



Particle diffusion in protein gels and at interfaces

Gireeshkumar Balakrishnan Nair

► To cite this version:

Gireeshkumar Balakrishnan Nair. Particle diffusion in protein gels and at interfaces. Other. Université du Maine, 2012. English. NNT : 2012LEMA1002 . tel-00710630

HAL Id: tel-00710630

<https://theses.hal.science/tel-00710630>

Submitted on 21 Jun 2012

HAL is a multi-disciplinary open access archive for the deposit and dissemination of scientific research documents, whether they are published or not. The documents may come from teaching and research institutions in France or abroad, or from public or private research centers.

L'archive ouverte pluridisciplinaire **HAL**, est destinée au dépôt et à la diffusion de documents scientifiques de niveau recherche, publiés ou non, émanant des établissements d'enseignement et de recherche français ou étrangers, des laboratoires publics ou privés.

Particle diffusion in protein gels and at interfaces

THÈSE

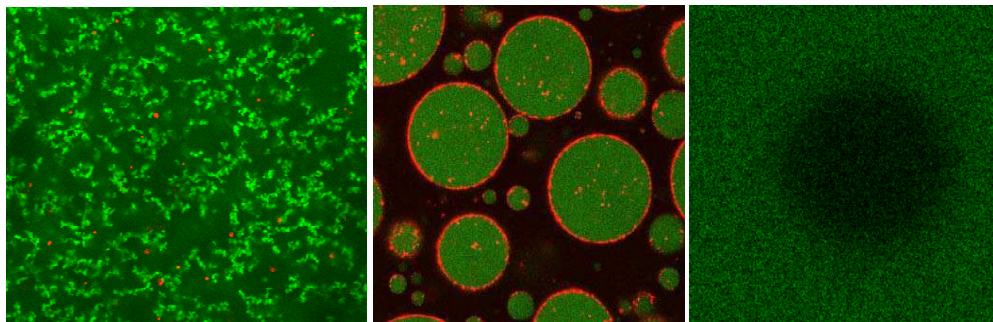
Présente le 14/03/2012 pour obtenir le grade de

DOCTEUR

Spécialité Chimie et Physico-chimie des polymères

Par

Gireeshkumar BALAKRISHNAN NAIR



Composition du Jury

Monsieur Francois Mariette (CEMAGREF, Rennes)

Rapporteur

Monsieur Fernando Leal Calderon (Institut Polytechnique, Bordeaux)

Rapporteur

Monsieur Alain Riaublanc (INRA, Nantes)

Examineur

Monsieur Lazhar Benyahia (PCI, Le Mans)

Examineur

Monsieur Dominique Durand (PCI, Le Mans)

Directeur de thèse

Monsieur Taco Nicolai (PCI, Le Mans)

Directeur de thèse

Acknowledgements

It is my great pleasure to thank both of my supervisors *Taco Nicolai and Dominique Durand* for their valuable guidance, suggestions, and saint like patience during these three years of my thesis. Also thanks to *Lazhar Benyahia and Christophe Chassenieux* for their help and advises in some occasion.

I express my gratitude to all the faculty members and technical staffs for providing me a good atmosphere to work in the lab. Also I thank to my friends in the lab for their constant encouragement and fun during these three years.

I thank the jury members: *Dr. Francois Mariette, Dr. Fernando Leal Calderon and Dr. Alain Riaublancanc* for their remarkable comments on this work.

I would like to thank *the Region Pays de la Loire* for the financial support for this thesis.

Table of contents

General Introduction	3
1. Bibliography	5
1.1. β -lactoglobulin.....	5
1.1.2. Molecular structure.....	5
1.1.3. Aggregation and gelation of β -lactoglobulin	6
1.1.4. Structure of dilute aggregates.....	7
1.1.5. Structure of the gels	7
1.2. Aqueous polymer mixtures	11
1.2.1. Phase separation	11
1.2.2. Phase diagrams	13
1.2.3. Emulsions.....	14
1.2.4. Interfacial tension	15
1.2.5. Mechanisms of emulsion instability	16
1.2.6. Pickering emulsions.....	17
1.2.7. Pickering water-in-water emulsions	20
1.3. Diffusion	21
1.3.1. Diffusion in liquids.....	22
1.3.2. Diffusion in gels	22
1.3.2.1. Theory	22
1.3.2.2. Simulation.....	24
1.3.2.3. Experiment.....	28
1.3.2.3.1. Methods to determine diffusion coefficient	28
1.3.2.3.2. Fluorescence recovery after photobleaching (FRAP).....	28
1.3.2.3.3. Multiple-particle tracking (MPT)	31
1.3.3. Tracer diffusion in protein solutions and gels.....	32
1.3.4. Diffusion of particles at the oil water interface.....	35
2. Materials and methods	41
2.1. Materials.....	41
2.1.1. Proteins	41
2.1.2. Particles.....	41

2.1.3. Poly(ethylene oxide) (PEO) and dextran.....	42
2.2. Methods	43
2.2.1. Confocal laser scanning microscopy (CLSM)	43
2.2.2. Principles of fluorescence.....	44
2.2.3. Parameters of fluorescence	45
2.2.3.1. Molar extinction coefficient	46
2.2.3.2. Quantum efficiency.....	47
2.2.3.3. Fluorescence lifetime	47
2.2.4. Fluorophores	47
2.2.5. CLSM Objectives.....	48
2.2.6. Resolution	50
2.2.7. Pinhole size	51
2.2.8. Electronic light detectors	52
2.2.9. Gain and offset on PMT	52
2.2.10. Photobleaching.....	53
2.2.11. Image analysis.....	53
2.2.11.1. Determination of local proteins concentration	54
2.2.11.2. Pair correlation function of CLSM images	54
2.2.12. Multiple-particle tracking	57
2.2.12.1. CLSM-particle tracking protocol.....	57
2.2.12.2. Particle tracking analysis.....	58
2.2.13. FRAP	60
2.2.13.1. CLSM-FRAP protocol	61
2.2.13.2 FRAP data analysis	62
2.3. Interfacial tension measurements by drop relaxation.....	63
2.4. Light scattering.....	66
2.5. Size exclusion chromatography	67
2.6. Viscosity	67
3. Results and discussion.....	71
3.1. Particle diffusion in β -lg gels	71
3.1.1. Introduction.....	71

3.1.2. Diffusion in liquids	71
3.1.3. Diffusion in gels	72
3.1.3.1. Structure of the gels.....	73
3.1.3.2. Tracer diffusion in gels using MPT	80
3.1.3.3. Tracer diffusion in gels using FRAP.....	83
3.1.4. Discussion	89
3.1.5. Conclusion	91
3.2. Particle diffusion at the interface of water-in-water emulsion.....	92
3.2.1. Introduction	92
3.2.2. Results and discussion	92
3.2.3. Structure of the particles at the interface	98
3.2.4. Mobility of the particles at the interface.....	100
3.2.5. Protein particles at the interface	102
3.2.6. Conclusion	103
General Conclusions	107
Annex.....	110
Annex-1. Multiple-particle tracking Algorithm.....	110
Annex-2. Most likelihood estimation method for FRAP	120
Annex-2.1. Input setting for FRAP data analysis	120
Annex-3. Input setting for the pair correlation analysis	125
Reference.....	129

Introduction and Bibliography

General Introduction

Brownian diffusion is the process responsible for spontaneous transport of matter from one part of the system to another. Knowledge of the mobility of particles in materials is of prime importance for many applications. In this thesis we investigate the diffusion of tracer particles in two complex media: globular protein gels and water in water emulsions formed by mixtures of incompatible water soluble polymers. The two systems may be considered as representative for two large classes of complex media: particle gels and emulsions. For this investigation we explored the possibilities of using confocal laser scanning microscopy (CLSM) to measure the displacement of tracer particles in such systems. We have used Multi-Particle Tracking for tracers with a radius larger than 100nm and Fluorescence recovery after photobleaching for smaller tracers.

The objective for the protein gels was to correlate the structure of the gel with diffusion of tracer particles through it. There is an interest in improving the health of food products by adding nutriments encapsulated in small particles and hence the diffusion of tracer particles in food colloidal gels becomes an important issue. Numerous studies have been reported in the area of tracer diffusion in polymer solutions and gels. However, most of these studies are not relevant to the diffusion of tracer particles in globular protein gels. From the many globular proteins, β -lactoglobulin (β -lg) was chosen for two main reasons. 1) The structural properties of heat-set β -lg gels have been thoroughly investigated at various conditions of ionic strength and pH. 2) Structures with a range of pore sizes could be prepared by varying the salt concentration. In addition, β -lg is the main protein component of whey and is much used in industrial food products.

It is well-known that oil in water emulsions can be efficiently stabilized by adding small solid particles that become spontaneously trapped at the interface of the emulsion droplets. Such emulsions are commonly known as Pickering emulsions. In this thesis we will show that the effect can occur in water in water emulsions formed by mixing aqueous solutions of two incompatible polymers: polyethylene oxide (PEO) and dextran which is a neutral polysaccharide. These two polymers were chosen because they are neutral and have a relatively simple behavior in pure solutions. In addition, the thermodynamics and the interfacial tension of PEO-dextran mixtures have already been reported in the literature. Our objective was to study the mobility of latex particles with different radii at the droplet interface in these emulsions. The advantage of using water in water emulsions

formed by mixing viscous polymer solutions is that creaming or sedimentation is very slow allowing MPT at stable droplet interfaces.

The thesis consists of 3 chapters and a general conclusion. In the first chapter we discuss the literature focusing on heat-set β -lactoglobulin gels; phase separation and emulsions; and tracer diffusion. In the second chapter we discuss the materials and methods that we have used in this study. This chapter includes a discussion of the different techniques that have been used to analyze the CLSM images. Details of the computer routines that were utilized are given in the appendices.

The third chapter divided in to two sections. The first section reports the experiments on the diffusion of tracer particles in β -lg gels. Here we discuss the results obtained from multiple particle tracking with larger tracers and then the results obtained from FRAP measurements with smaller tracers. We will show that both MPT and FRAP are useful and complementary techniques to study the mobility of tracers in protein gel. The main conclusion is that the tracer mobility is not only related to the average pore size, but that also the pore size distribution is of prime importance. Whereas the second section reports our investigation of the mobility of tracer particles at the droplet interface of emulsions formed by mixing aqueous solutions of PEO and dextran. Trapping of the particles was correlated to the experimentally determined interfacial tension and the contact angle of the particles with the interface. The diffusion coefficient of the particles at the interface could be determined using MPT and was found to be determined by the viscosity of the two phases and the contact angle.

1. Bibliography

Proteins are polymers of amino acids, with each amino acid residue joined to its neighbor by a peptide bond. Their structure can be described in four levels. Each protein is characterized by a unique sequence of amino acids, called its primary structure. The secondary structure refers to the regular arrangement of amino acid residues in a segment of the polypeptide chain, in which each residue is spatially related to its neighbors in the same way. The most common secondary structures are α -helix and β -sheet. The tertiary structure describes the complete three dimensional structure of a poly peptide chain. Quaternary structures arise from the oligomerization of proteins and it ranges from simple dimers to large complexes.

1.1. β -lactoglobulin

β -lactoglobulin (β -lg) is the major whey protein in the milk of ruminants and many other mammals. Six different genetic variants of β -lg have been identified, among these two are important: variants A and B that differ at position 64 (Asp/Gly) and 118 (Val/Ala) (Hambling, McAlpine, & Sawyer, 1992). β -lg has been the subject of a wide range of biophysical studies because of its abundance and ease of isolation. Its biological function is not clear, but it is a member of the family of lipocalins (Oliveira et al., 2001) which carry small hydrophobic molecules and thus may act as specific transporters.

1.1.2. Molecular structure

The primary structure of β -lg consists of 162 amino acids with a molecular weight around 18.40 Kg/mol. Its isoelectric point is at pH 5.2. It contains 5 sulfated amino acids. It has a dense approximately spherical tertiary structure (Brownlow et al., 1997) with a radius of about 2 nm, see figure 1.1.

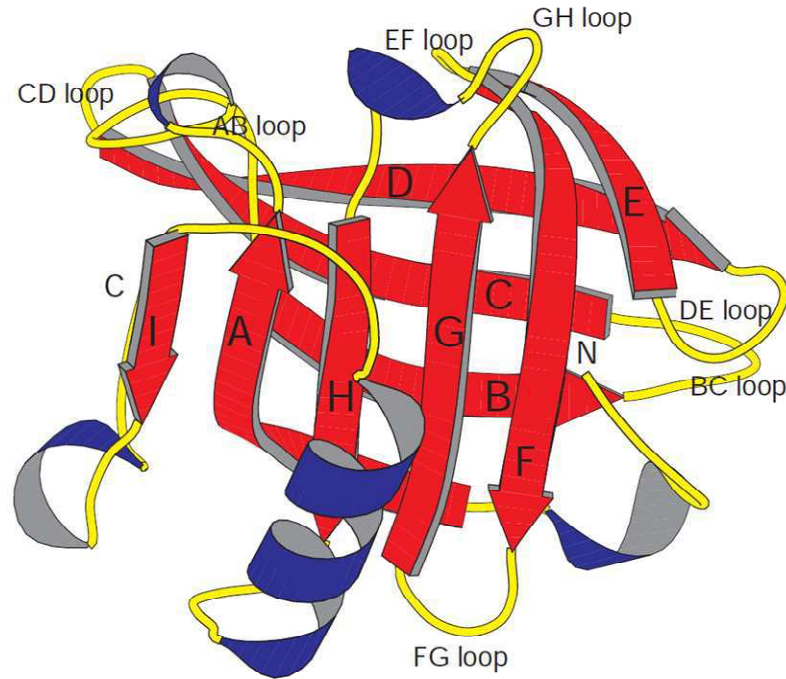


Figure 1.1. Schematic drawing of the structure of β -lactoglobulin (Brownlow et al., 1997).

1.1.3. Aggregation and gelation of β -lactoglobulin

Heating solutions of globular proteins such as β -lg above their denaturation temperature results in partial unfolding of the chains which leads in many cases to aggregation of the proteins. Above a critical protein concentration (C_g) the solution gels when heated. The process of aggregation and gelation of β -lg has been widely studied. The structure of the aggregates and gels has been studied by scattering techniques and microscopy (Ako, Durand, Nicolai, & Becu, 2009; Taco Nicolai, Britten, & Schmitt, 2011; Pouzot, Durand, & Nicolai, 2004). The effect of electrostatic interaction between the proteins on the structure of the aggregates has been investigated by changing the pH at a fixed salt concentration and protein concentration or by changing the salt concentration at fixed pH and protein concentration (Baussay, Bon, Nicolai, Durand, & Busnel, 2004; Mehalebi, Nicolai, & Durand, 2008)

1.1.4. Structure of dilute aggregates

The rate at which native β -lg aggregates increases exponentially with increasing temperature and is characterized by a large activation energy (Le Bon, Nicolai, & Durand, 1999; Taco Nicolai et al., 2011). The rate of aggregation also changes with protein concentration, ionic concentration and pH. During the initial stages of aggregation process small oligomers have been observed between pH 6 and 8.7 (Bauer, Hansen, & ogedal, 1998). With heating time, the fraction of unaggregated β -lactoglobulin decreases while the number and size of the aggregates increases. At low protein concentrations, the heated solutions at steady state mainly contain oligomers, but at higher concentration larger aggregates are formed.

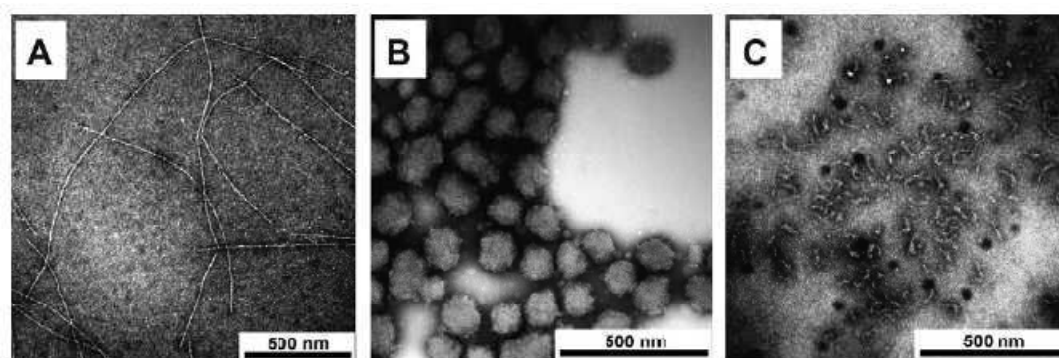


Figure 1.2. Negative-staining TEM images of β -lg aggregates formed at pH 2.0 (A), pH 5.8 (B) and pH 7.0 (C). Scale bars are 500 nm. Reproduced from Jung et al (Jung, Savin, Pouzot, Schmitt, & Mezzenga, 2008)

The structure of the aggregates at steady state depends on the pH (Durand, Gimel, & Nicolai, 2002; Jung et al., 2008). Figure 1.2 shows examples of β -lg aggregates at different pH (Jung et al., 2008). Small curved strands are formed at pH 7, spherical aggregates at pH 5.8 and long rigid strands at pH 2.

1.1.5. Structure of the gels

The visual aspect of the globular proteins gels strongly depends on electrostatic interaction between the proteins. The transition from transparent to turbid gels occurs in a narrow range of ionic strength (Ako, Durand et al., 2009; Mehalebi et al., 2008). Figure

1.3 shows the transition of the visual aspect of β -lg gels structure from transparent to turbid as a function of salt concentration.

Mehalebi et al (Mehalebi et al., 2008) investigated the structure of β -lg gels formed at various pH and salt concentrations using light scattering techniques. The results were expressed in terms of an apparent molar mass (M_a), which reflects the amplitude of the concentration fluctuations (heterogeneity) of the gel. The effect of the salt concentration was investigated for a range of pH from 6 to 9 at β -lg concentration $C = 100$ g/l. The value of M_a was found to increase exponentially with salt concentration between 0 and 200 mM, see figure 1.4. Gels with low values of M_a were transparent. At higher salt concentrations, the measurement of M_a is no longer accurate because of the high turbidity of the gels.

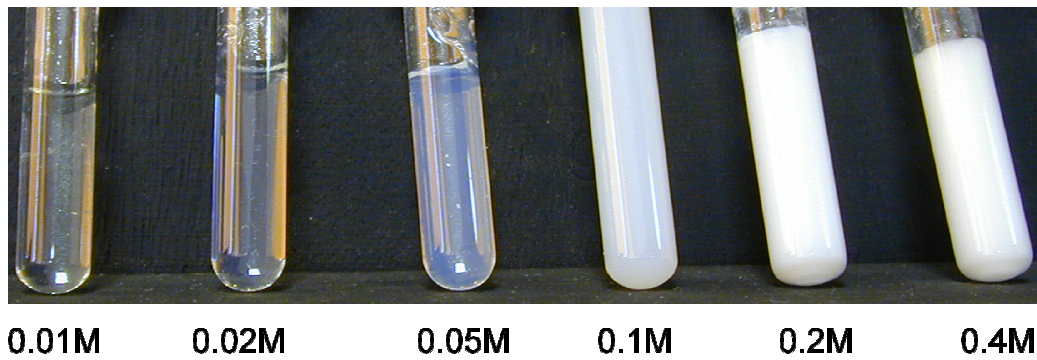


Figure 1.3. Transition from transparent to turbid gel structures as a function of salt concentration at β -lg concentration 100 g/l.

Ako et al (Ako, Nicolai, Durand, & Brottons, 2009) studied the effect of ionic strength (from 0 to 0.5 M) at pH7 for β -lg gels at $C=100$ g/L. The local structure of the gels was investigated with the help of small angle X-ray scattering (SAXS). Figure 1.5 shows the scattering intensity as a function of the scattering wave vector (q) for gels formed at pH 7 at different salt concentrations. The structure factor has a peak for the gels formed in the absence of salt indicating the ordered arrangement of the protein strands in these gels. They found that the proteins strands are situated at a preferred distance of $2\pi/q_{\max}=22$ nm. The ordered arrangement in the gel decreased with decreasing pH towards the isoelectric point or with increasing ionic strength at pH 7 while the intensity

at small q values increased. This explains the increase of turbidity of the gel with decreasing pH or increasing ionic strength. It was observed that in a narrow range of salt concentrations and pH the gel structure is self similar over some length scale so that the structure factor decreased as a power law with increasing q : $S(q) \propto q^{-df}$ with a fractal dimension df close to 2. At higher salt concentrations or lower pH it was found that $S(q) \propto q^{-4}$. This finding shows the formation of homogeneous micro domains as was also observed by confocal laser scanning microscopy (CLSM), see below. The q dependence deviated from the Porod law at $q > 0.15 \text{ nm}^{-1}$, which means that the domains are homogeneous down to about 10 nm.

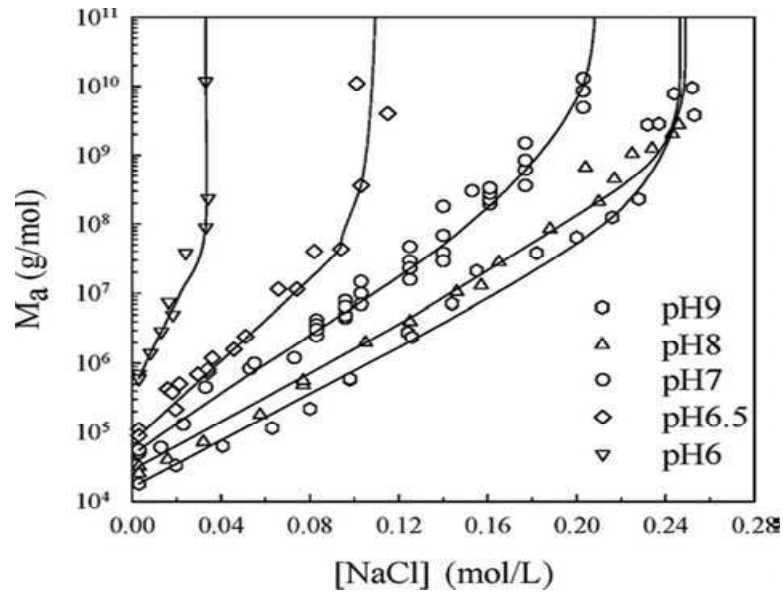


Figure 1.4. Dependence of M_w on the salt concentration at different pH as indicated in the figure for β -lg gels at $C=100 \text{ g/l}$ (Mehalebi et al., 2008).

The structure of the gels at higher salt concentrations or pH close to the isoelectric point cannot be investigated with light scattering, but can be studied with CLSM (Ako, Durand et al., 2009). Figure 1.6 shows CLSM images of β -lg gels formed at pH 7 and $C=100 \text{ g/l}$ for different NaCl concentrations. At low salt concentrations the gel structure is homogeneous on the length scales accessible to CLSM, but at higher salt concentrations the gels consist of micron sized spherical domains formed by micro phase separation.

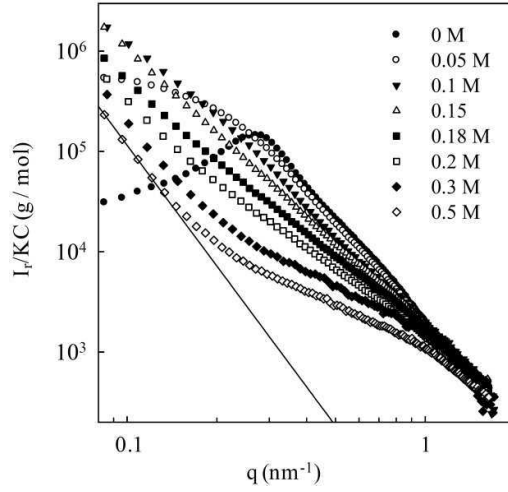


Figure 1.5. Dependence of the scattering intensity on the scattering wave vector for β -lg gels ($C = 100$ g/L) for different NaCl concentrations at pH 7. The solid line has slope -4 (Ako, Nicolai et al., 2009)

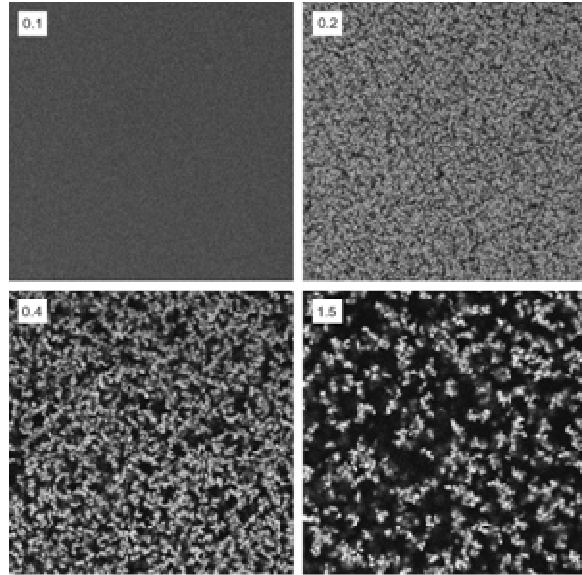


Figure 1.6. Shows the CLSM images of β -lg gels formed at different salt concentrations as indicated in the images for pH 7 and β -lg concentration 100 g/l. The width of the image is 160 μ m.

They studied the effect of the NaCl concentration on the structure of the gel with CLSM over a wide range of pH from 2 to 9. Between pH 4.1 and 5.8, micro phase separation of the proteins occurs in salt free solutions. Outside this range microphase

separation occurs only above a critical salt concentration that increases with increasing pH above 5.8 and decreasing pH below 4.1, see figure 1.7 (a). The effect of the protein concentration on the structure of heated β -lg solutions has been investigated at pH 7, see figure 1.7 (b).

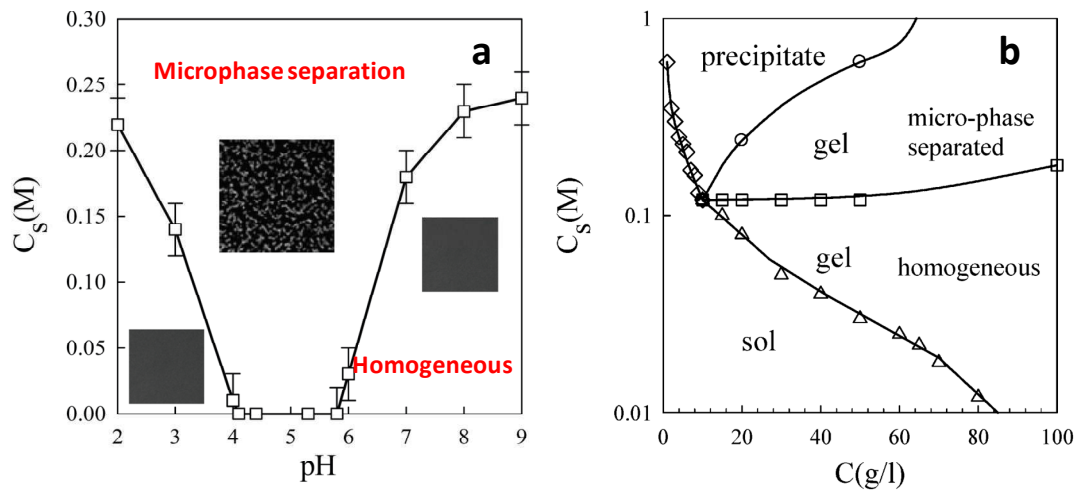


Figure 1.7: State diagram showing the conditions of pH and NaCl concentration at which β -lg ($C=100\text{g/l}$) forms homogeneous or microphase separated gels (left). Diagram showing the conditions of NaCl concentration and protein concentration at which β -lg forms a sol, a homogeneous gel, a precipitate or a micro-phase separated gel at pH 7 (Ako, Nicolai et al., 2009) (right).

1.2. Aqueous polymer mixtures

Aqueous polymer mixtures are most commonly encountered in food and household products and hence understanding their phase behavior and structure is crucial to design, formulation and manufacture of products.

1.2.1. Phase separation

Mixed polymer solutions can vary from homogeneous to fully phase separated, depending on the thermodynamics and the kinetics of phase separation. Miscibility of the mixed polymers can be predicted on the basis of the free energy of mixing. If it is

positive, then the mixture will have a tendency to form two phases. The Gibbs free (ΔG) energy of mixing is a combination of mixing enthalpy (ΔH_{mix}) and entropy of mixing (ΔS_{mix}):

$$\Delta G = \Delta H_{mix} - T\Delta S_{mix} \quad 1.1$$

Generally ΔH_{mix} is positive which favours demixing of the two polymers. However, for small solute molecules, ΔS_{mix} may be sufficiently large so that the molecules will mix. In the case of polymers, ΔS_{mix} is relatively smaller, so that it is common for them to demix into a phase enriched in one of the polymers and another enriched in the other polymer. For polyelectrolytes, the nature of the interaction in solution depends on the sign and degree of charge on the mixed polymers. Three different situations are illustrated in the figure 1.8 (Frith, 2010) for neutral polymers and polyelectrolytes. The system has a strong tendency to phase separate, if the two polymers are either neutral or have charges of the same sign. If the two polymers have opposite charges then they will attract each other and form complexes which may eventually precipitate.

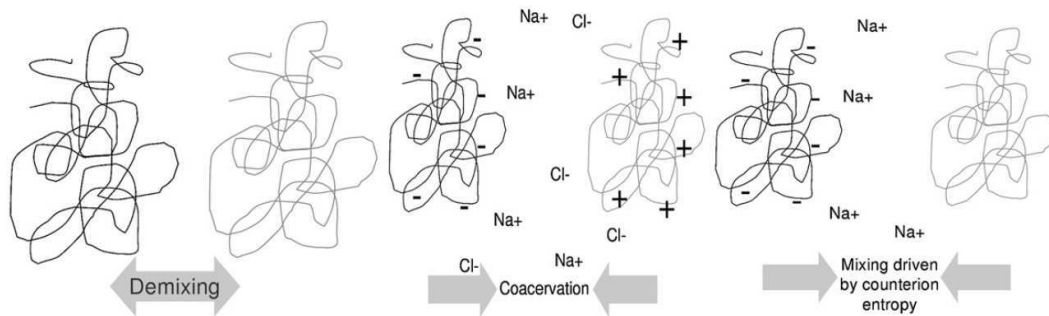


Figure 1.8. Illustration of the possible influence of charges on the polymer in solution. From left to right: uncharged polymers tend to phase separate; oppositely charged polymers form complexes; mixtures of charged and uncharged polymers tend form homogeneous mixtures at low salt concentrations (Frith, 2010).

The situation becomes more complex when only one polymer is charged so that the entropy of the counter ions controls the mixing of the two such polymers in solution. Piculell and Lindman (Piculell & Lindman, 1992) found that mixing of the two polymers

is strongly depended on the ionic strength. At low ionic strength the system is usually homogeneous, but at higher salt concentrations it phase separates.

1.2.2. Phase diagrams

The phase behavior of mixed polymer solutions can be characterized by a phase diagram which describes the conditions of phase separation, either as an X-Y plot or a ternary plot as shown in the figure 1.9 (Norton & Frith, 2001) where the phase diagram of aqueous gelatin-maltodextrin mixtures is shown, which is typical for many biopolymer mixtures. The binodal separates the one phase from the two phase region. The composition of a biopolymer mixture can be represented by a single point in the phase diagram. If the point lies in the two phase region then the system has a tendency to separate into two phases with compositions that lie on the binodal. The tie line connects the initial composition with the compositions of the separate phases. The volume fraction of each phase after phase separation can be deduced from the tie-line length between the initial composition and the composition of each phase. Figure 1.9 shows that the binodal is close to the axis, which means that for most phase separating compositions each phase mainly contains one of the polymers and only a small amount of the other. The 50:50 phase volume line shows where the two phases have the same volume fraction after phase separation. Below this line, maltodextrin is the continuous phase, but above it, gelatin is the continuous phase. The critical point of the phase diagram is the point on the binodal where the tie-line length becomes zero.

As mentioned above, if the composition of the mixture lies above the binodal line then the system has a tendency to phase separate into two phases. There is a second line that lies within the binodal region which is termed the spinodal, see the dotted line in figure 1.9. The spinodal separates the metastable region from the unstable region. If a solution composition lies between binodal and spinodal then the system will phase separate through nucleation and growth, which may take a long time and may not be observed in the time scale of an experiment. The reason for metastability of compositions between the binodal and the spinodal is that the free energy of mixing increases during the initial process of phase separation and only decreases ones the phase separated domains (nuclei) are larger than a critical size. Thermodynamically unstable mixtures phase separate everywhere from the very beginning (De Gennes, 1979) which is known

as the spinodal decomposition. Figure 1.10 shows a CLSM image of the microstructure of biopolymer mixture during spinodal decomposition (Firoozmand, Murray, & Dickinson, 2009)

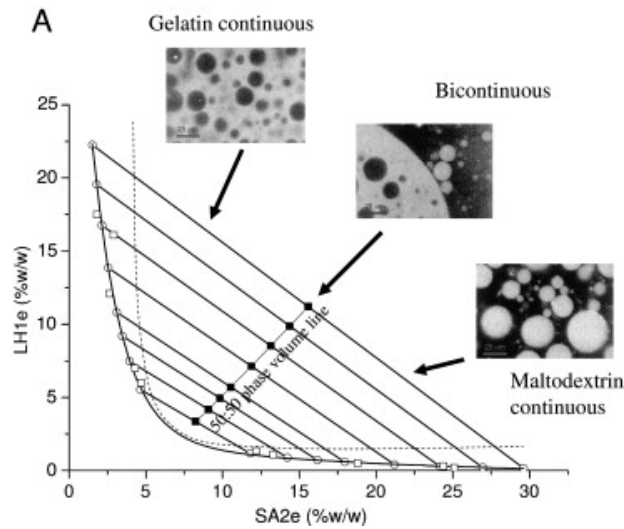


Figure 1.9. Phase diagram of Maltodextrine (SA2e)/ gelatin (LH1e) mixtures. The open squares represent the experimentally determined phase compositions while the open circles represent theoretical values (Norton & Frith, 2001).

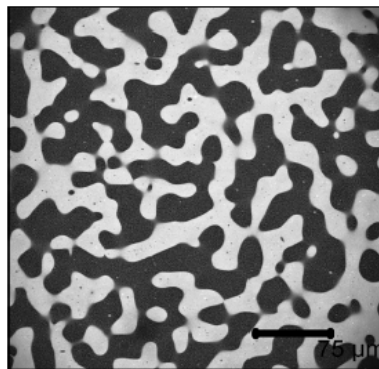


Figure 1.10. CLSM image of spinodal type microstructure of phase separated mixed biopolymer solution of protein-polysaccharide system (Firoozmand et al., 2009).

1.2.3. Emulsions

An emulsion is a dispersion of droplets of one liquid in another liquid with which it is immiscible. In foods, the two immiscible liquids are usually an oil and an

aqueous solution. Emulsions can be classified on the basis of the organization of the two immiscible phases. If the oil droplets are dispersed in the water phase then it is called an oil in water emulsion (e.g., milk, salad dressing and mayonnaise) whereas the inverse is known as a water in oil emulsion (e.g., butter or margarine). The material within the droplets is usually referred to as the dispersed or internal phase, whereas the material that makes up the surrounding liquid is called the continuous or external phase. From a thermodynamic point of view, these emulsions are unstable because of the positive free energy associated with the oil-water interface.

Concentrated aqueous solutions of thermodynamically incompatible polymers form water in water emulsions (Frith, 2010). This situation often occurs in food systems containing proteins and polysaccharides when the protein-polysaccharide interaction is net repulsive.

1.2.4. Interfacial tension

The interfacial tension (γ) is a measure of the cohesive energy arising from the imbalance of forces between the molecules at an interface. When two different phases are in contact with each other then molecules at the interface experience an imbalance of forces. This will result into an increase of the free energy at the interface. This excess free energy can be quantified as the amount of energy required to create a new surface or as the force that acts perpendicular and inward from the boundaries of the surface to reduce the area of the interface. The unit of interfacial tension in the SI system is Nm^{-1} .

The spherical droplet structure displayed by phase separating mixtures results from the minimization of the interfacial tension within the system. The interfacial tension strongly depends on the nature of the two phases that are in contact. The interfacial tension of phase separated aqueous polymer mixtures was found to be 0.5-500 $\mu N/m$ which is orders of magnitude lower than between oil and water (Ding et al., 2002). Bamberger et al (Bamberger, Seaman, Sharp, & Brooks, 1984) and Forciniti et al (Forciniti, Hall, & Kula, 1990) studied the interfacial tension in aqueous mixtures of polyethylene glycol (PEG) and dextran. They found that the interfacial tension ranged from 30 to 300 $\mu N/m$ depending on the molecular weight and total concentration of the

polymers. They showed that there exists a correlation between the interfacial tension and the tie-line length (TLL),

$$\gamma = C_1 \cdot (TLL)^{C_2} \quad 1.2$$

$$\gamma = C_3 \cdot \exp[C_4 \cdot (TLL)] \quad 1.3$$

or the interfacial tension and the difference between the concentration of the polymers (ΔC) in the separated phases:

$$\gamma = C_5 (\Delta C_{dex})^{C_6} \quad 1.4$$

$$\gamma = C_7 (\Delta C_{PEG})^{C_8} \quad 1.5$$

Where the experimental constants C_1 to C_8 were found to depend on the type of biopolymer, molecular weight, temperature and concentration.

1.2.5. Mechanisms of emulsion instability

The most important mechanisms of physical instabilities are Ostwald ripening, creaming, sedimentation, aggregation, and coalescence. During Ostwald ripening, larger droplets grow at the expense of smaller ones which is due to the fact that the solubility of the material within the dispersed droplets increases with decreasing droplet radius (Kabalnov, 1998); (McClements, 2005). Figure 1.11 illustrates the various mechanisms of physical emulsion instability (Fredrick, Walstra, & Dewettinck, 2010).

Creaming or sedimentation is caused by the density difference between the dispersed phase and the continuous phase. If the droplets have a lower density than the continuous medium, then the droplets tend to go upwards which is referred to as creaming. If the dispersed phase is of greater density then the droplets tend to move downwards which is referred to as sedimentation. Due to thermal energy, droplets in emulsions collide with their neighbors, after collision they may coalesce, move apart or remain aggregated depending on the stability of the interface and the relative magnitude of the attractive and repulsive forces between them.

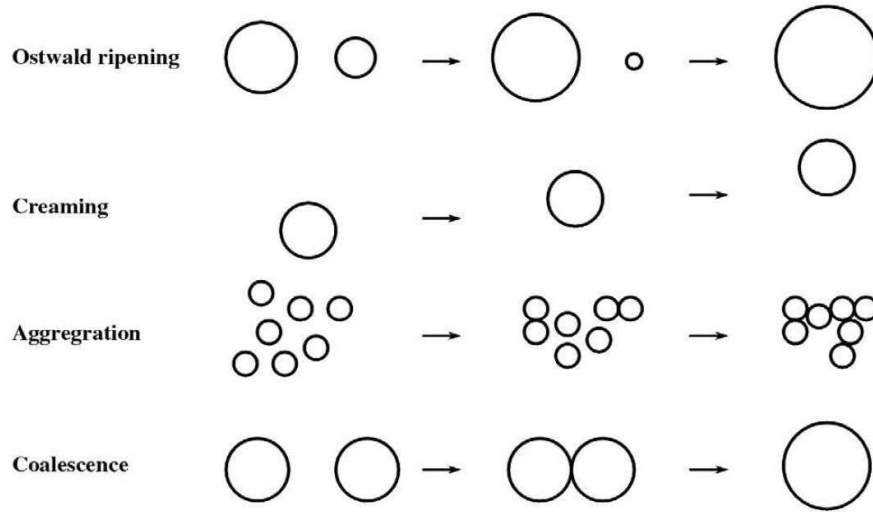


Figure 1.11. Schematic drawing of different mechanisms of physical emulsion instability (Fredrick et al., 2010).

1.2.6. Pickering emulsions

In 1907, Pickering discovered that finely divided solid particles could be used as stabilizers in emulsions and are therefore called Pickering emulsions (Pickering, 1907). The particles are adsorbed at the oil-water interfaces and provide a barrier against coalescence, thereby stabilizing the emulsion. Figure 1.12 shows an optical microscopy image of a water droplet in cyclohexane stabilized by hydrophilic latex particles of diameter 3.2 μm .

Assuming that the particles are small enough so that the effect of gravity is negligible, then the energy (ΔG) required to remove particles with radius R from an oil-water interface is given by the following equation (Aveyard, Binks, & Clint, 2003),

$$\Delta G = \pi R^2 \gamma_{ow} (1 - |\cos \theta_{ow}|^2) \quad 1.6$$

Where θ_{ow} is the contact angle of the spherical particle with the interface. For hydrophilic particles $\theta < 90^\circ$ with respect to the water phase which means that a larger fraction of the particle surface resides in the water phase than in the oil phase. For hydrophobic particles $\theta_{ow} > 90^\circ$ and the particle resides more in the oil than in the water, see figure 1.13.

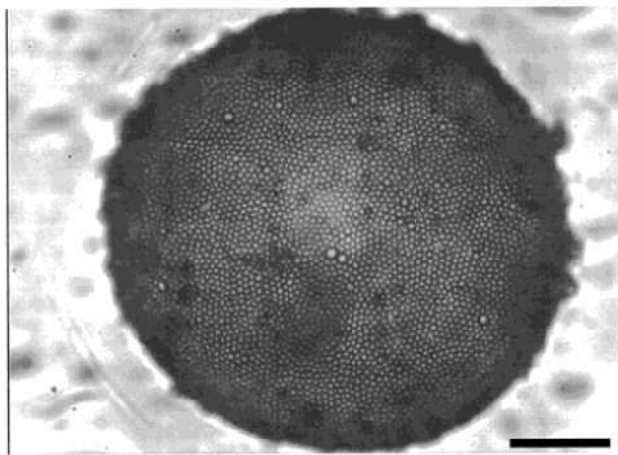


Figure 1.12. Optical microscope image of a single water drop in cyclohexane coated with 3.2 micron hydrophilic latex particles. The scale bar corresponds to 50 μm (Aveyard *et al.*, 2003).

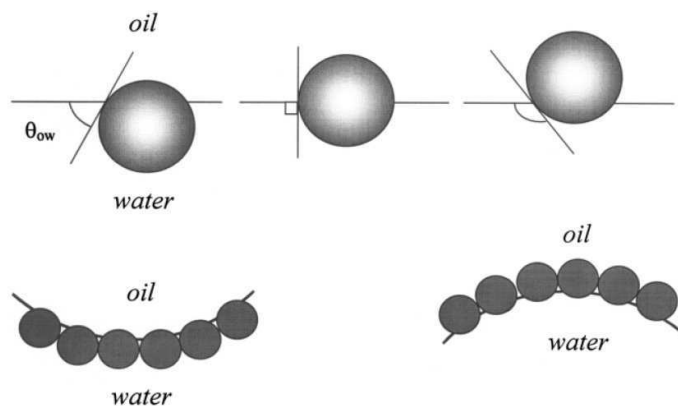


Figure 1.13. Schematic representation of a spherical particle at a planar oil water interface for different contact angles (Aveyard *et al.*, 2003)

From Eq. 1.6 it is clear that the particle is most strongly held at the interface when $\theta = 90^\circ$. There will be a rapid decrease of ΔG when θ is increased or decreased away from 90° . For instance, the amount of energy required to remove a spherical particle with a radius $R = 10 \text{ nm}$ from a toluene-water interface ($\gamma_{ow} = 0.036 \text{ N m}^{-1}$) is 2750 kT for $\theta = 90^\circ$. However, when θ is 20° or 160° then the energy is reduced to 10 kT. Figure 1.14 shows the variation of interfacial free energy with the contact angle for this system.

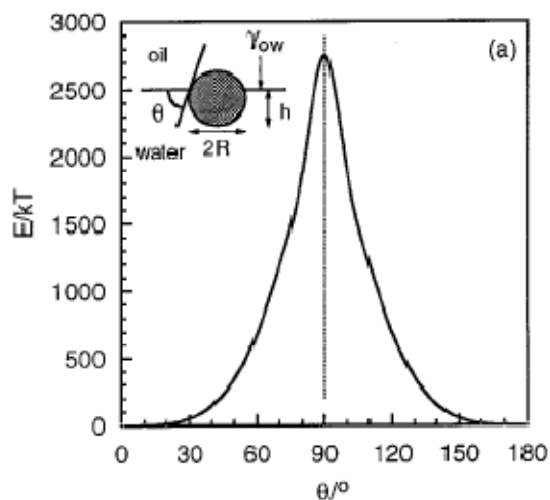


Figure 1.14. Dependence of the energy required to remove a spherical particle with a radius $R=10$ nm from a toluene-water interface on the contact angle.

Aveyard et al investigated the effect of the initial particle concentration on the average emulsion drop size and stability for a given emulsification condition. They have used alkylsilane coated spherical silica particles with radius 25 nm. In figure 1.15 the mean droplet diameter immediately after preparation is plotted as a function of particle concentration. They found that the droplet diameter decreased with increasing particle concentration. The size of the droplets decreased by a factor of eight when the particle concentration increased 10 fold. They also observed that the ratio of the total number of particles to the number of particles adsorbed was around unity up to a particle concentration of 3 wt%, but it increased by more than a factor 2 when the concentration of the particle was 5.6 wt% and the excess particles appeared in the continuous phase. Up to 3 wt%, the droplet size decreased which increased the total surface and hence allowed more particles to go to interface. Once the droplets attained a limiting size the excess particles went to the continuous phase.

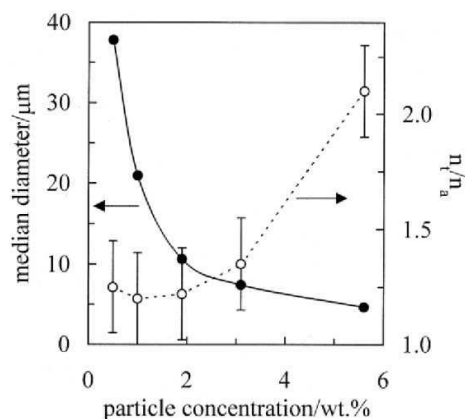


Figure 1.15. Median drop diameter (left hand ordinate, filled points) as a function of aqueous concentration of hydrophobic silica particles (25 nm diameter) in PDMS-in-water emulsions. Also shown is the ratio of the total number of particles available to the number required to provide a monolayer around all drops (right hand ordinate, open points) (Aveyard et al., 2003).

Particle size is also a major factor which determines the stability of the emulsion. Sanford and Levine (Levine & Sanford, 1985) proposed that particles size should be in the range of a few nanometers to a few micrometers to stabilize an emulsion. There exists a critical diameter of the particle below which the emulsion is not stable. It follows from Eq. 1.6 that is the desorption energy depends on the square of the particle size

1.2.7. Pickering water-in-water emulsions

Binks et al (Binks & Horozov, 2006) showed recently that particles can also be trapped at the interface between water and ionic liquids and Firoozmand (Firoozmand et al., 2009) et al showed that they can even be trapped at the interface of between protein and polysaccharide rich aqueous phases. Firoozmand et al found that self assembly of the latex particles at the interface perturb and significantly slow down coarsening of the heterogeneous microstructure. However, they considered that the interfacial tension for water-in-water emulsions is too low and suggested that the driving force was the repulsion between the particles and the two incompatible polymers within the system. Figure 1.16 shows CLSM images of aged samples of a mixed biopolymer system (25.5

wt% sugar, 31.4% glucose syrup, 7 wt% gelatin, and 4 wt% oxidized starch) containing polystyrene latex particles

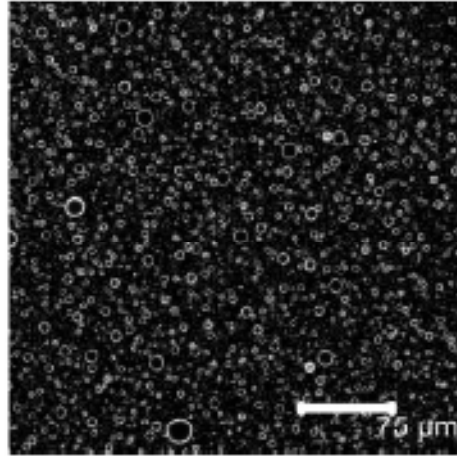


Figure 1.16. CLSM images of aged samples of a mixed biopolymer system (25.5 wt% sugar, 31.4% glucose syrup, 7 wt% gelatin, and 4 wt% oxidized starch) containing polystyrene latex particles (Firoozmand et al., 2009).

1.3. Diffusion

Diffusion is the process which is responsible for the spontaneous movement of matter from a region of higher concentration to a region of lower concentration and it is due to random molecular (Brownian) motion. The diffusion process is much faster in gases than in liquids and solids (Masaro & Zhu, 1999). The first mathematical treatment of diffusion was done by Fick (Fick, 1855) who developed a law for diffusion in one dimension.

$$J = -D \frac{\partial c}{\partial z} \quad 1.7$$

Where J is the flux per unit area, D is the diffusion coefficient and $\partial C/\partial z$ is the gradient of concentration along z axis. When the concentration of the studied species is very small, then the diffusion of the species is also called tracer diffusion.

1.3.1. Diffusion in liquids.

The diffusion coefficient of dilute spherical particles in liquids is related to the solvent viscosity (η) and the hydrodynamic radius (a) of the particle via the Stokes-Einstein relation (Cussler, 2000),

$$D = \frac{K_B T}{f} = \frac{K_B T}{6\pi\eta a} \quad 1.8$$

Where f is the friction coefficient of the solute, K_B is Boltzmann's constant and T is the absolute temperature. This equation shows the relation between the thermal energy and the drag force that a particle feels when it is pulled through a liquid. From this equation it is clear that the diffusion coefficient increases with increasing temperature and decreases with increasing viscosity and particle radius. The relation is valid only when the solute is much larger than the solvent (Cussler, 2000).

1.3.2. Diffusion in gels

1.3.2.1. Theory

The diffusion in polymer solutions and gels is complex and it is difficult to predict and control the diffusion of molecules in these systems. There exist different theoretical models of diffusion based on obstruction effects, free volume effects and hydrodynamic interactions. In obstruction models, it is assumed that the self-diffusion coefficient of gels is much slower than that of the diffusant. Hence the polymer is represented as immobile and impenetrable segments immersed in a solution. Many models were developed (Fricke, 1924; Mackie & Meares, 1955) on the basis of obstruction, which describe the diffusion of small molecules in dilute or semi dilute polymer solutions satisfactorily, but deviate for large diffusants and for higher polymer concentrations.

Ogston et al (Ogston, Preston, & Wells, 1973) developed an approach in which the self-diffusion coefficient of the diffusant molecules depends on both the size of the obstacle present in the solution and on the size of the diffusant, as shown in the following equation:

$$\frac{D}{D_0} = \exp \left[-\frac{R_h + \rho}{\rho} \varphi^{1/2} \right] \quad 1.9$$

Where ϕ is the volume fraction of the polymer, R_h the hydrodynamic radius of the diffusant and ρ the cylindrical radius of the fiber. However, this model also failed at high polymer concentrations when hydrodynamic interactions became non-negligible (Ogston et al., 1973).

Hydrodynamic theories consider hydrodynamic interaction in the whole system. This includes the frictional interactions between the solute and the polymer, the solute and the solvent and the solvent and the polymer. All these interactions play an important role for the diffusion in more concentrated polymer solutions where the polymer chains start to overlap. Among the models based on hydrodynamic theories, the most remarkable one was developed by Phillies (Phillies, 1986, 1987, 1989) who proposed a stretched exponential equation to describe the self-diffusion of macromolecules over a wide range of concentrations:

$$D = D_0 \exp(-\alpha c^\nu) \quad 1.10$$

Here α and ν are scaling parameters which depend on the molecular weight of the diffusant polymer. This equation was proposed on the basis of numerous experimental data from Phillies own research group as well as from the literature (Phillies, 1986). For macromolecules α scales with molecular weight ($\alpha \sim M^{0.9 \pm 0.1}$) whereas for small diffusant, α scales with the hydrodynamic radius ($\alpha \sim R_h$). The other scaling parameter ν varies between 1 for low molecular weight diffusants and 0.5 for high molecular weight diffusants and between these limits $\alpha \sim M^{-1/4}$. Figure 1.17 shows the self-diffusion coefficient of polystyrene as a function of molecular weight in dibutyl phthalate for different polymer concentrations (Phillies, 1992).

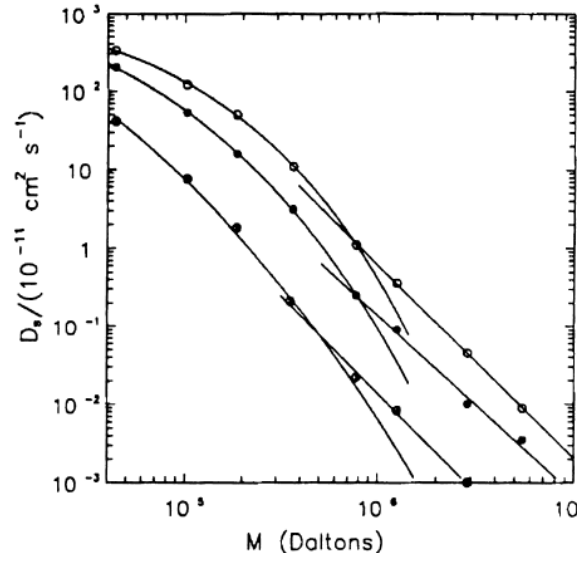


Figure 1.17. Self-diffusion coefficient of polystyrene as a function of the molecular weight in dibutyl phthalate for different polymer concentration: 13 wt% (open circles), 18 wt% (filled circles) and 40.6 wt% (half-filled circles). Curved lines represent the fittings to the stretched exponential equation while the straight lines correspond to power laws (Phillies, 1992).

1.3.2.2. Simulation

Babu et al (Babu, Gimel, & Nicolai, 2008) simulated tracer diffusion of colloidal particles in the gels that were formed by diffusion limited cluster aggregation (DLCA) or reaction limited cluster aggregation (RLCA) of hard spheres. The diffusion of tracer particles in these gels strongly depends on the volume fraction of the gels that can be accessed by the center of mass of the tracer particles. They investigated in detail the effect of accessible volume on the mean square displacements of tracer particles by varying the volume fraction of the gels, the structure of the gels and also the size of the tracers. Figure 1.18 shows a plot of accessible volume ϕ_a versus the volume fraction ϕ for randomly distributed frozen hard spheres (FHS), and gels formed by DLCA and RLCA. For a given volume fraction, ϕ_a is larger for RLCA gels than for DLCA gels for which it is in turn larger than for FHS.

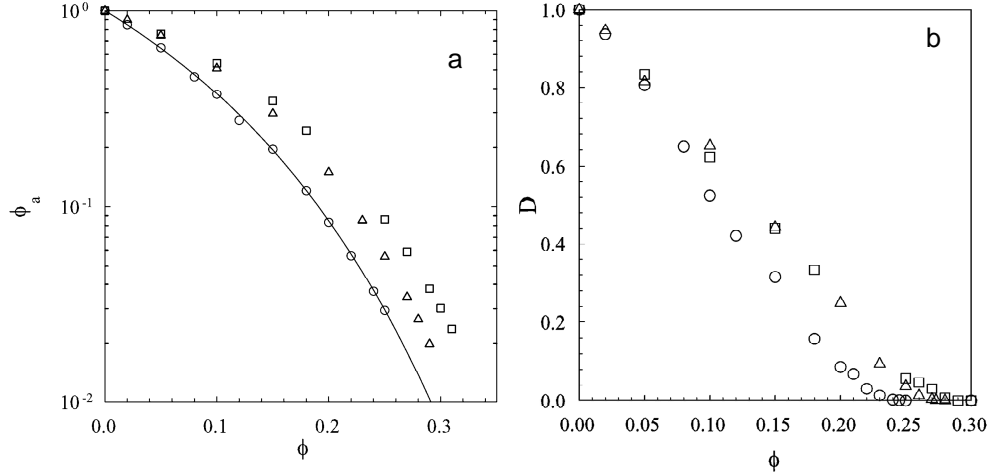


Figure 1.18. (a) Accessible volume as a function of the volume fraction for spherical tracers with the same diameter as that of the spherical obstacles for FHS (circles) and DLCA (triangles) or RLCA (squares) gels. Figure 1.18. (b) Dependence of diffusion coefficient of the tracer as a function of volume fraction of obstacles for FHS (circles) and DLCA (triangles) or RLCA (squares) gels (Babu et al., 2008).

Gels have higher accessible volume than FHS systems because the particles in the gels are connected which leads to overlap of the excluded volume. The higher ϕ_a of RLCA than that of DLCA comes from the fact that the RLCA gels are denser than DLCA gels and therefore more excluded volume overlaps in this gel. For all the systems ϕ_a decreases with increasing the volume fraction of the obstacle.

The long time diffusion coefficient relative to the free diffusion coefficient (D), of the tracer particles is plotted as a function of volume fraction of the three systems in figure 1.18 (b). From the graph it is clear that for a given volume fraction of obstacles, the relative diffusion coefficient of the tracers in the RLCA gels is larger than that in DLCA gels which is in turn larger than in FHS. In all the above systems D decreases with increasing ϕ and at a critical volume fraction (ϕ_c) the particles become trapped. At low volume fractions, the accessible volume percolates through the system, but the number of isolated pores increases with increasing ϕ and above ϕ_c there are only isolated pores in which the tracers are trapped. Figure 1.19 (a) shows images of ϕ_a for DLCA gels at different values of ϕ . Percolating pores are yellow whereas the red color indicates the

isolated pores. The mean square displacement averaged over many tracers is shown in figure 1.19 (b) for DLCA gels at different ϕ values.

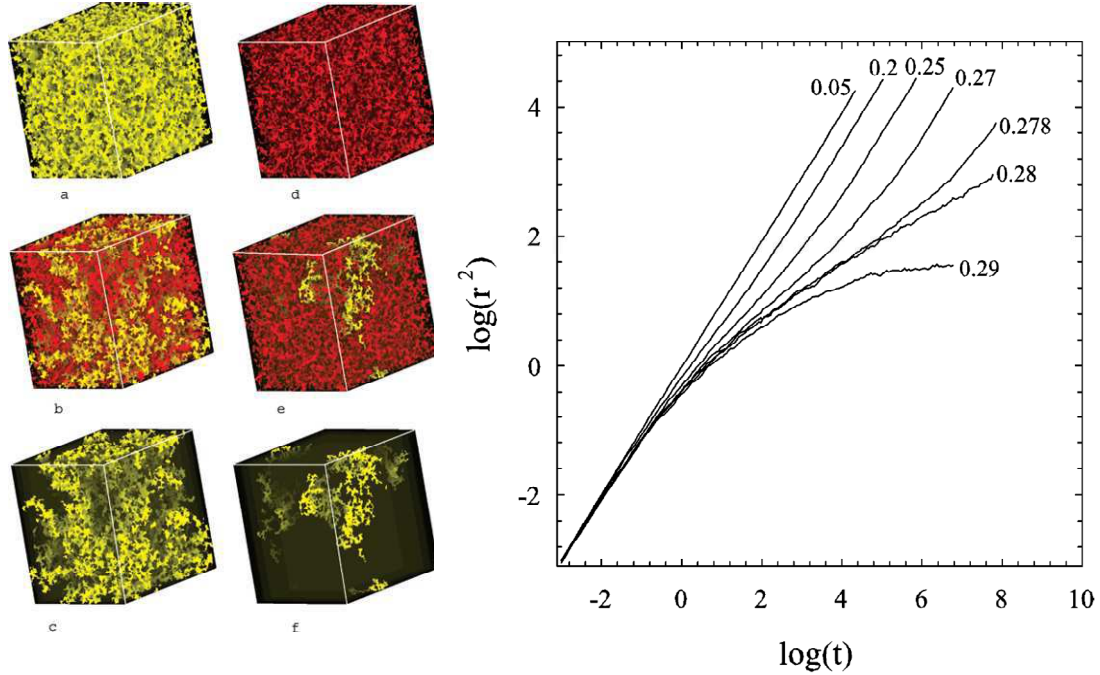


Figure 1.19. (a) Shows images of accessible volume for DLCA gels at different volume fraction. Percolating pores are yellow and isolated pores are red. For clarity images of the percolating pore of the systems in parts b and e are shown separately in c and f, respectively. Figure 1.19. (b) Mean square displacement averaged over many tracers for DLCA gels at different volume fractions (Babu et al., 2008).

Tracers diffuse freely until they hit the obstacles after which the diffusion is anomalous until the MSD of the tracer exceeds a characteristic value, called the correlation length of the percolating pores. At longer distances it becomes again diffusional with a reduced diffusion coefficient. When $\phi > \phi_c$, then all tracers are trapped in the isolated pores and hence the MSD of the tracers stagnates at long times.

An interesting result of this investigation was that the diffusion of spherical particles in these above mentioned systems were mainly determined by the volume fraction that is accessible to the tracers irrespective of the gel structure, gel volume fraction and tracer size. Figure 1.20 (a) shows the dependence of the long time diffusion

coefficient relative to the free diffusion on the accessible volume for DLCA and RLCA gels and frozen hard spheres. From the graph it is clear that for given accessible volume, the diffusion coefficient of the tracers is same for these systems and it decreases with decreasing accessible volume. Remarkably, when the accessible volume was lower than 3% then all the tracers were trapped in the matrix regardless of the gel structure.

The effect of the tracer size on the accessible volume was investigated by varying the tracer size from 0.1 to unity; see figure 1.2 (b). ϕ_a decreased with increasing tracer size and for a point tracer it was $1-\phi$.

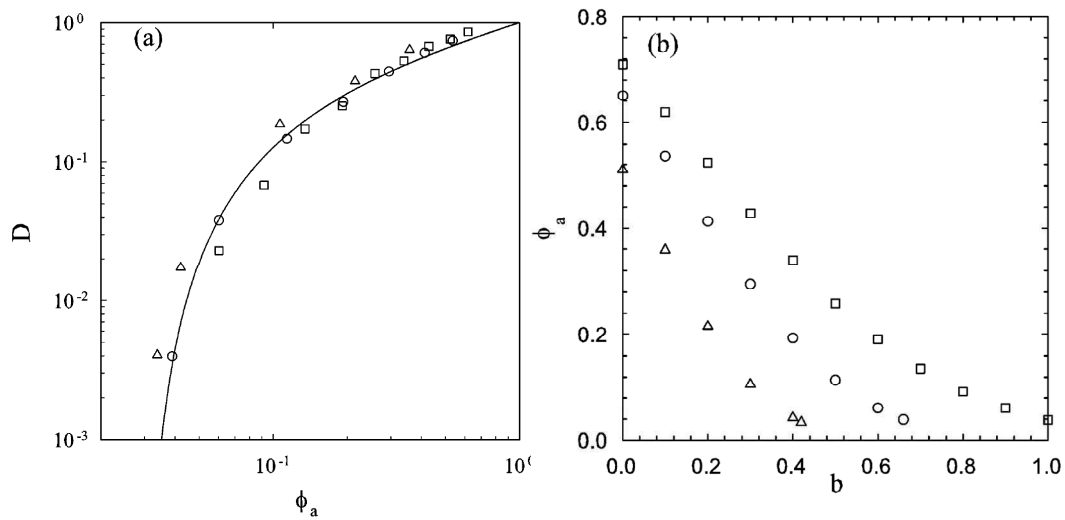


Figure 1.20. (a) Dependence of the long time diffusion coefficient relative to the free diffusion on the accessible volume for DLCA (circles) and RLCA (squares) gels and frozen hard spheres (triangles). Figure 1.20. (b) Dependence of the accessible volume on the tracer size for DLCA (circles) and RLCA (squares) gels and frozen hard spheres (triangles) (Babu et al., 2008).

1.3.2.3. Experiment

1.3.2.3.1. Methods to determine diffusion coefficient

There exist several methods to determine the global and local diffusion properties. Nuclear magnetic resonance diffusometry (NMRD) is a powerful technique to measure the diffusion of solutes, which allows one to measure the diffusion coefficient down to $10^{-15} \text{ m}^2\text{s}^{-1}$ with high accuracy. The disadvantage of this technique is that it requires flexible diffusants. Other techniques exploit CLSM to determine the displacement of particles. In the following sections we will discuss in more detail about two such techniques: multiple particle tracking and fluorescence recovery after photobleaching.

1.3.2.3.2. Fluorescence recovery after photobleaching (FRAP)

Fluorescence recovery after photo bleaching is a useful technique to measure the diffusion coefficient of the tracers in various medias and was developed by Peters et al. (Peters, Peters, Tews, & Bahr, 1974) and Axelrod et al. (Axelrod, Koppel, Schlessinger, Elson, & Webb, 1976). In this technique, an intense laser beam is used to photobleach the fluorescence of tracers in a small region of the sample followed by measurement of the recovering of the fluorescence intensity due to diffusion of the unbleached tracers to this region, see Figure 1.21 (Lorén, Nydén, & Hermansson, 2009).

In a typical FRAP experiment a cylindrical region of the sample is bleached and it is assumed that the intensity recovery in the bleached region is dependent only on the diffusion of the fluorochromes in the plane perpendicular to the cylinder. With the proper set-up there is a linear relationship between the intensity and fluorochrome concentration. The combination of FRAP and CLSM allows one to determine transport in different parts of the system with a good precision.

The length scale of structural heterogeneity and the size of the bleached region is important when FRAP is done on a heterogeneous material (Lorén et al., 2009). Such a situation may occur in phase separated and gelled systems and is illustrated in figure 1.22. Figure 1.22 (a) shows a situation where the size of the bleached region is much smaller than the distance between the different parts of the system and covers a single homogeneous domain. Figure 1.22 (b) shows a situation where the size of the bleached region covers several parts of the heterogeneous media. In this case the effect of the

structural heterogeneity will be averaged. The average diffusion of the tracer particles depends on the diffusion rate and the equilibrium solubility in different parts of the system. There have been several studies of FRAP in biopolymer gels. Here we will discuss one typical example.

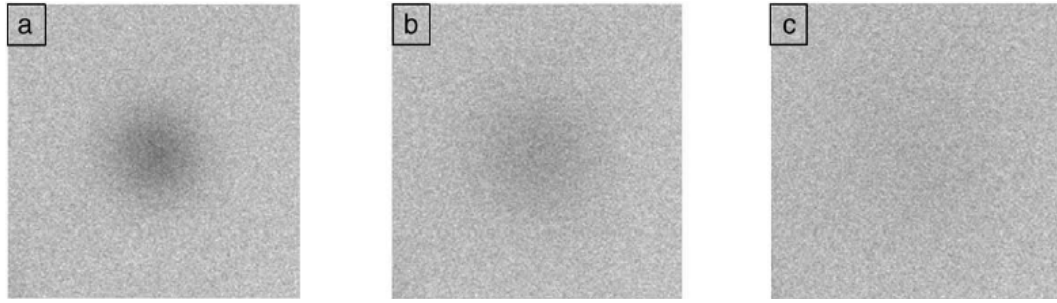


Figure 1.21. FRAP experiment in a homogeneous solution of 20 wt % polyethylene glycol (PEG) and water (Jonasson, Lorén, Olofsson, NydeÏ n, & Rudemo, 2008). The figure shows CLSM images directly after bleaching (a), 2s after bleaching (b) and 8s after bleaching (c). The image size is 120 μm and size of the bleached region is 30 μm .

Hagman et al (Hagman, Lorén, & Hermansson, 2010) studied the sol-gel transition of gelatin using FRAP and rheology. For this study Na₂-fluorescein, 10 kDa FITC-dextran, and 500 kDa FITC-dextran were used as the diffusing probes and the concentration of gelatin was 2% w/w. The temperature of the gelatin solution was quenched from 60⁰ C to different temperatures, 15, 20 and 25⁰ C. The diffusion curves were normalized to remove the temperature effect caused by quenching. Figure 1.23 shows the diffusion rate and the moduli as a function of time for different temperatures and for different probes at 2% gelatin.

From figure 1.23 it is clear that the fluorescein molecules diffuse faster than the other two probes and D/D_0 is constant before and after gelation. This indicates that the size of the fluorescein molecule is too small to detect the structural changes during the sol-gel transition. The D/D_0 values of 10 and 500 kDa FITC-dextran decrease rapidly after quenching until they reach a plateau. If the plateau is reached before the gel point, the structure of the gel is similar to that of the aggregates formed before gelation. Larger

FRAP probes can detect the structural changes in the gelatin before percolation when the gelation is slow, see Figure 1.23 (b) and 1.23 (c).

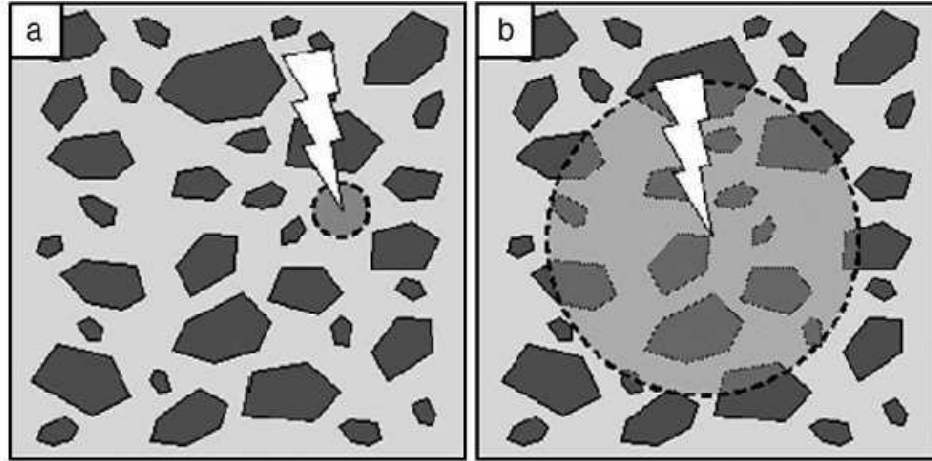


Figure 1.22. Photobleaching in heterogeneous media. (a) The bleaching region covers one single phase; (b) the bleaching region includes several parts of the heterogeneous media (Lorén et al., 2009).

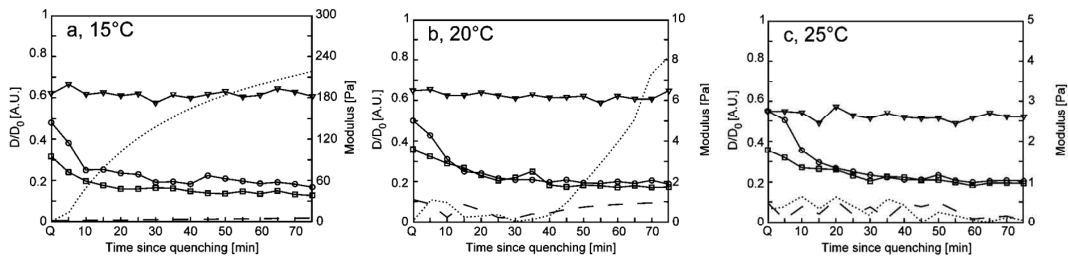


Figure 1.23. Diffusion rate and modulus of the gel as a function of time: 2% gelatin gels with fluorescein (triangles), 10 kDa FITC dextran (squares), and 500 kDa FITC-dextran (circles). The dotted line represents G' , the dashed line represents G'' ; (a) quenched to 15 °C, (b) quenched to 20 °C, (c) quenched to 25 °C. Note the difference in the y axis scale for the modulus. The solid lines are to guide the eye

As expected, the D/D_0 of the tracer in the solutions as well as in the gels was found to decrease with increasing gelatin concentration.

1.3.2.3.3. Multiple-particle tracking (MPT)

In multiple particle tracking (MPT), trajectories of particles are monitored as a function of time using CLSM (Crocker & Grier, 1996). As an example, figure 1.24 shows individual particle trajectories recorded over a time period of 17 s for fluorescent microspheres with radius $R=0.25\ \mu\text{m}$ embedded in (A) 60% glycerol solution (viscosity $0.010\ \text{Pa s}$) and (B) 88% glycerol solution (viscosity $0.147\ \text{Pa s}$) (Moschakis, Murray, & Dickinson, 2006).

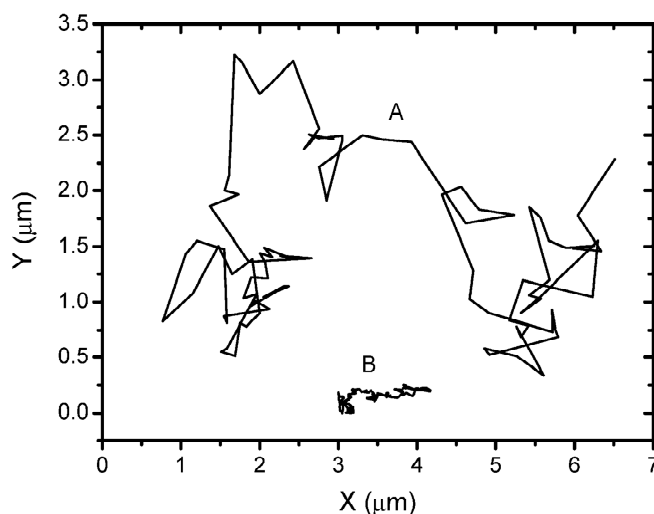


Figure 1.24. Representative individual particle trajectories recorded over a time period of 17 s for $R=0.25\ \mu\text{m}$ fluorescent microspheres embedded in (A) 60% glycerol solution (viscosity $0.010\ \text{Pa s}$) and (B) 88% glycerol solution (viscosity $0.147\ \text{Pa s}$) (Moschakis et al., 2006).

The mean square displacement (MSD) is determined from the ensemble of particle trajectories. The MSD can be related to the molecular diffusion rates by assuming different transport mechanisms such as normal diffusion where the MSD increases linearly with time, or anomalous diffusion or hindered diffusion where the MSD increases with a weaker power law exponent. Figure 1.25 shows a log-log plot of MSD versus time for microspheres with $R=0.1\ \mu\text{m}$ in dilute xanthan solutions for different concentrations. All the data in Figure 1.25 lie on straight lines of slope one.

For normal diffusion, the mean square displacement (MSD) averaged in the x - and the y -direction is related to the diffusion coefficient of the particles:

$$\langle r^2 \rangle = (\langle X^2 \rangle + \langle Y^2 \rangle) / 2 = 2Dt \quad 1.11$$

Where $\langle r^2 \rangle$ is the ensemble average MSD.

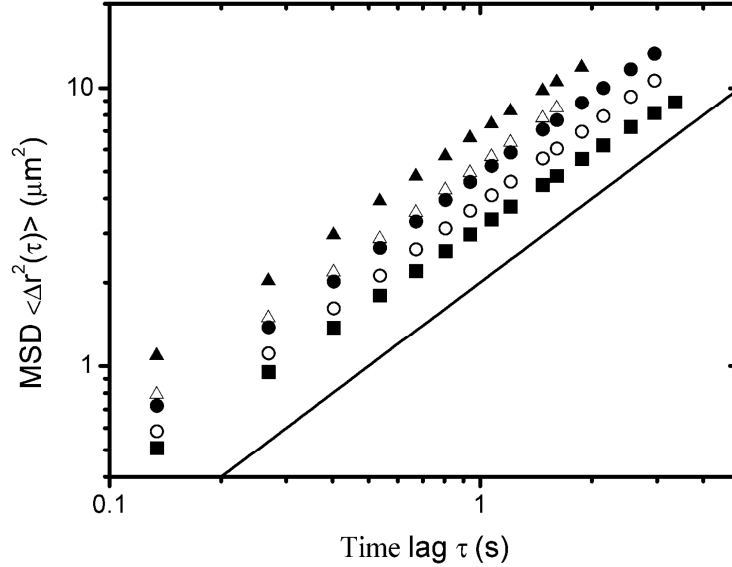


Figure 1.25. Ensemble-average mean-square displacement (MSD) of particles with $R=0.10 \mu\text{m}$ as a function of time at 20°C in xanthan solutions of different concentrations (0.03, 0.04, 0.05, 0.06 and 0.07 w/v%). The straight line has a slope of unity (Moschakis et al., 2006).

MPT can be used to probe the heterogeneity of the protein gels by monitoring the diffusion of particles through pores of the gel (Cucheval, Vincent, Hemar, Otter, & Williams, 2009). In some cases the tracers can be trapped in less rigid gels and in that case the displacement of the trapped particles reflects the elasticity of the gel. This method is called microrheology and has been used for studying the local viscoelastic properties of the surrounding medium (Moschakis et al., 2006).

1.3.3. Tracer diffusion in protein solutions and gels

Diffusion of molecular probes has been widely investigated in protein systems like casein and β -lactoglobulin gels. Colsenet et al (Colsenet, Soderman, & Mariette,

2006a, 2006b) studied the self diffusion of poly(ethylene glycol) (PEG) in whey protein solutions and gels, using Pulsed Field Gradient NMR. They have investigated the effect on the diffusion of molecular probes of the probe size, the protein concentration and the structural changes during gelation. PEG chains with three different molecular weights, 1080, 8500 and 82250 g/mol were used.

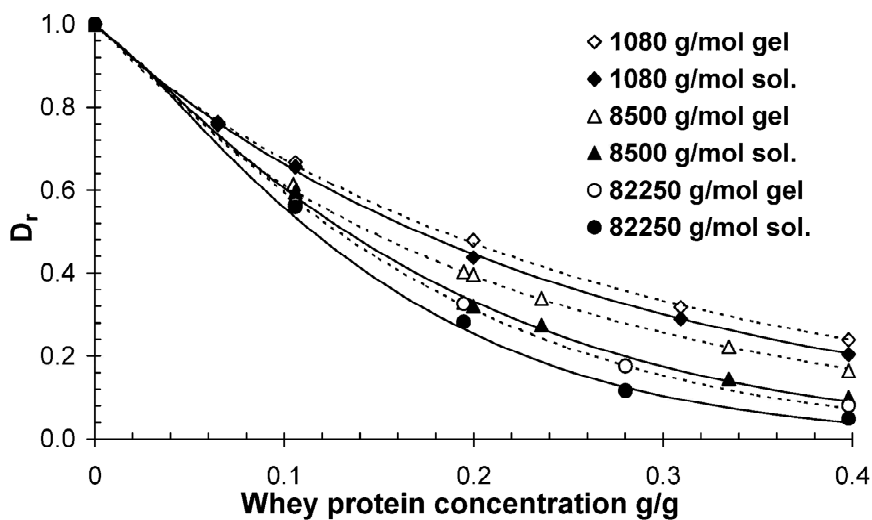


Figure 1.26. Diffusion coefficient of PEG with different molecular weights as a function of whey protein concentrations in solutions and gels (pH 6.8 and no added salt) at 20 °C (Colsenet et al., 2006b).

Figure 1.26 shows the plot diffusion coefficient of the PEG chains as a function of the proteins concentration in solutions and gels at 20 °C. D decreased with increasing protein concentration in both solutions and gels. The decrease of D with the whey protein concentration is stronger for larger probes. Also it is clear from the graph that, at a given concentration, the diffusion of the probes was faster in gels than in solutions. Colsenet et al (Colsenet et al., 2006b) also studied the effect of the type of protein on the self diffusion of PEG both in solutions and gels. They used casein and whey proteins with diameters 100 nm and 2 nm, respectively. Figure 1.27 shows the diffusion coefficient in casein and whey protein solutions as a function of the protein concentrations. In both systems D decreased with increasing proteins concentration, but the extent of the decrease

strongly depended on the type of the protein. The authors suggested that the slower diffusion of in the casein solutions due to their larger size.

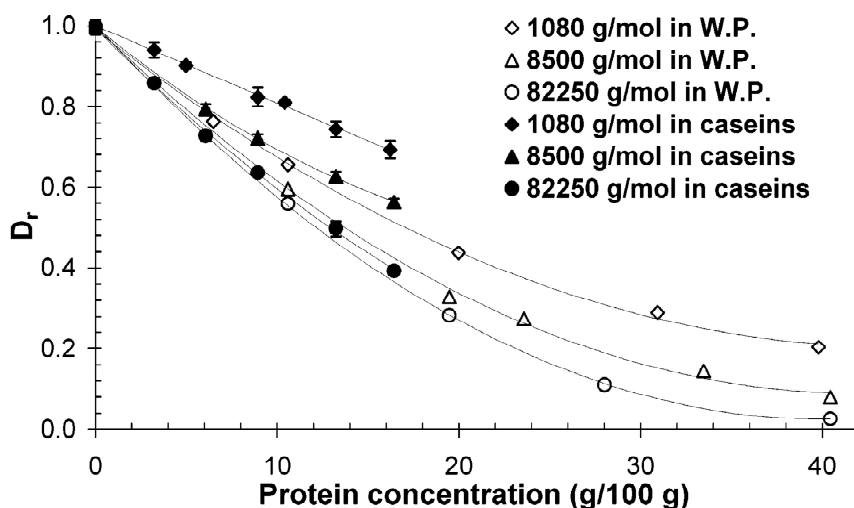


Figure 1.27. Diffusion coefficient of PEG with different molecular weights as a function of the protein concentration in casein and whey protein solutions (Colsenet et al., 2006b).

Croguennoc et al (Croguennoc, Nicolai, Kuil, & Hollander, 2001) studied the self diffusion of dextran with three different molecular weights (1.7×10^6 , 2.5×10^5 and 6.2×10^4 g/mol) in β -lg gels at 70g/l (0.1M NaCl and pH 7). Figure 1.28 shows the variation of D of the three dextran probes as a function of heating time at 70 °C. They found that the diffusion coefficient decreased with increasing heating time around the gel time and then remained constant. The decrease of D was stronger for the larger probes.

The authors suggested that this decrease could be explained on the basis of the friction experienced by probes. Native β -lg is small and can easily penetrate the dextran chains, so the friction between dextran and native β -lg small is small. However, more and larger aggregates are formed with heating time which increases the effective volume fraction of the β -lg and thus enhances the obstruction for the dextran chains. This explains why the diffusion coefficient of the probes decreased with increasing heating time. At the gel point an immobile structure is formed and this structure varies little with further heating time and hence the diffusion coefficient remained constant.

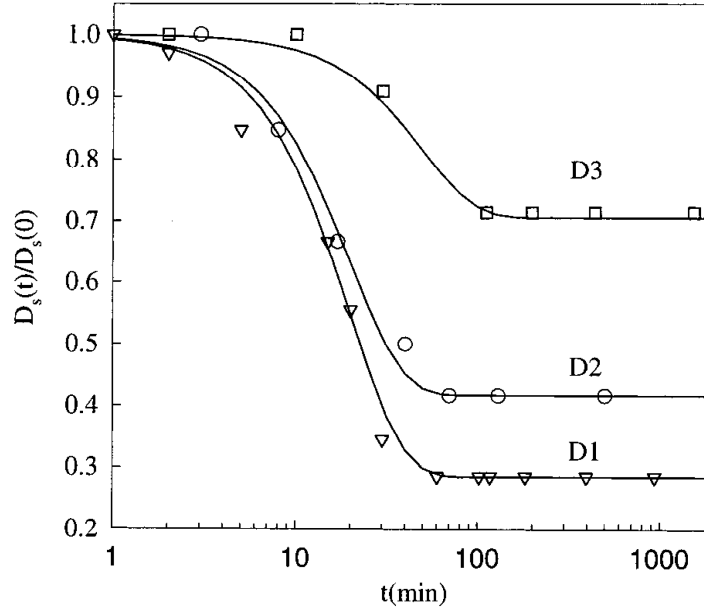


Figure 1.28. Diffusion coefficient of dextran with different molecular weights ($D1=7 \times 10^6$ g/mol, $D2=2.5 \times 10^5$ g/mol, $D3=6.2 \times 10^4$ g/mol) in a gelling β -lg solution as a function of heating time at 70°C for $C=70$ g/l at 0.1 M NaCl and pH 7.

1.3.4. Diffusion of particles at the oil water interface

Tarimala et al (Tarimala, Ranabothu, Verneti, & Dai, 2004) investigated the mobility of charged micro particles at the poly (dimethylsiloxane)-water interface using CLSM. The mean square displacement of the probes was calculated from the movements of particles between subsequent images. They calculated the diffusion coefficient of the particles in water and at the interface from the relation $MSD=4.Dt$. Figure 1.29 shows the MSD of the particles dispersed in water and at the oil-water interface.

They observed that the diffusion coefficient of the particles at the oil water interface was only moderately smaller compared to that in the bulk. Figure 1.30 shows the diffusion coefficient at the interface versus the viscosity of the oil phase. It was found to be proportional to the viscosity of the oil phase implying that the effective viscosity felt by the particle at the interface was mainly controlled by the phase with the higher viscosity. They conducted the experiments on both oil-in-water and water-in-oil emulsions, but they found only a minor influence on the particle diffusion.

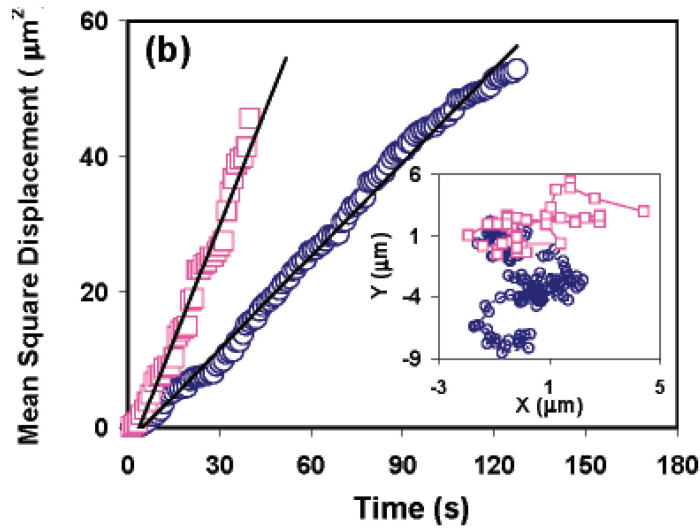


Figure 1.29. Mean square displacement of particles dispersed in water (squares) and at the oil-water interface (circles). The solid lines represent linear regressions. The inset shows the trajectory of the particle movement; the time between each point is 1 s (Tarimala et al., 2004).

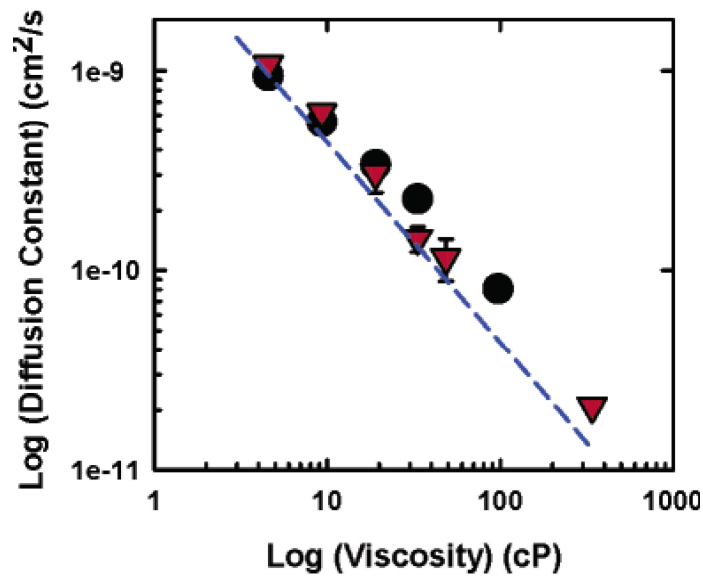


Figure 1.30. Effect of poly(dimethylsiloxane) (oil) viscosity on the diffusion coefficient of single polystyrene particles at the interface in oil-in-water type (triangles) and water-in-oil type (circles) Pickering emulsions. The dashed line is calculated on the basis of the Stokes-Einstein relation if the particles were dispersed in the bulk oil phase.

Tarimala et al (Tarimala et al., 2004) also studied the in-situ aggregation of charged micro particles at the oil-water interface with CLSM. They suggested that every collision of the particles at the interface led to aggregation and hence the structure formation is due to diffusion limited cluster aggregation. Figure 1.31 shows how a single particle, a trimer, and pentamer did a random walk and then attached to the large clusters.

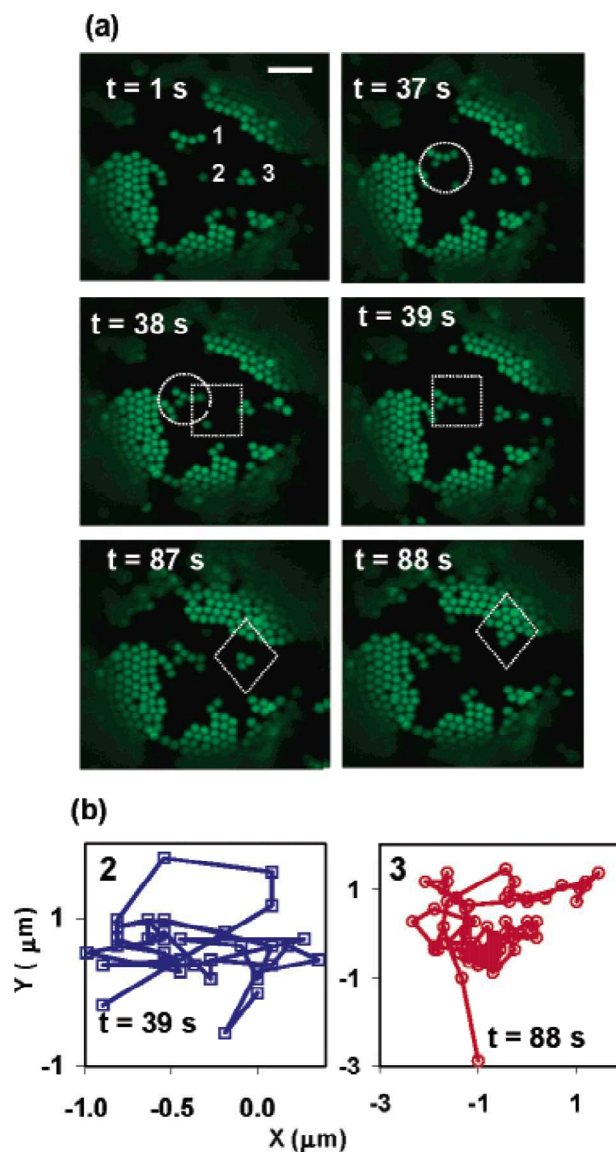


Figure 1.31. (a) CLSM images showing the aggregation of polystyrene particles at the poly (dimethylsiloxane)-in water Pickering emulsion interface. The circles, squares, and diamonds highlight locations before and after particle attachment. (b) Trajectories of the single particle (2) and the three-particle cluster (3) before aggregation. At $t=0$, the positions were set to be at $(0, 0)$. The scale bar is $5 \mu\text{m}$ (Tarimala et al., 2004).

Materials and Methods

2. Materials and methods

2.1. Materials

2.1.1. Proteins

In this study β -lg is used as the protein matrix and it consisted of a mixture of variants A and B in about equal quantities. β -lg solution was prepared by dissolving the protein powder in pure water (Millipore) that contained 3mM Sodium azide to prevent bacterial growth. The pH of the solution was set at 7 by adding small amounts of a 0.1M NaOH solution. The solution was filtered through 0.45 μ m pore size filters after which the protein concentration was determined by measuring the UV absorption at 280 nm using extinction coefficient 0.96 l g⁻¹cm⁻¹ (Townend, Winterbottom, & Timasheff, 1960). The ionic strength was set by adding small amounts of a concentrated NaCl solution. Gels were prepared by heating the solutions at 80⁰ C for 24 hours.

In order to visualize the gel structure, β -lg was labeled with either Rhodamine B isothiocyanate (RhB) or Fluorescein isothiocyanate (FITC) by adding a small amount of a concentrated dye solution to the β -lg solution before heat treatment. A laser beam with wave length λ =543 nm excited RhB and fluorescence light was recorded between 560-700 nm. A laser beam at λ =448 nm excited FITC and the emission was recorded between 560-700 nm. Figure 2.1 shows the absorbance (a) and the emission spectra (b) of RhB and FITC. Sometimes the gel and particle phases were visualized separately so-called multi fluorescent labeling.

2.1.2. Particles

Fluorescent polystyrene latex particles with radii 0.1, 0.25, 0.5, and 1 μ m were used as tracer particles. The particles were covered with a layer of poly(ethylene oxide) (PEO) in order to avoid interaction with the protein gel. To this end, particles were suspended in a solution of PEO (M_w =5 \times 10⁵ g/mol) for 24 hours. DLS measurements were done on the particles before and after PEO treatment. The difference between the hydrodynamic radii of the PEO coated particles and the bare latex particles give the

thickness of PEO covering. The dynamic light scattering showed that the hydrodynamic radius of the smallest particles increased by 20 nm due to PEO covering.

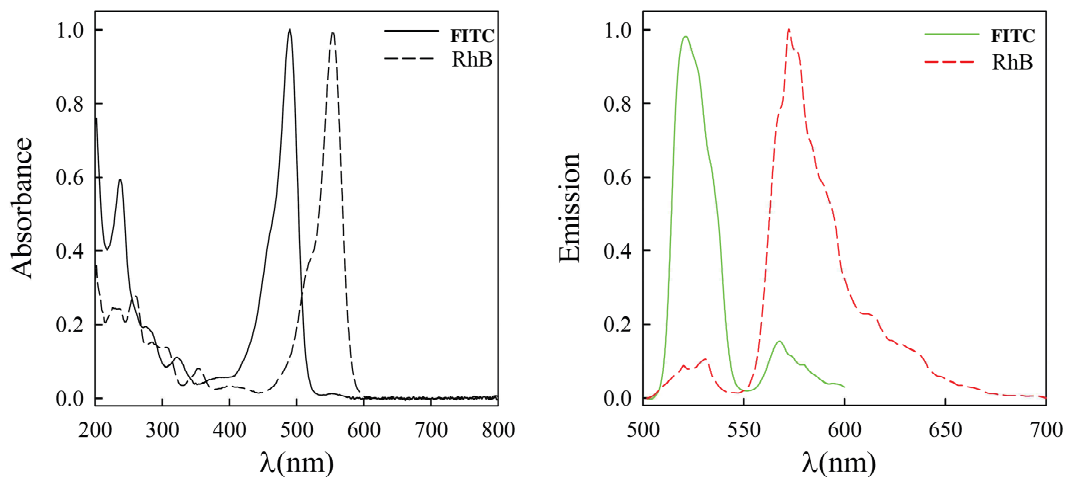


Figure 2.1. Absorbance (a) and emission spectra (b) of Rhodamine B and FITC (Ako, 2010).

Fluorescein labeled dextran molecules with different molecular weights were used for the FRAP measurements: d40k, d500k and d2000k with molecular weights 4×10^4 , 5×10^5 and 2×10^6 g/mol, respectively. Dynamic light scattering was used to measure the z-average hydrodynamic radius (R_{hz}) of the tracers: 5.5, 23, and 50 nm for d40k, d500k and d2000k, respectively. The tracer concentration was varied between 20 and 30 ppm.

Contrary to the latex particles, the dextran chains are polydisperse as clearly seen in figure 2.2.

2.1.3. Poly(ethylene oxide) (PEO) and dextran

PEO ($M_w = 2 \times 10^5$ g/mol) and dextran ($M_w = 5 \times 10^5$ g/mol) were purchased from Sigma Aldrich. Dextran was used without any further purification whereas PEO contained a small amount of silica particles which were removed by centrifugation and filtration. This was found to be important for the trapping of particles in the interface of PEO-dextran emulsions, otherwise the interface might be saturated with silica particles, which prevents the latex particles to enter the interface. Figure 2.2 shows chromatographs of the PEO and dextran samples used in this study.

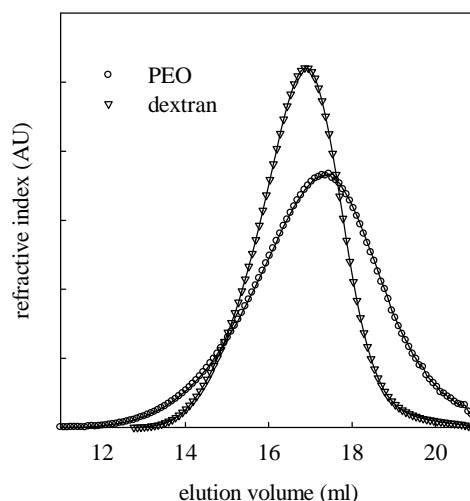


Figure 2.2. Chromatographs of the PEO and dextran samples used in this study

2.2. Methods

The main technique used for this investigation was confocal laser scanning microscopy. Here we explain this technique and its application to tracer diffusion measurements in some detail. Other experimental techniques that were used will only be described briefly.

2.2.1. Confocal laser scanning microscopy (CLSM)

The basic concept of confocal laser scanning microscopy was originally developed by Mirvin Minsky in the 1950s when he was a postdoctoral student at Harvard University. But at first, Minsky's invention remained largely unnoticed due to lack of intense light sources and computer requirements for handling large amounts of data. During the late 1970s and the 1980s, advances in computer and laser technology, coupled to new algorithms for digital manipulation of images, led to a growing interest in confocal microscopy.

The method of image formation in confocal microscopy is different from conventional microscopy where the whole specimen is illuminated from a mercury or xenon source and the image can be directly viewed by eye. A laser scanning confocal microscope incorporates two ideas: point by point illumination of the specimen from a

laser source and rejection of out of focus light with a pinhole aperture situated in front of the detector. The basic configuration of a modern laser scanning microscope is shown in figure 2.3. The light from the laser source passes through a pinhole aperture that is situated in a conjugate plane (confocal) with a scanning point on the specimen. For scanning, the microscope uses a dichromatic mirror that reflects light shorter than a certain wavelength but transmits light of longer wavelength. Thus the light from the laser source is reflected and scanned across the specimen in a defined focal plane, by the dichromatic mirrors. The fluoresced (higher wave length) light from the sample passes back through the objective and is descanned by the same mirrors used to scan the sample. Before it reaches the detector, the fluoresced light passes through the pinhole which is placed in the conjugate focal (hence the term confocal) plane of the sample. The significant amount of fluorescence emission that occurs at points above and below the objective focal plane is not confocal with the pinhole and hence most of this out of focus light is not detected by the photomultiplier tube and does not contribute to the resulting image. In confocal microscopy, there is never a complete image of the specimen because at any instant only one point is observed. Thus, for visualization, the detector is attached to a computer, which builds up the image, one pixel at a time. The speed of most confocal microscopes is limited by the rate at which the mirrors can scan the entire sample plane. This particular type of fluorescence microscopy, in which the objective used by the illuminating light is also used by the fluorescence light in conjunction with a dichroic mirror, is called epifluorescence.

2.2.2. Principles of fluorescence

Fluorescence is the property of some atoms and molecules to absorb light at a particular wavelength and to subsequently emit light of longer wavelength after a brief interval, termed the fluorescence lifetime. At ordinary temperatures, most of the molecules are in their ground state. However they may absorb a photon and excite an electron to a higher energy discrete singlet state. In figure 2.4, this state is represented by a top black line. Typically, the molecule quickly (within 10^{-8} sec) dissipates some of the absorbed energy through collisions with surrounding molecules causing the electron to drop to a lower energy level (the second black line in the figure 2.4). If the surrounding molecules are not able to accept the larger energy difference needed to further lower the molecule to its ground state, it may undergo spontaneous emission, thereby losing the

remaining energy, by emitting light of a longer wavelength (Atkins, 1994). Fluorescein is a common fluorophore that acts this way, emitting green light when stimulated with blue excitation light. The wavelengths of the excitation light and the color of the emitted light are material dependent. Microscopy in the fluorescence mode has several advantages over the reflected or transmitted modes. It can be more sensitive and, often, it is possible to attach fluorescent molecules to specific parts of the specimen, making them the only visible ones in the microscope. It is also possible to use more than one type of fluorophore (Tsien & Waggoner, 1995). Thus, by switching the excitation light, different parts of the specimen can be distinguished.

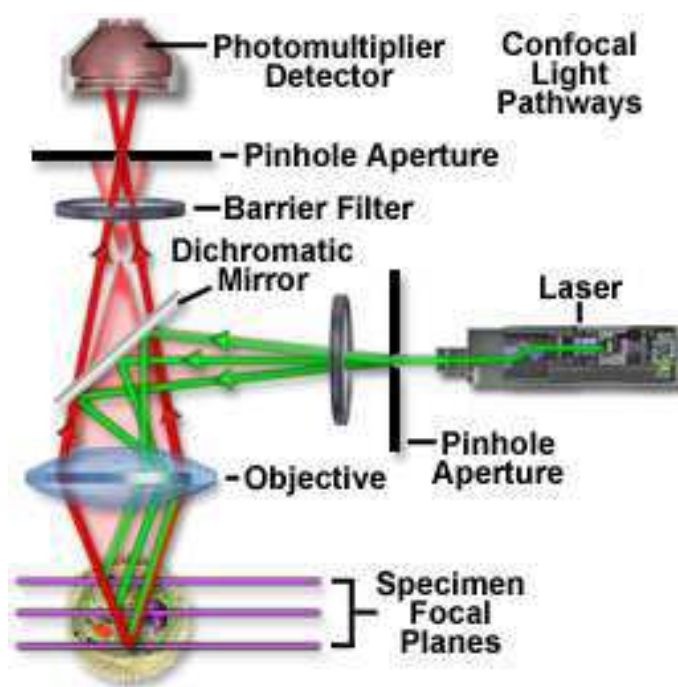


Figure 2.3. Illustrating the basic configuration of a modern confocal laser scanning microscope

2.2.3. Parameters of fluorescence

Three fundamental parameters are used to describe the process of fluorescence: molar extinction coefficient, quantum efficiency (ϕ_f) and fluorescence lifetime (t).

2.2.3.1. Molar extinction coefficient

The molar extinction coefficient is the measure of how strongly a chemical species absorbs light at a given wave length. The extinction coefficient is determined by measuring the absorbance at a reference wavelength (characteristic of the absorbing molecule) for one molar (1 M) concentration of the target chemical in a cuvette having a one-centimeter path length. The reference wavelength is usually the wavelength of maximum absorption in the ultraviolet or visible light spectrum. The relationship is described by the Beer-Lamberts law:

$$I_t = I_0 e^{-\varepsilon c l} \quad 2.1$$

where ε is the molar absorptivity, l is the distance travelled by the light through the material, c is the molar concentration of the species, and I_t and I_0 are the intensity of the transmitted and incident light respectively. Chromophores having a high extinction coefficient also have a high probability of fluorescence emission.

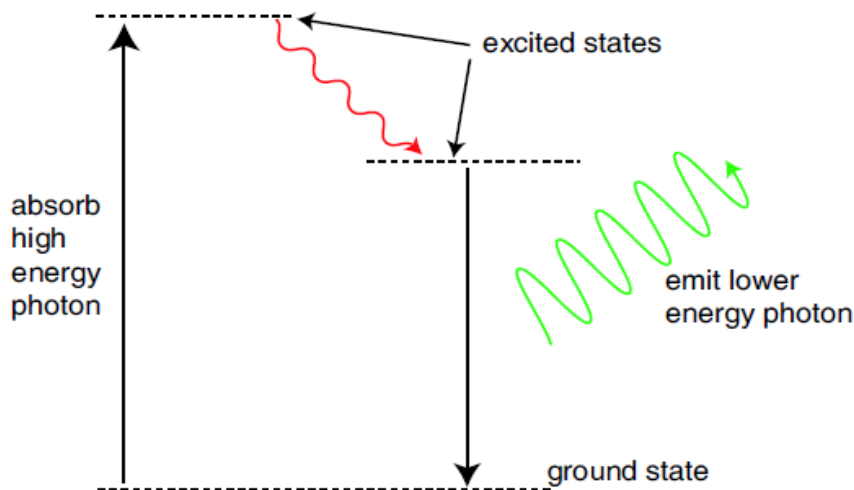


Figure 2.4. Horizontal lines indicating the quantum energy levels of the molecule. The upward arrow indicates the excitation of a fluorescent molecule by absorbing a high energy photon. It drops some energy to the neighboring molecules and de-excites to a lower energy excited state. Subsequently, it attains the ground state by emitting a photon.

2.2.3.2. Quantum efficiency

Quantum efficiency is defined as the ratio of photons emitted to the number of photons absorbed. In other words, the quantum yield represents the probability that a given excited fluorochrome will produce an emitted photon. Fluorescent molecules commonly employed as probes in microscopy have quantum yields ranging from very low (0.05 or less) to almost unity (the brightest fluorophores)

$$\varphi_f = \frac{N_e(\text{number of photons emitted})}{N_a(\text{number of photons absorbed})} \quad 2.2$$

2.2.3.3. Fluorescence lifetime

The fluorescence lifetime is the characteristic time that a molecule remains in an excited state prior to returning to the ground state and is an indicator of the time available for information to be gathered from the emission profile. When in the excited state, a fluorophore can undergo conformational changes as well as interact with other molecules and diffuse through the environment. The following equation gives the decay of fluorescence as a function of time.

$$I_t = I_0 e^{\left(\frac{-t}{\tau}\right)} \quad 2.3$$

Here I_t is the fluorescence intensity measured at time t , I_0 is the initial intensity observed immediately after excitation, and τ is the fluorescence lifetime. The fluorescence lifetime is defined as the time in which the initial fluorescence intensity of a fluorophore decays to $1/e$.

2.2.4. Fluorophores

Many fluorescent probes are constructed around synthetic aromatic organic chemicals designed to bind with biological macromolecules like proteins or nucleic acids. The most important aspect of fluorescence confocal microscopy is the choice of the fluorophore. The fluorophore should tag the correct part of the specimen. It must be sensitive enough for the given excitation wavelength. For living specimens it should not

significantly alter the dynamics of the organism; and an extra consideration is the effect of the specimen on the fluorophore and its chemical environment that can affect the position of the peaks of the excitation and emission.

The best known fluorophores are fluorescein and its derivatives. Fluorescein has quantum efficiency close to one. But the disadvantages are that it easily photo bleaches and that it is sensitive to the ionic strength and the pH of the medium.

Rhodamine and its derivatives are also used in many studies. It binds to protein molecules by strong hydrophobic interaction. It is stable at both acidic as well as basic pH and it is less photo bleaching than fluorescein. Figure 2.5 shows the molecular structure of Fluorescein and Rhodamine B.

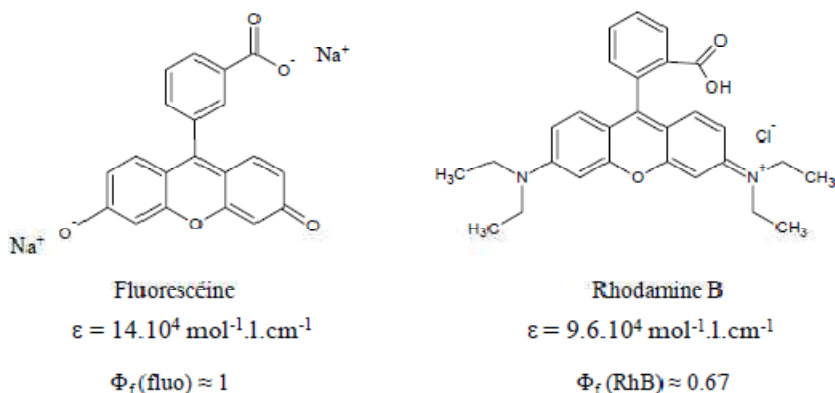


Figure 2.5. Molecular structure of fluorescein and Rhodamine B

2.2.5. CLSM Objectives

The objective is the most critical component of the system in determining the information content of the image. There are different objectives available according to the immersion medium between the lens and the cover slip of the specimen. The efficiency of an objective is determined by its numerical aperture (NA), and it is a measure of how well an objective gathers light. Higher values of the numerical aperture allow increasingly oblique rays to enter the objective front lens, producing a more highly resolved image. Image forming light waves pass through the specimen and enter the objective in an

inverted cone as illustrated in figure 2.6. A longitudinal slice of this light cone shows the angular aperture that is determined by the focal length of the objective.

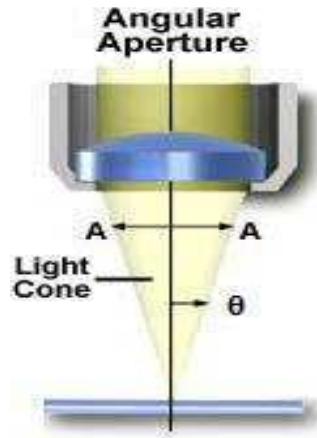


Figure 2.6. Illustration of image-forming light waves which pass through the specimen and enter the objective in an inverted cone. The angle (θ) and the angular aperture (A) are indicated in the figure.

The angle θ is one-half of the angular aperture (A) and is related to the numerical aperture through the following equation:

$$NA = n \sin(\theta) \quad 2.4$$

where n is the refractive index of the immersion medium between the front lens of the objective and the specimen cover glass, a value that ranges from 1.00 for air to 1.51 for specialized immersion oils. From the above equation it is clear that for a dry objective the maximum possible NA is 1. In practice, however, it is difficult to attain NA above 0.95 for dry objectives. Also it is clear from the above equation that to obtain higher working numerical apertures, one has to increase the refractive index of the immersion medium between the cover slip of the specimen and the front lens of the objective.

We have used two different water immersion objectives:

HCx PL APO 63x with $NA=1.2$

HCx PL APO 20x with $NA=0.7$

2.2.6. Resolution

The resolution of a microscope objective is defined as the smallest distance between two points on a specimen that can still be distinguished as two separate entities. The relationship between numerical aperture, wavelength, and resolution is given below:

$$R = 0.61 \times \frac{\lambda_{em}}{NA} \quad 2.5$$

where λ_{em} is the wavelength of the light in the immersion medium.

Confocal laser scanning microscopy has inherent resolution limitations due to diffraction. We assumed that the point source used produces a point of light on the specimen, but in fact, it appears in the focal plane as an Airy disc. These Airy discs limit the maximum resolution of the microscope in the sample plane due to the Rayleigh criterion, which states that two Airy discs must be separated by at least their radius in order to be resolved. The maximum resolution that can be attained with the confocal microscope is typically about 300nm. Airy discs consist of small concentric light and dark circles as illustrated in Figure 2.7. Figure 2.7(a) illustrates a hypothetical Airy disc that essentially consists of a diffraction pattern containing a central maximum (typically termed a zeroth order maximum) surrounded by concentric 1st, 2nd, 3rd, etc., order maxima of sequentially decreasing brightness that make up the intensity distribution. Two Airy discs and their intensity distributions at the limit of optical resolution are illustrated in Figure 2.7(b). In this part of the figure, the separation between the two discs exceeds their radii, and they are resolvable. Figure 2.7(c) shows two Airy discs and their intensity distributions in a situation where the center-to-center distance between the zeroth order maxima is less than the width of these maxima, and the two discs are not individually resolvable by the Rayleigh criterion.

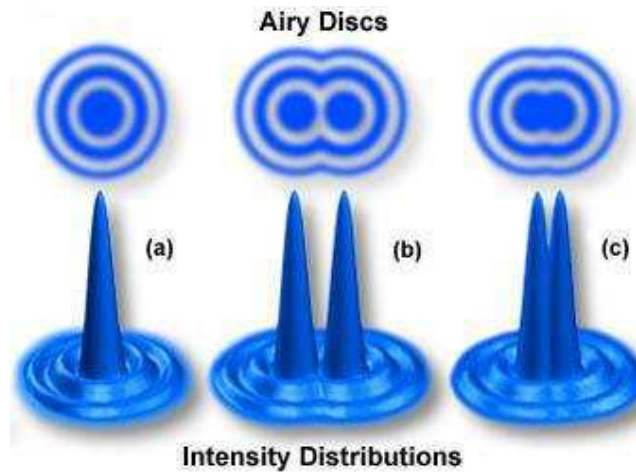


Figure 2.7. (a) Shows a hypothetical Airy disc and Airy pattern containing a center maximum or zeroth order maximum. (b) Two Airy discs and their intensity distributions at the limit of optical resolution are shown. (c) Shows two Airy discs and their intensity distributions in a situation where the center-to-center distance between the zeroth order maxima is less than the width of these maxima, and the two discs are not individually resolvable by the Rayleigh criterion.

2.2.7. Pinhole size

The strength of optical sectioning of a confocal microscope depends strongly on the pinhole size. One may think that making the pinhole as small as possible is the best choice. But in fact reduction in the pinhole size results in a reduction of number of photons detected by the detector. This may lead to a reduced signal-to-noise ratio. To offset the weaker signal more fluorescence is needed from the specimen. This usually can be done, to a limit, by raising the intensity of the excitation light. But high intensities can damage the specimen, and in the case of fluorescence, also degrade the fluorophore. Moreover, it has been shown that optical sectioning does not improve considerably with the pinhole size below a limit that approximates the radius of the first zero of the Airy disc. Thus, a good compromise is to make the pinhole about the size of the Airy disc.

2.2.8. Electronic light detectors

A photomultiplier tube consists of a classical vacuum tube in which a glass or quartz window encases the photocathode and a chain of electron multipliers, known as dynodes, followed by an anode to complete the electrical circuit.

In the side-on photomultiplier tube design, photons impact on the photocathode surface to subsequently generate photoelectrons that are ejected into the vacuum. Absorbed photons produce a free electron in the photocathode and the surplus energy is converted into kinetic energy. Electrons having sufficient kinetic energy are able to escape from the photocathode surface. These ejected photoelectrons have trajectories angled at the first dynode, which in turn produce a large quantity of electrons angled at the second dynode and so on. An electrical potential of approximately 100 volts is applied between each dynode element in the chain. Thus, the dynodes serve as electron multipliers by virtue of their geometry and the gradation in voltage between the individual elements. Finally, these amplified secondary electrons are collected by the anode as an output signal. A schematic representation of a photomultiplier tube is shown in the figure 2.8.

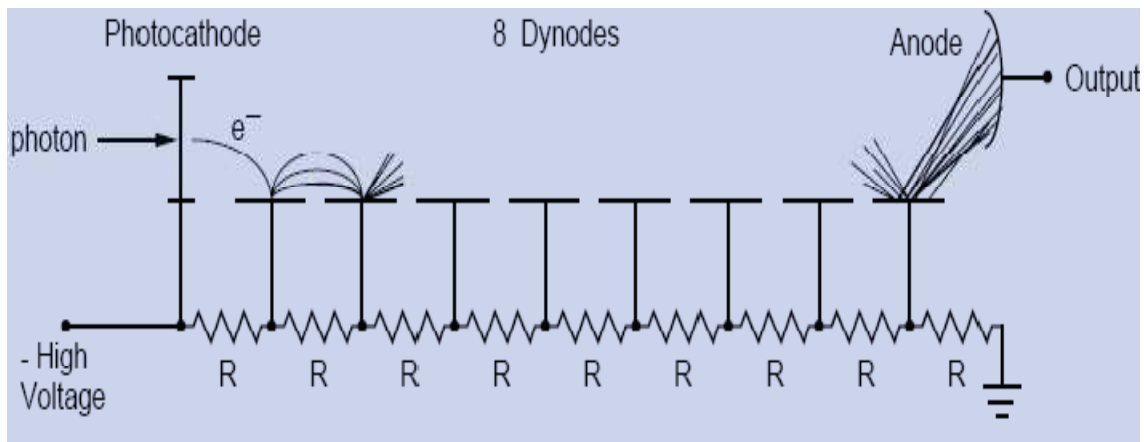


Figure 2.8. Schematic representation of a photomultiplier tube

2.2.9. Gain and offset on PMT

When a photon reaches the photo cathode in the PMT tube, it causes the release of electrons that are accelerated towards the dynodes. As they pass from one dynode to the next, the electrons multiply, and eventually are absorbed by the anode. The gain of the

PMT tube is used to increase or decrease the number of electrons produced each time an electron collides with a dynode. The gain (voltage) on the PMT has a 0 to 1000 V adjustable range. The smart offset on the PMT ranges from 0 to 100. The combination of gain and offset adjustment on the PMT can be used to produce an image with balanced intensity and background noise. A too high PMT voltage gives out more dark current and thus more background, while a too high offset cuts off too much signal and reduces the dynamic range of the image.

2.2.10. Photobleaching

The phenomenon of photobleaching occurs when a fluorophore loses permanently its ability to fluoresce due to photon induced damage. The process of photobleaching is not completely understood but it is believed that, upon transition from an excited singlet state to the excited triplet state, fluorophores may interact with another molecule to produce irreversible covalent modifications. The triplet state is relatively long-lived with respect to the singlet state, thus allowing excited molecules a much longer timeframe to undergo chemical reactions with components in the environment. The average number of excitation and emission cycles that occur for a particular fluorophore before photobleaching is dependent upon the molecular structure and the local environment. Some fluorophores bleach quickly after emitting only a few photons, while others that are more robust can undergo thousands or millions of cycles before bleaching. The photobleaching reactions lead to a dramatic loss of fluorescence emission intensity in most specimens which make fluorescence microscopy more difficult. Under certain circumstances, the photobleaching effect can also be utilized to obtain specific information that would not otherwise be available. The technique fluorescence recovery after photobleaching (FRAP) takes advantage of photobleaching, see below.

2.2.11. Image analysis

The CLSM images were analyzed with different techniques which are explained below.

2.2.11.1. Determination of local proteins concentration

The fluorescence intensity is proportional to the protein concentration in the gels [Ako et al., 2009]. Hence it is possible to measure the protein concentration in the dense phase as well as in the pores. This is done by measuring the fluorescence intensity of a large number of small areas of the phase that is under consideration (gel or pores). When measuring the intensity it is important to make sure that the chosen small regions are in focus. Figure 2.9 illustrates the measurement of the protein concentration in the dense phase.

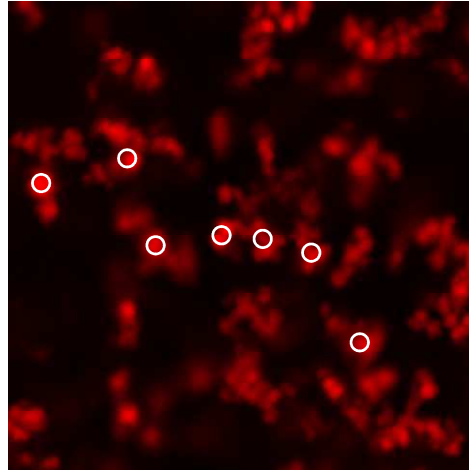


Figure 2.9. Illustrating the measurement of protein concentration in the dense phase of the gel. Scale of the image is 40 μm

2.2.11.2. Pair correlation function of CLSM images

We have insured that the intensity of the signal is proportional to the concentration of the fluorophores in the system. This means that the pair correlation of the intensities of different pixels provides a measure of the spatial distribution. In this method the intensity A_i of a random pixel i of the image is chosen and is correlated with the intensity A_j of pixel j . The pair correlation function is defined as:

$$g(r) = \frac{\sum_{i=1}^n \sum_{j=1}^m A_i \cdot A_j}{\sum_{i=1}^n A_i \cdot \sum_{j=1}^m A_j} \text{ with } r = |i - j| \quad 2.6$$

for large r values A_i and A_j are no longer correlated and hence $g(r)$ becomes unity. In order to avoid finite size effects the random pixel i is chosen in such a way that the distance from the edge to the i^{th} pixel is larger than the maximum value of r (r_{max}).

$g(r) - 1 = \sigma^2$ for r smaller than the resolution of the microscope. σ Characterizes the amplitude of the intensity fluctuations and is defined as:

$$\sigma = \langle A \rangle^{-1} \sqrt{n^{-1} \sum_{i=1}^n (A_i - \langle A \rangle)^2} \quad 2.7$$

where $\langle A \rangle$ is the spatially averaged intensity. Random fluctuations of the fluorescence intensity of the marker in time do not have any influence on $g(r)$, but it does influence the value of σ . The effect of fluctuations of the fluorescence can be reduced by increasing the marker concentration or averaging over several images. The routine to calculate $g(r)$ is explained in annex 3.

In practice the minimum useful value of r corresponds to the resolution of the microscope. It was found that the best resolution was obtained with a HCx PL APO 63x water immersion objective and is theoretically 0.3 μm in the x-y plane, but in the z-direction (perpendicular to the objective) it is 0.6 μm . Fortunately, for isotropic systems like protein gels it is sufficient to correlate the pixel intensities as a function of r in the x-y plane.

Figure 2.10. shows an example of $g(r)$ for different zooms and objectives before (a) and after superposition (b). By analyzing images of the same system with different zooms and with two different lenses a broad range of r could be covered.

For the protein gels studied here, the decay $g(r)$ could be described by a stretched exponential:

$$g(r) - 1 = B_1 \exp[-(r/\xi)^\beta] \quad 2.8$$

where B_1 is the contrast, ξ is the correlation length and β is the stretching exponent. However, this function failed to describe the weak minimum of $g(r)$ observed at larger r values.

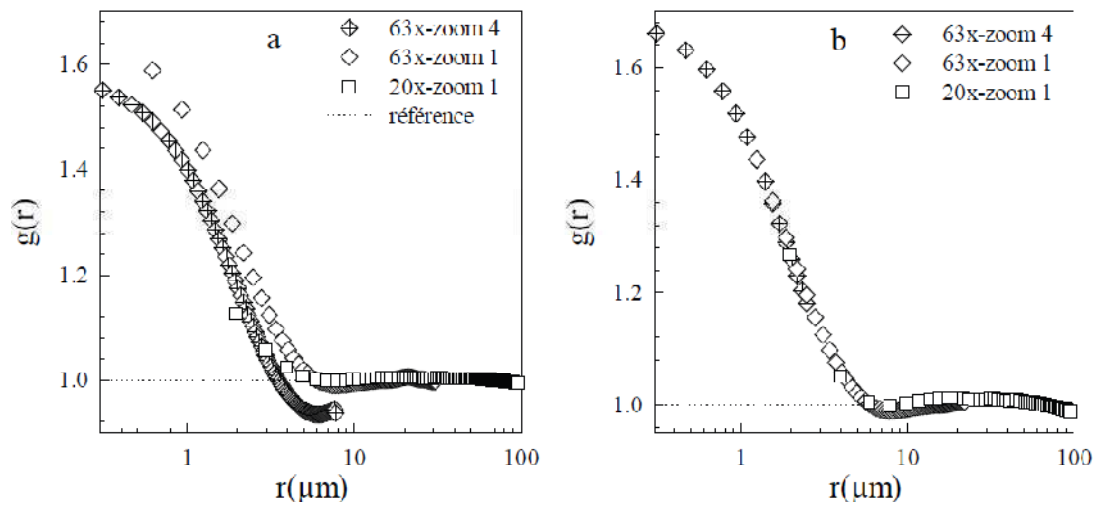


Figure 2.10. $g(r)$ as a function of r for different zooms and objectives before (a) and after superposition (b).

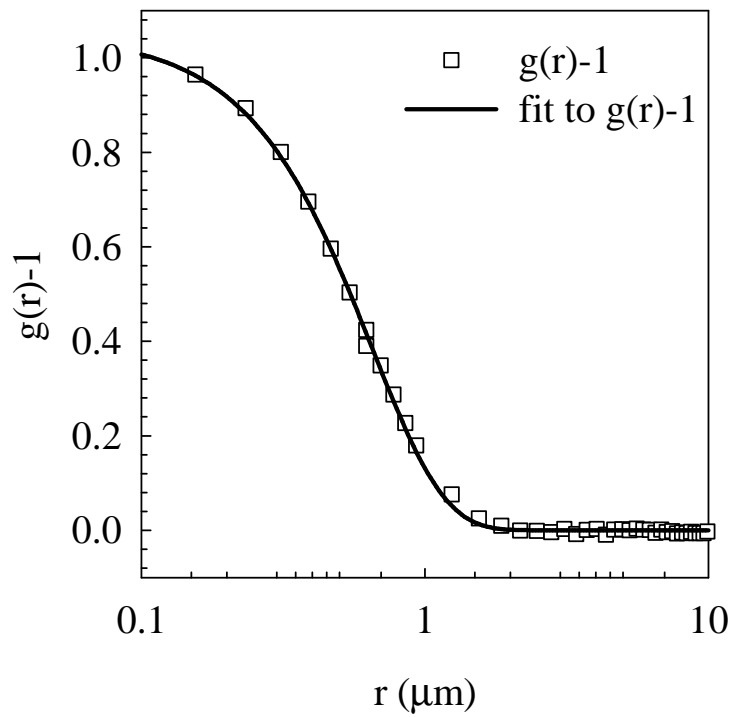


Figure 2.11. $g(r)-1$ for a b-lg gel formed at $C=20$ g/l, $C_s=0.15$ M and at pH 7. The solid line represents a fit to Eq. 2.8

2.2.12. Multiple-particle tracking

As mentioned in the Bibliography, this technique involves monitoring the trajectories of particles as a function of time with CLSM for different time intervals (Δt) between images. The movie of the particle displacement was analyzed with a particle tracking routine developed by Crocker and Weeks. (Crocker, JC and Grier DG., 1996; Crocker JC, and Weeks ER, <http://www.physics.emory.edu/weeks/idl/tracking.html>) to determine the parameters of diffusion. The smallest time interval between the images was 0.3 s, but in general results obtained with several time intervals were compared. Fluorescent polystyrene latex particles with radii between 0.1 and 1 μm were used as tracer particles. The particle concentration was kept very low so that individual tracers could be tracked with little ambiguity. In general, images contained around 100 particles. Some variation of the particle concentration did not give systematically different results. However, too many particles made tracking difficult and too few particles led to too low statistics. For a given system, the diffusion coefficient was determined from at least 5 films taken at different positions in the gel.

2.2.12.1. CLSM-particle tracking protocol

The particle trajectories were recorded with a Leica TCS-SP2 (Leica Microsystems Heidelberg, Germany). Observations were made with a water immersion objective lens: 20x NA =0.7. An image size of 250 μm and a zoom factor of 2 were used in this work. A He-Ne laser with an emission maximum of 540 nm was used for tracking latex particles. Trajectories of the particles were monitored for different time intervals between images. In all cases 200 8-bit tiff images of 512 \times 512 pixels were recorded and these images were combined together to make a film of the particle displacements.

Figure 2.12 shows a CLSM image of particles with radius, $R=0.25\ \mu\text{m}$ (red) in β -lg gel (green) with protein concentration $C=20\ \text{g/l}$ and salt concentration, $C_s=0.3\ \text{M}$. Particles are situated in the pore phase of the gel.

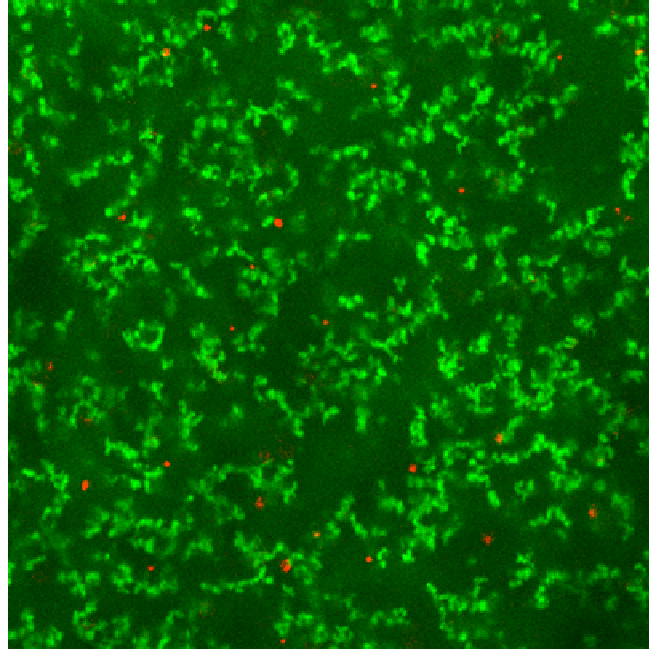


Figure 2.12. Shows the CLSM image of particles with $R=0.25 \mu\text{m}$ (red spots) in β -lg gel (green) with $C=20 \text{ g/l}$ and $C_s= 0.3 \text{ M}$. Scale of the image is $160 \mu\text{m}$.

2.2.12.2. Particle tracking analysis

Here we tracked the particle displacements in the x-y direction with the help of a particle tracking routine, see annex 1, and the mean square displacement in both directions was averaged.

$$\langle r^2 \rangle = (\langle x^2 \rangle + \langle y^2 \rangle)/2 \quad 2.9$$

If the tracers diffuse normally then the MSD of the particles increases linearly with time and the diffusion coefficient of the tracer can be determined by the following equation:

$$\langle r^2 \rangle = 2Dt \quad 2.10$$

If the MSD of the particles increases with time as a weaker power law, then the diffusion of the tracer is anomalous diffusion:

$$\langle r^2 \rangle \propto t^\alpha \quad 2.11$$

with $\alpha < 1$. In this case no diffusion coefficient can be determined.

As an example, the MSD of particles with (radius) $R=0.25\ \mu\text{m}$ in water is shown as a function of time, see figure 2.13. From the graph it is clear that the MSD increases linearly with increasing time. Notice that we have recorded the MSD of the particles only up to forty frames even though the stack contained two hundred images. Films with different Δt 's were analyzed and give the same diffusion coefficient, see figure 2.13.

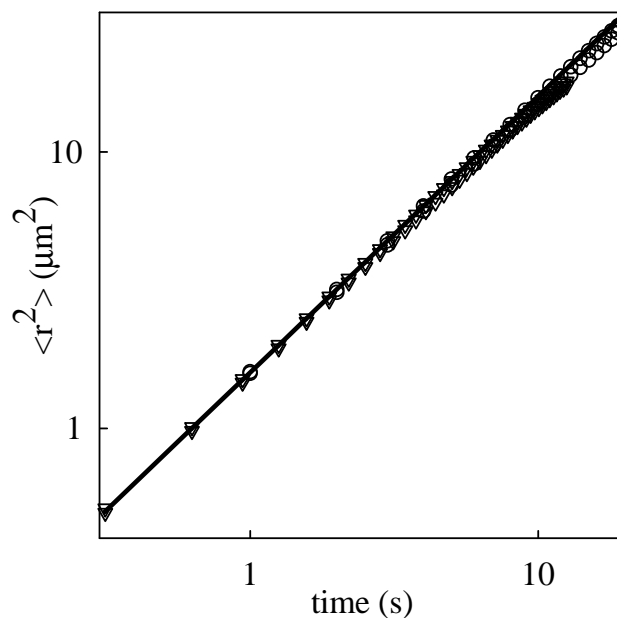


Figure 2.13. Plot of $\langle r^2 \rangle$ versus time for tracers with $R=0.25\ \mu\text{m}$ in water. The solid line represents $\langle r^2 \rangle = 2Dt$

The particle tracking measurements also provide the distribution of mean square displacements $P(r^2)$ of the particles which is Gaussian for normal diffusion and broader for anomalous diffusion. Figure 2.14 Shows the distribution of mean square displacements of $0.2\ \mu\text{m}$ particles at different times (1 (circles), 4 (triangles), and 40 s (squares)) in β -lg gels with $C=20\ \text{g/l}$ and $C_s=0.18\ \text{M}$ salt. The average MSD of particles is smaller at shorter times, but it increases with increasing time if the diffusion is normal.

An important limitation for MPT is that the number of particles that are tracked is rather limited (<100). Hence the experimental error in MPT is larger than for other techniques that can be used to measure particles diffusion such as dynamic light scattering and pulsed field gradient NMR.

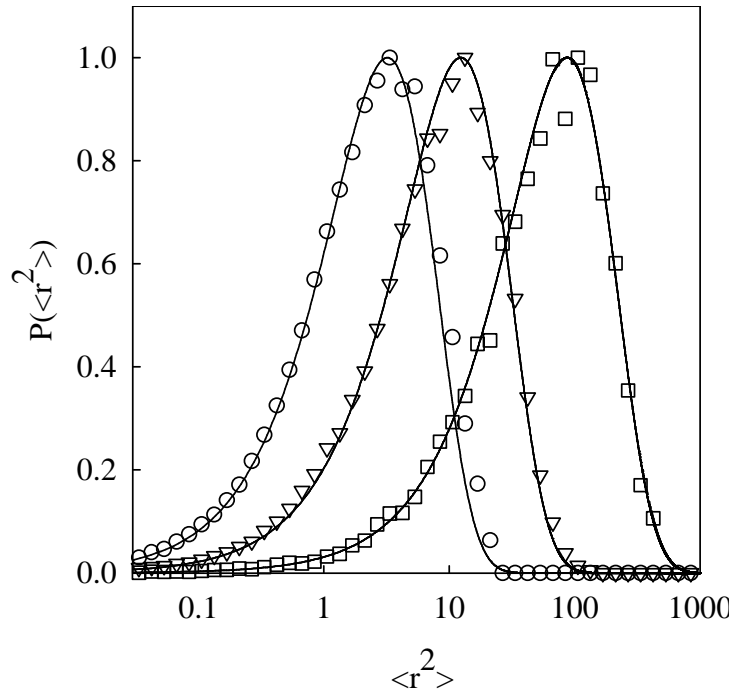


Figure 2.14. The distribution of mean square displacements of $0.2 \mu\text{m}$ particles at different times (1 (circles), 4 (triangles), and 40 s (squares)) in $\beta\text{-lg}$ gels with 20 g/l $\beta\text{-lg}$ and 0.18 M salt

2.2.13. FRAP

As mentioned in chapter.1, in FRAP the intensity recovery of the fluorescein tagged dextran in a region of interest (ROI) is monitored with CLSM after intense bleaching with high intensity laser radiation. The photobleaching reaction of the dye is irreversible and hence the intensity recovery in ROI is related to the diffusion of the tracer molecules. Fluorescein-tagged dextran molecules with different molecular weights were used as tracer particles, for details see materials. A simple FRAP experiment set-up consists of three different stages: pre-bleach, bleach and post bleach. First a ROI was chosen in the sample where the system is bleached. Then 10 images were recorded during pre-bleach and bleach and a varying number of images were recorded during post-bleach. The laser intensity during pre-bleach and post-bleach was chosen small enough so that bleaching could be neglected.

2.2.13.1. CLSM-FRAP protocol

Observations were made with a Leica TCS-SP2 (Leica Microsystems Heidelberg, Germany) with a water immersion objective lens: 20x NA =0.7. An image size of 63x63 μm and a zoom factor of 8 were used. The size of the bleached region was 30x30 μm at the center of the image. A pinhole size of one Airy unit was chosen and the beam expander was set to one. The low numerical aperture of the objective and the large bleached region ensure a cylindrical bleaching geometry. An argon laser with an emission maximum of 488 nm was used in this work. The laser intensity was kept at 2% before and after bleaching while it was 100 % during bleaching. The time interval between the images was kept as small as possible during bleaching: 0.31 s. All the images were stored in 8-bit tiff-images. The image format was 512x512 pixels.

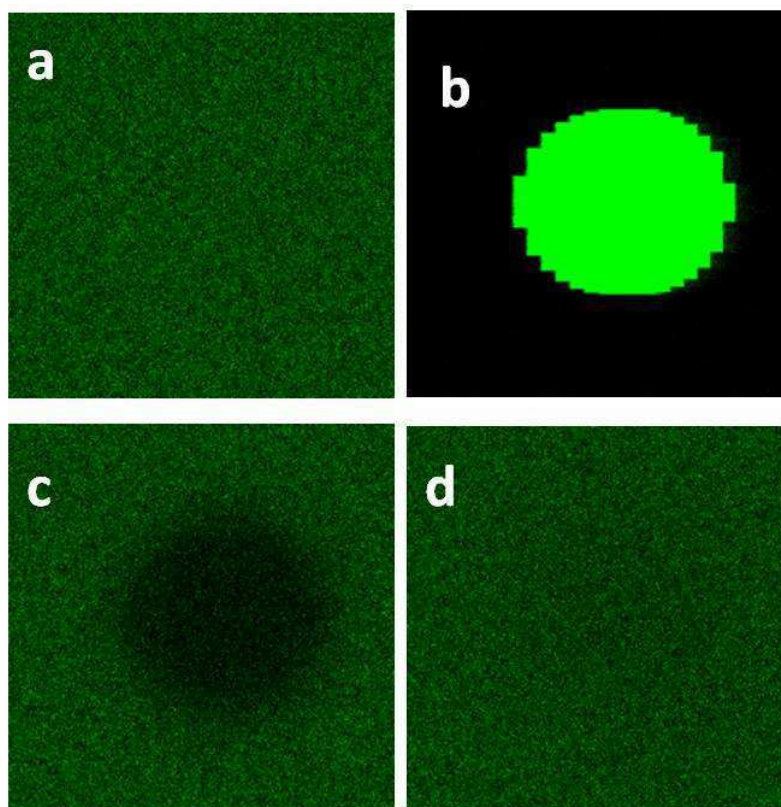


Figure 2.15. Example of a FRAP experiment in β -lg gels. a to c show the first pre-bleach, bleach and post-bleach images, respectively, and d shows the system 50 s after the bleach. Scale of the image is 63 μm .

Figure 2.15 visualizes different stages of a FRAP experiment set up in β -lg gels with $C=40$ g/l and $C_s=0.1$ M for d2000k probe. Images a to c correspond to the first pre-bleach, bleach and post-bleach images, respectively while d was taken after 50 s.

The intensity recovery of d2000k inside the bleached region is shown in figure 2.16.

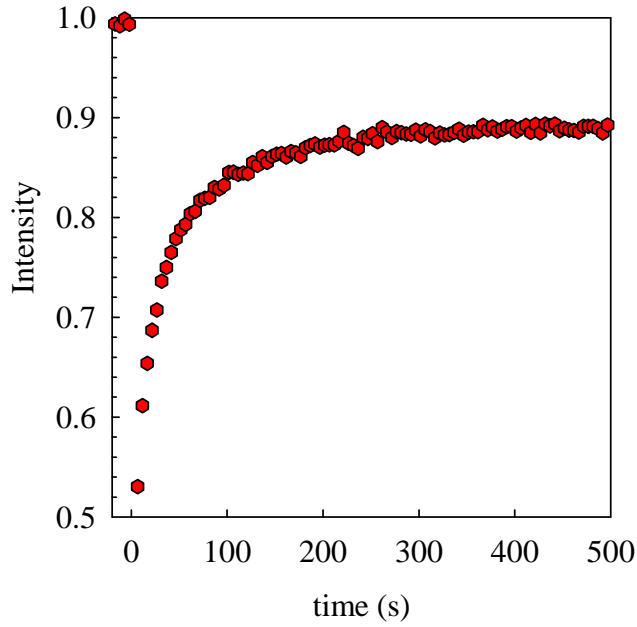


Figure 2.16. Recovery of the intensity after bleaching as a function of time for d2000k in a β -lg gel with $C=40$ g/l and $C_s=0.1$ M.

2.2.13.2 FRAP data analysis

The data analysis was carried out in Mat-lab using a novel method explained in annex 2. The diffusion coefficient of the tracers can be calculated if the intensity recovery of the probes is Gaussian. This is the case, if the diffusion of the tracers is Brownian. It was found that this was true in all cases for the smallest tracers (d40k). The intensity recovery data of the larger dextran molecules (d500k and d2000k) in the gel was not Gaussian for the first few post-bleach images, irrespective of the salt and protein concentrations. Hence the first two post-bleach images with larger tracers were excluded from the analysis.

As an example, the fluorescence intensity of d2000k is shown in figure 2.17 as a function of the distance from the center of the bleached region 40 s. after bleaching for β -lg gels formed at $C=60$ g/l and two different salt concentrations: $C_s=0.05$ and 0.1 M. At $C_s=0.1$ M the recovery of d2000k was Gaussian while at $C_s=0.05$ M it was non Gaussian.

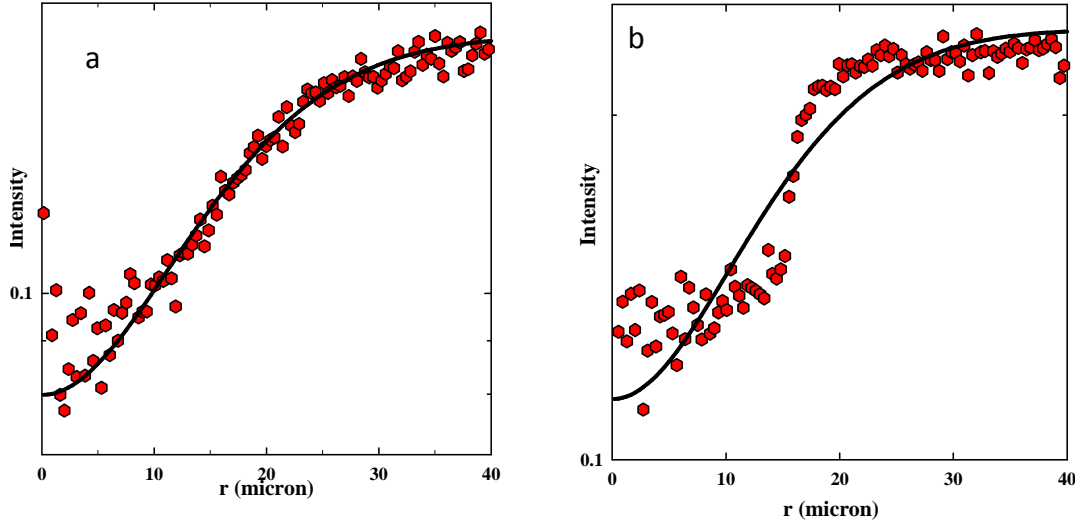


Figure 2.17. Intensity of unbleached d2000k probes as a function of distance from the center of the bleached region 40 seconds after bleaching in β -lg gels at $C=60$ g/l for $C_s=0.1$ M (a) and 0.05 M (b). The solid lines represent fits to a Gaussian profile.

From figure 2.17 it is clear that for a Gaussian intensity recovery profile, a good fit to the data was obtained and the calculated diffusion coefficient of the tracers is reliable. On the other hand for a non Gaussian intensity recovery profile, a poor fit to the data was obtained and the calculated value of D is not trustworthy.

2.3. Interfacial tension measurements by drop relaxation

The most suitable method to measure the interfacial tension of incompatible aqueous biopolymer solutions is to measure the relaxation of elongated droplets of one solution surrounded in a matrix of the other solution. The advantage of drop relaxation methods is that it allows one to measure extremely low values of the interfacial tension

which would be very difficult to obtain from more conventional techniques based on the balance between gravitational forces and surface tension.

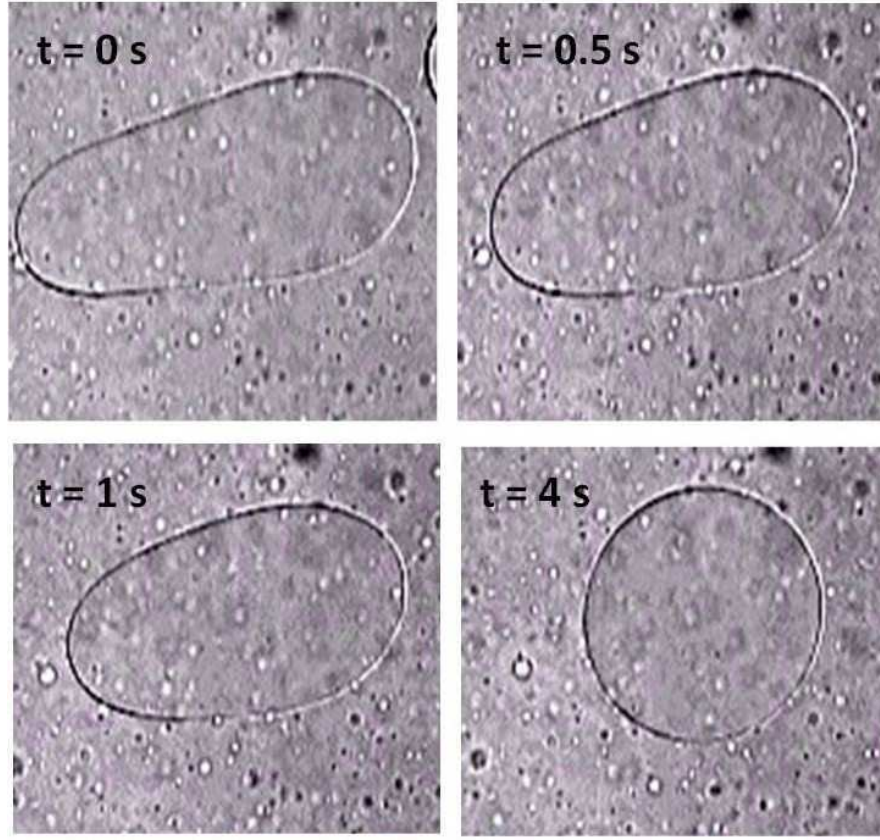


Figure 2.18. Relaxation of a drop of the dextran rich phase in the continuous medium of the PEO rich phase after shear flow.

A droplet of phase A is introduced into the matrix of phase B that fills a specially designed shear cell (Linkam) (Guido, Simeone, & Alfani, 2002) and the whole system is subjected to shear. After stopping the shear the length of the droplets (L) is measured as a function of time until they attain the equilibrium spherical shape. For small deformations, the relaxation of the droplet shape is given by,

$$\ln L = \ln L_0 - \frac{t}{\tau} \quad 2.12$$

where L is the length of the stretched droplet at time t and L_0 is the equilibrium droplet diameter. τ is a characteristic time that depends on the interfacial tension, the viscosity of both phases and the drop radius (Guido et al., 2002):

$$\tau = \frac{\tau_{ca} 19(k+16)(2k+3)}{40(k+1)} \quad 2.13$$

where τ_{ca} is the capillary time and k is the ratio of the droplet (η_d) and matrix (η_m) viscosities. The capillary time is given by,

$$\tau_{ca} = \frac{\eta_m R_0}{\gamma_{AB}} \quad 2.14$$

where γ_{AB} is the interfacial tension and R_0 is the equilibrium radius of the droplet. Figure 2.18 shows a sequence of images of a dextran droplet during relaxation in the PEO rich phase at different times. The plot of $\ln(L/L_0)$ of droplets as a function of time is shown in figure 2.19. The droplets take a relatively long time (a few seconds) to recover their equilibrium diameter due to the low value of the interfacial tension and the relatively high viscosity of the medium. From the plot of $\ln(L/L_0)$ vs time, the interfacial tensions of the mixtures could be measured accurately.

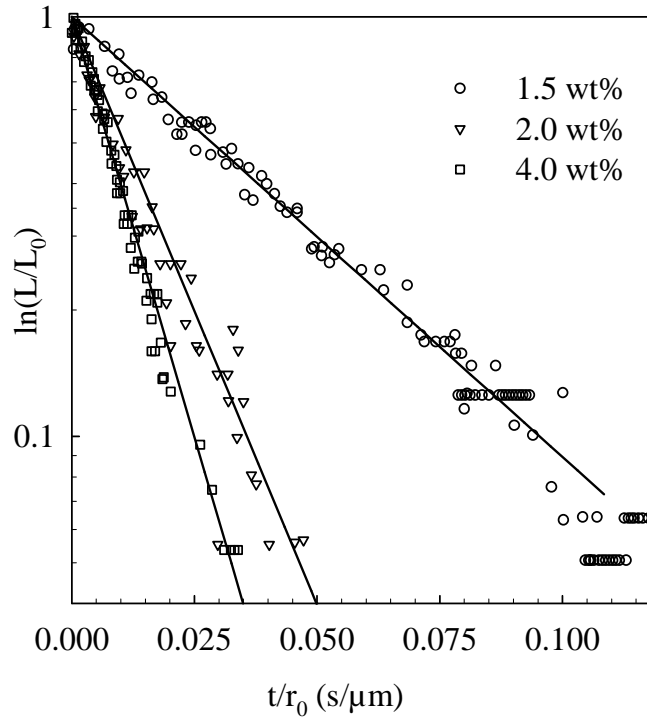


Figure 2.19 .Droplet deformation parameter as a function of time in mixtures of 20 g/L dextran and varying concentrations of PEO indicated in the figure.

2.4. Light scattering

Standard dynamic light scattering (DLS) measurements were used to measure the intensity autocorrelation function ($G_2(t)$) at different scattering angles (θ). The intensity autocorrelation function at a given scattering vector ($q = 4 \frac{\pi}{\lambda} \sin \frac{\theta}{2}$) is given by

$$G_2(t) = I(t) \cdot I(t + \Delta t) \quad 2.15$$

where I is the intensity of the scattered light. For $\Delta t = 0$, $G_2(0)$ is maximum and is equal to the mean square intensity $\langle I(t)^2 \rangle$. For $\Delta t \rightarrow \infty$ the intensities of the scattered light at t and $t + \Delta t$ are uncorrelated and $G_2(\infty)$ becomes equal to the square of the average intensity $\langle I(t) \rangle^2$. Figure 2.20 shows an example of the intensity correlation function.

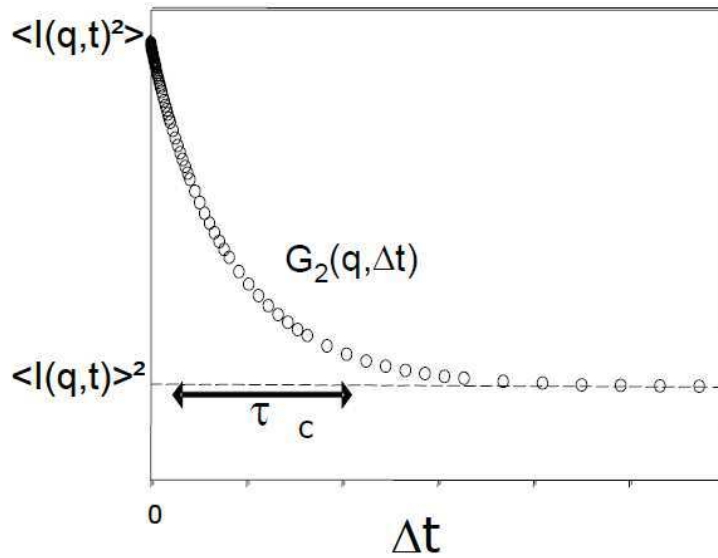


Figure 2.20. Evolution of $G_2(t)$ as function of time (Δt)

$G_2(t)$ is related to correlation function of the electric field amplitude fluctuations ($G_1(t)$) by the Siegert relation (Berne & Pecora, 1976). The normalized autocorrelation function of the scattered electric field fluctuations is analyzed in terms of a distribution of relaxation times using the Laplace inversion routine REPES (Stepanek, 1993).

$$g_1(q, t) = \int A_\tau \exp\left(-\frac{t}{\tau}\right) d\tau \quad 2.16$$

The relaxation time distribution ($A(\tau)$) gives information about the dynamics of the particles on the length scale q^{-1} . The average diffusion coefficient of the particles can be determined from the average relaxation time by using the relation

$$\tau = \frac{1}{D_0 q^2} \quad 2.17$$

The average hydrodynamic radius of the particles can be determined from the diffusion coefficient using the Stokes-Einstein relation:

$$D = kT/6\pi\eta R_h \quad 2.18$$

Where k is Boltzmann's constant, T is temperature in Kelvin, η is the medium viscosity and R_h is the hydrodynamic radius of the diffusing particle.

2.5. Size exclusion chromatography

Size exclusion chromatography (SEC) measurements were done at room temperature with a TSK PW 5000 + PW 6000 column set (30 cm + 60 cm) in series in addition to a Zorbax GF-450 pre-column (25 cm). The refractive index was measured at the exit of the columns using a differential refractive index detector (SHODEX RI 71). A volume of 300 μ l of the protein solution was injected using an automatic injection system (Auto injector 234, Gilson) at a concentration of approximately 1 g.L⁻¹. The system was eluted at 20°C with 0.1 M NaNO₃ at pH 7 with a flow rate of 1 ml.min⁻¹. The elution volume was converted to the molar mass using calibration curves obtained with dextran and PEO standards.

2.6. Viscosity

The viscosity (η) of the solutions was determined from shear flow measurements at 20°C using a stress-controlled rheometer (ARG2, Rheometrics) with a cone-plate geometry (60 mm diameter, cone angle 0°58') The viscosities of pure PEO and dextran solutions in the linear response regime are shown as a function of the polymer concentration in figure 2.21. η increased more strongly with increasing concentration for PEO than for dextran.

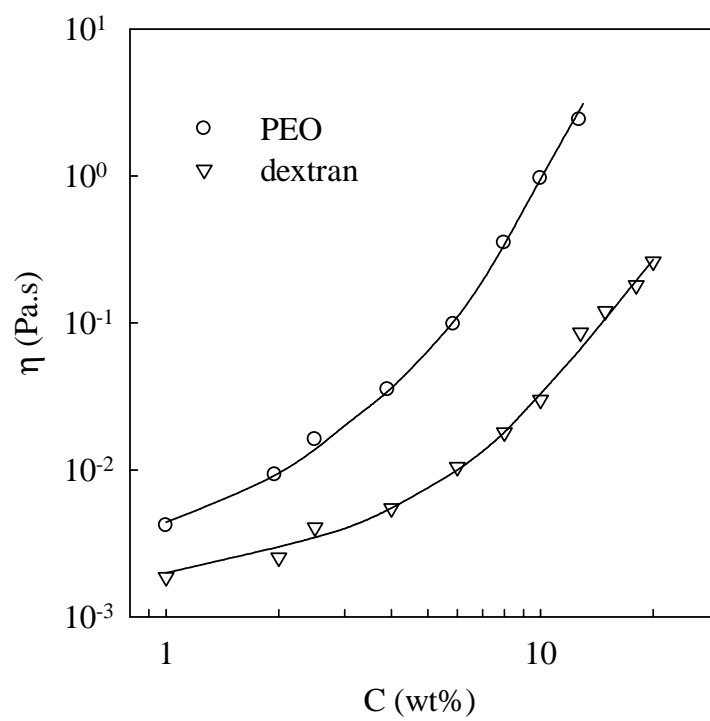


Figure 2.21. Concentration dependence of the viscosity of pure aqueous dextran and PEO solutions.

Results and Discussion

3. Results and discussion

3.1. Particle diffusion in β -lg gels

3.1.1. Introduction

Here we explore the diffusion of model colloidal particles/molecules in well-characterized heat-set gels of β -lg. Our aim is to correlate the structure of gels formed at different ionic strengths with the mobility of particles/molecules embedded in the gel. As mentioned in chapter .1, there exist various techniques like pulsed field gradient NMR and dynamic light scattering to measure the diffusion properties (N. Lorén et al., 2009). In this study we used two simple but powerful techniques to measure the diffusion of tracers in β -lg gels: multiple particle tracking (MPT) and fluorescence recovery after photo bleaching (FRAP). MPT requires larger tracers with diameters of the order of a micrometer while FRAP can be used with small tracers such as molecules or polymer chains. At pH 7, the visual aspect of the gel varies from transparent to turbid in a narrow range of salt concentrations (Ako, Durand et al., 2009; Durand et al., 2002; Mehalebi et al., 2008), see chapter.1. The transparent gels are homogeneous on the length scale accessible to light microscopy whereas very turbid gels are heterogeneous. We have used MPT to study the diffusion of tracer particles in heterogeneous gels. The structure of these gels was characterized by detailed analysis of CLSM images. Fluorescent polystyrene latex particles with radii between 0.1 and 1 μm were used as the tracer particles. However, MPT cannot be used with homogeneous gels, because the size of the tracers is larger than the pore size of the gel and hence the tracer particles are trapped in the gel matrix. On the other hand, FRAP could be used to study the diffusion in homogeneous gels with smaller tracers. For FRAP, we have used fluorescein isothiocyanate labeled dextran molecules (FITC-dextran) with different molecular weights ($M_w=4.0\times 10^4$, 5.0×10^5 and 2.0×10^6 g/mol, denoted d40k, d500k and d2000k, respectively). We will attempt to relate the diffusion of tracers in these gels to their structure.

3.1.2. Diffusion in liquids

In first instance, we have studied the diffusion of tracer particles in unheated β -lg solutions using particle tracking and FRAP. No systematic dependence on the salt

concentration was observed. Figure 3.1 shows the diffusion coefficient (D) normalized by the value in water (D_0) for tracers with different radii as a function of the protein concentrations obtained from particle tracking (b) and FRAP (a). Each D/D_0 is an average of at least 5 measurements correspond to different positions of the same sample. As expected, D/D_0 decreased with increasing protein concentration. The protein solution can be considered as a continuous medium with viscosity η for the larger latex particles used in MPT. Therefore the variation of D/D_0 is equal to the variation of η_0/η of the protein solution, see Eqn 2.18. η_0/η of the protein solutions was determined and included in figure 3.1. Also we calculated D/D_0 of particles with $R=0.25\ \mu\text{m}$ in protein solutions with dynamic light scattering (DLS). It was found that D/D_0 obtained by MPT and by DLS are the same within the experimental error.

FITC-dextran molecules are comparatively smaller and at lower protein concentrations, the solution cannot be considered as a continuous medium. This is clearly seen in Figure 3.1 (a), at lower protein concentrations for which D/D_0 is systematically higher than η_0/η of the protein solutions. At higher concentrations, the protein solutions may again be considered as a continuous medium for the tracers as D/D_0 is close to η_0/η .

3.1.3. Diffusion in gels

Gels were prepared by heating β -Ig solutions at 80°C until the reaction was complete. Gels with a wide range of porosity were formed by varying the protein and the NaCl concentration. The diffusion of tracer particles in heterogeneous gels was investigated by MPT and the diffusion in homogeneous gels was investigated by FRAP.

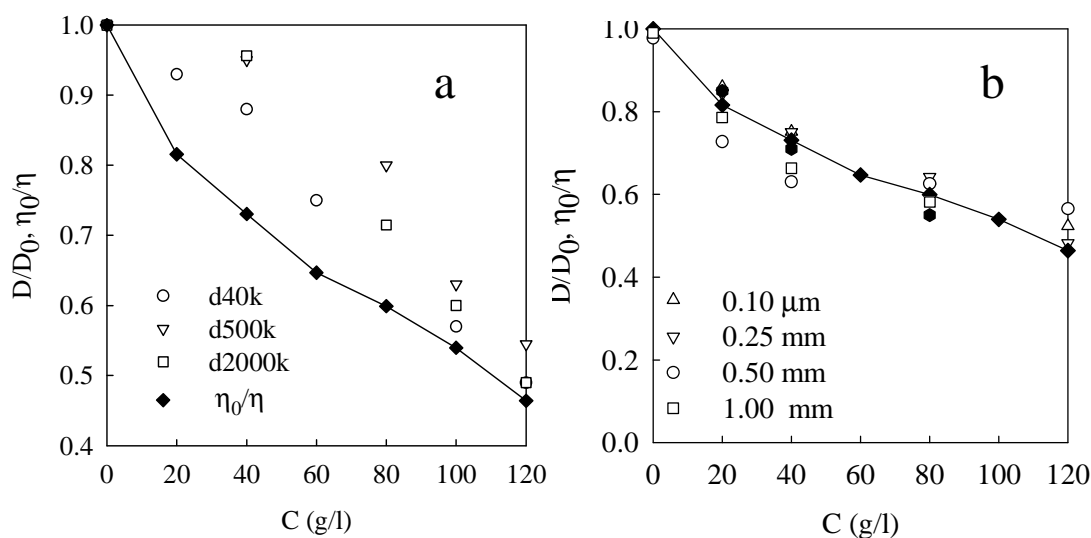


Figure 3.1. (a) D/D_0 obtained from FRAP for tracers with different molecular weights as a function of the protein concentration. η_0/η of the protein solutions (closed diamond) is included. (b) D/D_0 obtained from particle tracking for tracers with different radii as indicated in the graph as a function of the protein concentration. D/D_0 obtained by DLS for tracers with $R=0.25 \mu\text{m}$ (closed hexagons) and η_0/η (closed diamonds) are also shown.

3.1.3.1. Structure of the gels.

As mentioned in the first chapter, at lower ionic strength and pH far from the isoelectric point, the gel is transparent and the structure is homogeneous on the length scale of microscopy. Scattering methods were extensively used to characterize these gels. It was observed that there was a peak in the static structure factor for the gels formed at lower salt concentrations and pH 7 at $C=100$ g/l (Ako, Nicolai et al., 2009; T. Nicolai, Pouzot, Durand, Weijers, & Visschers, 2006; Pouzot et al., 2004). This interaction peak indicates a weak ordering of the aggregated proteins, which decreases with increasing salt concentration and decreasing protein concentration. Figure 3.2 shows the SAXS results of gels formed at different ionic strengths for $C=100$ g/l. Above, around 20 mM salt, the scattering peak is no longer observed and the intensity at small q -values increases, see figure 3.2.

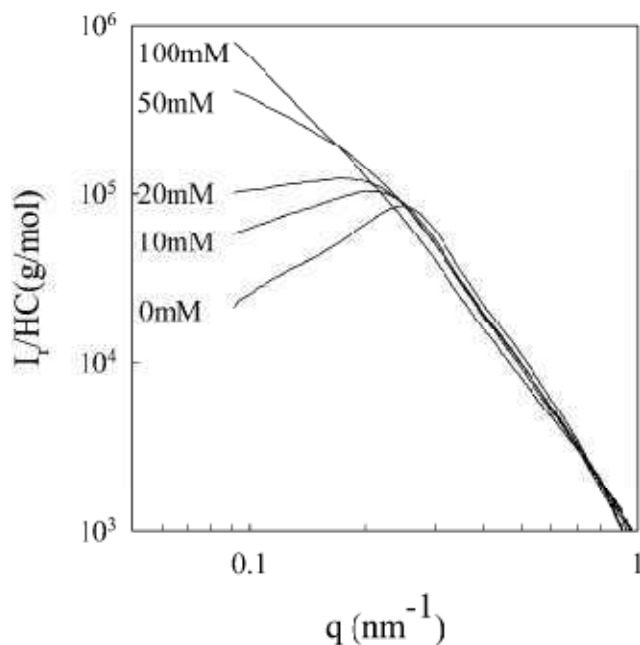


Figure 3.2. Dependence of the scattering intensity on the scattering wave vector (q) for β -lg gels ($C = 100$ g/L) prepared at different NaCl concentrations (T. Nicolai et al., 2006; Pouzot et al., 2004).

The disappearance of the peak indicates that the local ordering of the aggregates becomes weaker. It was found that the visual aspect of the gels varied from transparent at $C_s \leq 0.05$ M to opaque at $C_s \geq 0.2$ M (Ako, Durand et al., 2009; Mehalebi et al., 2008; T. Nicolai et al., 2006; Pouzot et al., 2004). The increase of the turbidity could be understood in terms of increasing heterogeneity, i.e. the increase of the correlation length, with increasing salt. Ako et al (Ako, Durand et al., 2009) investigated in detail the effect of the salt concentration on the correlation length of the gels at pH=7 and $C=100$ g/l, see figure 3.3. The correlation length increased strongly between $C_s=0.1$ and 0.2 M followed by a weak increase at higher ionic strengths. The correlation length was found to be less than 20 nm for $C_s \leq 0.05$ M (Pouzot et al., 2004).

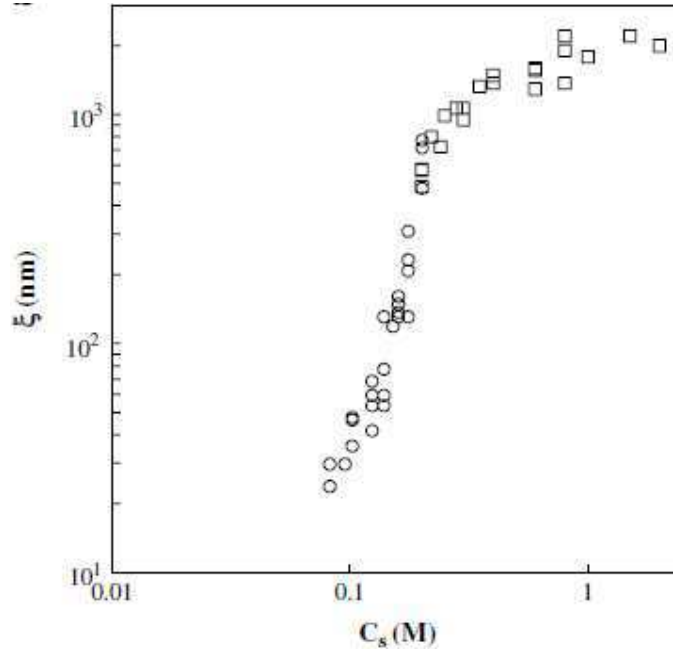


Figure 3.3. Dependence of the correlation length on the salt concentration for β -lg gels at pH 7 and $C=100$ g/l (Ako, Durand et al., 2009).

It was found that when the salt concentration is above than a critical limit, then β -lg aggregates form dense particles with a radius of about a micrometer. Ako et al (Ako, Nicolai et al., 2009) reported that microphase separation induces the formation of these dense particles. These particles can stick together to form a phase spanning gel at higher protein concentrations or precipitate at lower protein concentrations. It is not easy to pinpoint exactly the critical salt concentration for microphase separation, but gels with salt concentration $C_s \leq 0.15$ may be considered as homogeneous (not microphase separated).

Heterogeneous gels were formed at varying protein ($C=20$ - 120 g/L) and NaCl ($C_s=0.1$ - 0.25 M) concentrations. This range of ionic strengths was chosen here because for $C_s \geq 0.25$ M NaCl, Brownian diffusion was observed for all tracers used in MPT, while for $C_s \leq 0.1$ M, all tracers were trapped. Figure 3.4 shows CLSM images of the gel structure at different protein and salt concentrations. At $C_s=0.25$ M, the gel structure was heterogeneous and similar for all protein concentrations. At $C_s=0.20$ M, the gel structures are similar for all protein concentrations except for $C=20$ g/l which appeared more homogeneous. At $C_s=0.18$ M, a transition of structure occurred between $C=40$ and 80 g/l.

For $C \leq 40$ g/l, the gel structures were similar to those found at $C_s=0.15$ M while for $C \geq 40$ g/l; the structures are similar to those at 0.2 M salt. At $C_s=0.1$ M the CLSM images were homogeneous at all protein concentrations (results not shown).

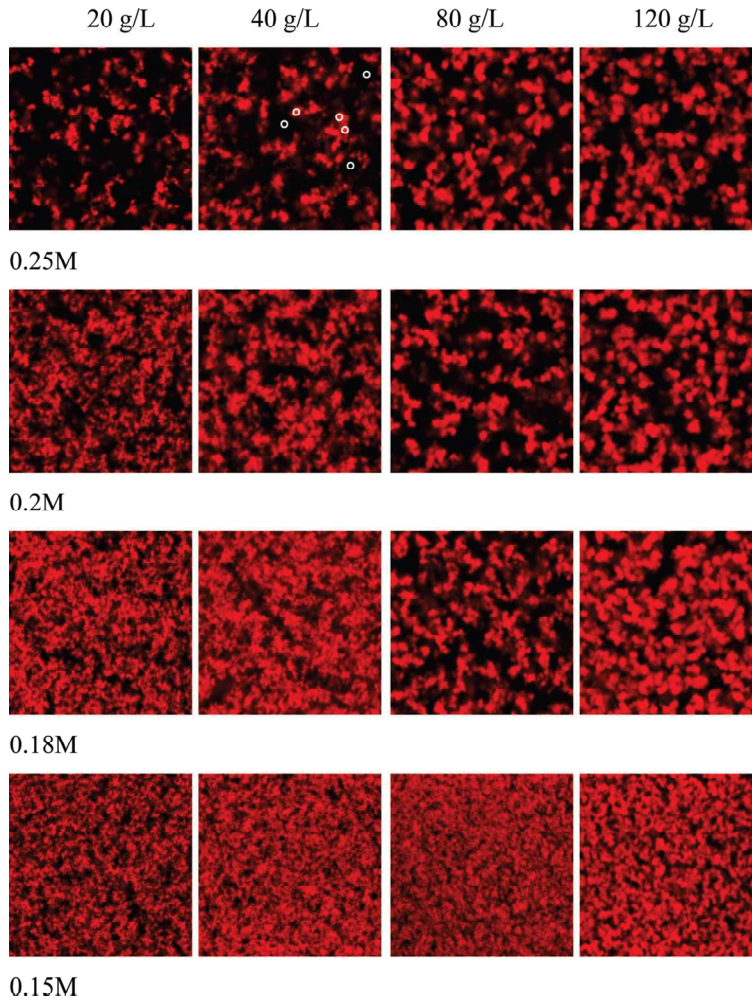


Figure 3.4. CLSM images of β -lg gels at different protein and salt concentrations. The images represent $40 \times 40 \mu\text{m}$. The circles in the image at 0.25 M and 40 g/L illustrate areas over which the intensity was measured in the gel phase and the pores

Increase in structural heterogeneity at higher protein concentrations for salt concentrations $C_s=0.18$ M and to a minor extent at 0.2 M could be explained by taking into account the counter ion concentration that increases with increasing protein concentration. At pH 7, the net charge of β -lg is -7 resulting in around 0.4mM counter ions per gram per liter of β -lg. Precise quantification of the amount of free counter ions is

not possible since the proteins are ambivalent and counter ion condensation may occur. Nevertheless, the fraction of counter ions is clearly not negligible and this can cause structural changes near the critical salt concentration.

The CLSM images were analyzed in terms of the pair correlation function $g(r)$ of the protein concentration fluctuations as explained in chapter 2. Figure 3.5 shows the decay of $g(r)$ for different protein concentrations at $C_s=0.18$ M. The amplitude of $g(r)$ indicates the contrast which is lower at lower protein concentrations when $C \leq 40$ g/l, but it is higher at $C=80$ g/l than $C=120$ g/l.

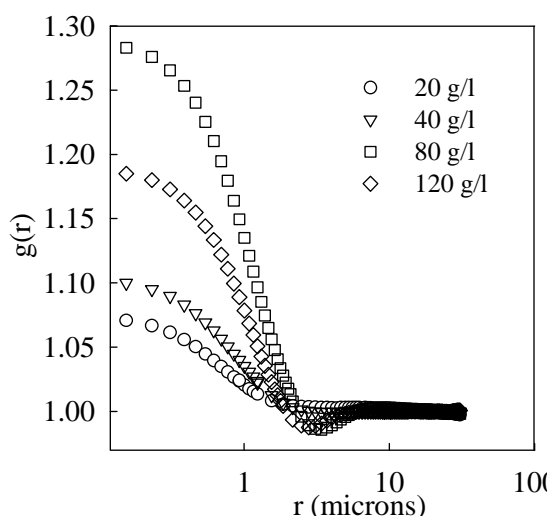


Figure 3.5. Semi-logarithmic representation of $g(r)$ for different protein concentrations at $C_s=0.18$ M salt.

Figure 3.6, was obtained by normalizing the pair correlation function at $r=0.15$ μm for different protein and salt concentrations. At 0.25 M and 0.15 M NaCl, the pair correlation functions for different protein concentrations are similar and there is no significant influence of the protein concentration on $g(r)$. At $C_s=0.2$ M and at all protein concentrations, $g(r)$ is similar to that at 0.25 M except at $C=20$ g/l for which it was intermediate between the results at $C_s=0.25$ M and at $C_s=0.15$ M. At $C_s=0.18$ M, $g(r)$ at $C=80$ g/l and $C=120$ g/l was similar to that at $C_s=0.25$ M while at $C=20$ g/l and $C=40$ g/l $g(r)$ was intermediate between that at $C_s=0.15$ M and $C_s=0.25$ M. Heterogeneous gels at

higher protein concentrations showed a weak minimum of $g(r)$ which indicates a preferred distances between the strands of the gels.

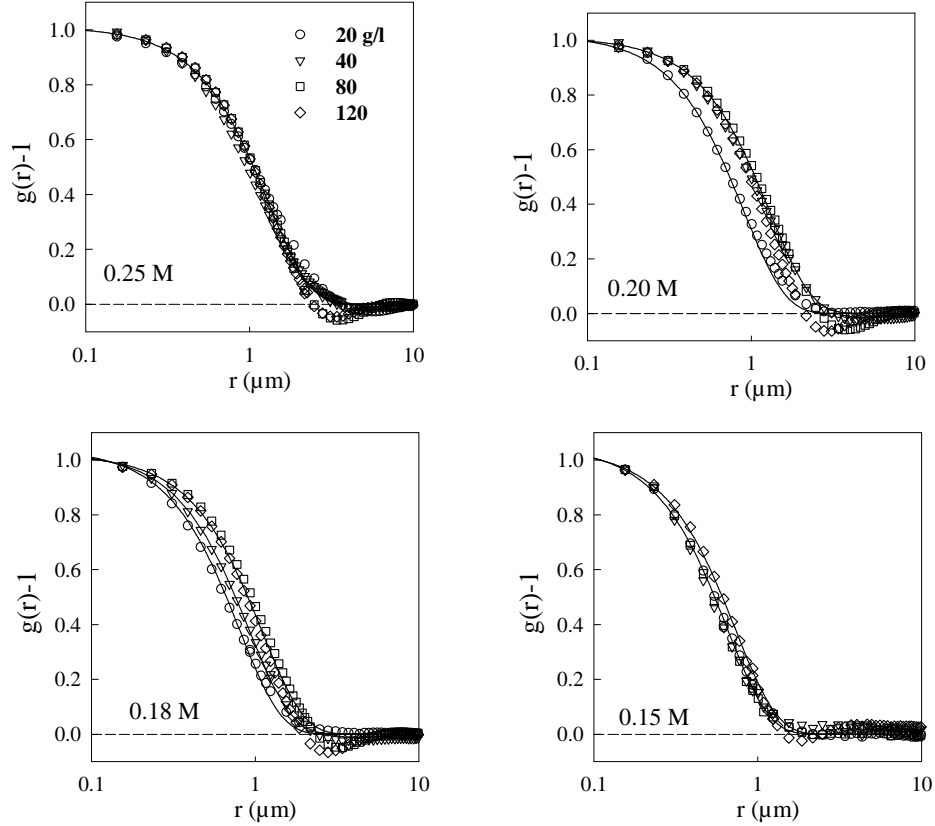


Figure 3.6. Semi-logarithmic representation of the normalized pair correlation functions of heat-set β -lg gels formed at different β -lg and NaCl concentrations indicated in the figures. The solid lines represent fits to $g(r) - 1 = \exp[-(r/\xi)^\beta]$.

The decay of $g(r)$ was described by a stretched exponential decay, $g(r) - 1 = B_1[-(r/\xi)^\beta]$ as explained in chapter 2. The correlation length, ξ , of the systems could be compared by keeping the value of β fixed at 1.75. However, changing the value of β by 10 % higher or lower still yielded a good fit to the data. There was little dependence of correlation length on the protein concentration at 0.25 and 0.15 M NaCl, but the correlation length at $C_s=0.25$ M was around two times larger than at $C_s=0.15$ M. Table 3.1 shows the correlation lengths of the gels at different salt and protein concentrations. A

weak decrease of the correlation length was observed with increasing protein concentration at 0.18 and 0.20 M NaCl. This increase can be attributed to an increase in the counter ion concentration as was explained above.

Concentration	0.25 M	0.2 M	0.18 M	0.15 M
120 g/L	1.3	1.1	1.1	0.73
80 g/L	1.3	1.1	1.1	0.65
40 g/L	1.3	1.1	0.9	0.65
20 g/L	1.3	0.9	0.8	0.65

Table 3.1. β -lg gel correlation lengths (μm) for different β -lg and NaCl concentrations.

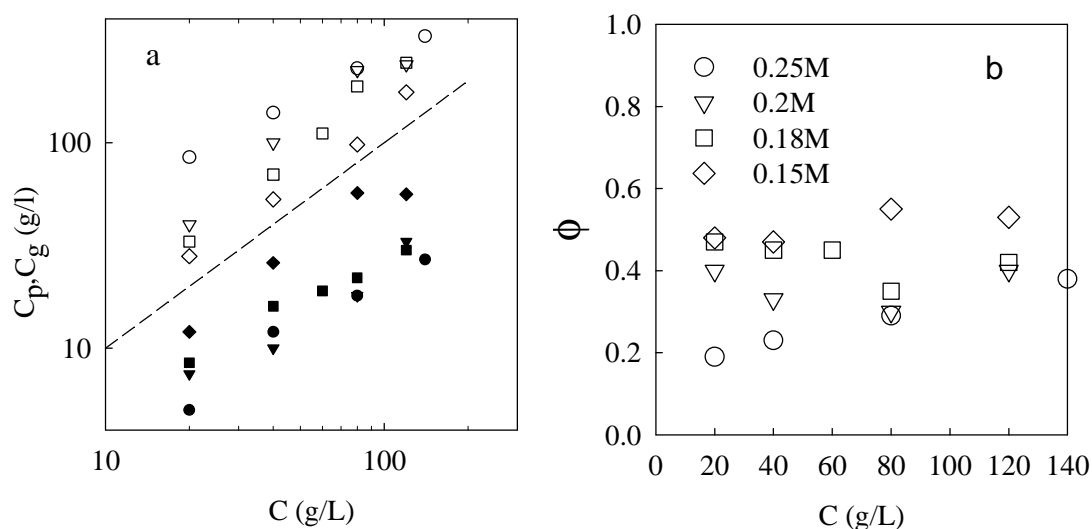


Figure 3.7. (a) Protein concentration in the gel (C_g) (open symbols) and the pores (C_p) (closed symbols) as a function of the average protein concentration for gels formed at different NaCl concentrations. The dashed line in figure a represents $C_p = C_g = C$. (b) Volume fraction of the gel as a function of the average protein concentration for gels formed at different NaCl concentrations.

It is possible to determine the protein concentration in the gel phase (C_g) and in the pore phase (C_p) by measuring the intensity of each phase as explained in chapter 2.

Figure 3.7 (a) shows a plot of C_p and C_g versus the protein concentration at different salt concentrations. From the graph, it is clear that both C_p and C_g increase linearly with increasing protein concentration for a given salt concentration. The contrast between the gel phase and the pore phase decreases with decreasing salt concentration and at lower salt concentrations the gels are less heterogeneous. The volume fraction of the gel see figure 3.7 (b), (ϕ) was determined from C_p and C_g by using the relation, $C = C_g\phi + (1-\phi)C_p$. For given protein concentration, the volume fraction of the gel is higher for more heterogeneous gels. The gel volume fraction at a given salt concentration is not a strong function of the protein concentration since both C_p and C_g increase linearly with C .

3.1.3.2. Tracer diffusion in gels using MPT

Fluorescent latex particles with different radii (0.1-1 μm) were used as tracers. At $C_s=0.25$ M all tracers diffused normally for all protein concentrations tested between 20 and 120 g/L indicating that the proteins present in the pores did not form gels and are probably in the form of small aggregates. At $C_s=0.2$ M particles with $R=1$ μm were trapped in the matrix for all C and the MSD of these tracers remained less than 10^{-2} μm^2 , while the other tracers were diffusing normally. At $C_s=0.18$ M particles with $R=0.25$ and $R=0.1$ μm diffused normally for $C \geq 80$ g/l, but at lower C (20 and 40 g/l) only particles with $R=0.1$ μm diffused normally. At $C_s=0.15$ M only particles with $R=0.1$ μm diffused normally for $C \geq 80$ g/l while at lower protein concentrations none of the tracers showed Brownian diffusion. Finally at 0.1 M NaCl, all the tracers were trapped for all protein concentrations.

D/D_0 of the tracers is plotted as a function of the protein concentration in figure 3.8 for tracers with different radii and at different salt concentrations. It was found that the scattering of D/D_0 in the gels is larger than in the liquids. The D values varied somewhat for different gels prepared at the same conditions. This is probably due to a variation of the gel structure, caused by small differences in the heating history during the preparation of the gels. There was no systematic dependence of D/D_0 on the protein concentration. This is expected because the gel volume fraction was not strongly correlated with the protein concentration, see figure 3.7 (b). Figure 3.8 was obtained by plotting D/D_0 as a function of the protein concentrations (a) and the corresponding gel

volume fractions (b) for different salt concentrations and tracer radii. Interestingly, there was no clear systematic dependence of tracer size on D/D_0 , contrary to expectation. However, we cannot exclude a small effect that is hidden by the large scatter in the data.

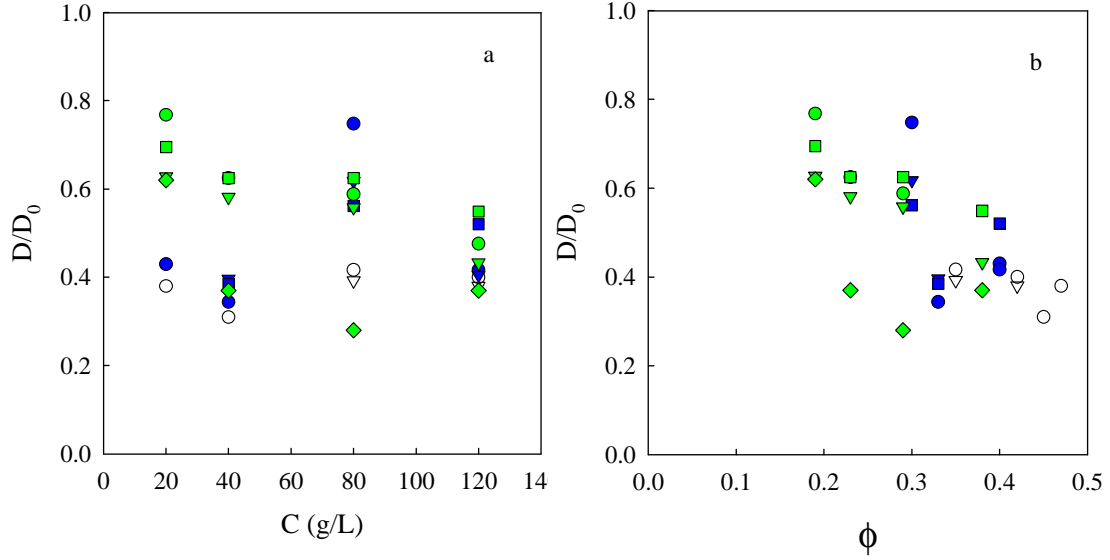


Figure 3.8. Dependence of D/D_0 on the protein concentration (a) or the gel volume fraction (b) for tracers with different radii ($0.1 \mu\text{m}$ (circles), $0.25 \mu\text{m}$ (triangles), $0.5 \mu\text{m}$ (squares), $1.0 \mu\text{m}$ (diamonds)) in gels formed at different ionic strengths (0.18M (white), 0.2M (blue), 0.25M (green)).

In some cases we observed anomalous diffusion of the tracers when MSD increased as $\langle r^2 \rangle \propto t^\alpha$ with $\alpha < 1$. In these situations the distribution of the displacements was broader than the Gaussian distribution expected for Brownian diffusion. As an example we show in figure 3.9 (a) the MSD of different size tracers in gels formed at $C = 20\text{g/L}$ and $C_s = 0.18\text{M}$.

In figure 3.10 we have plotted the distribution of the squared displacements $P(r^2)$ for $R = 0.1 \mu\text{m}$ and $0.5 \mu\text{m}$. Tracers with $R = 0.1 \mu\text{m}$ diffused normally and the distribution of the displacements was Gaussian, see figure 3.10 (a). Tracers with $R = 0.25$ and $0.5 \mu\text{m}$

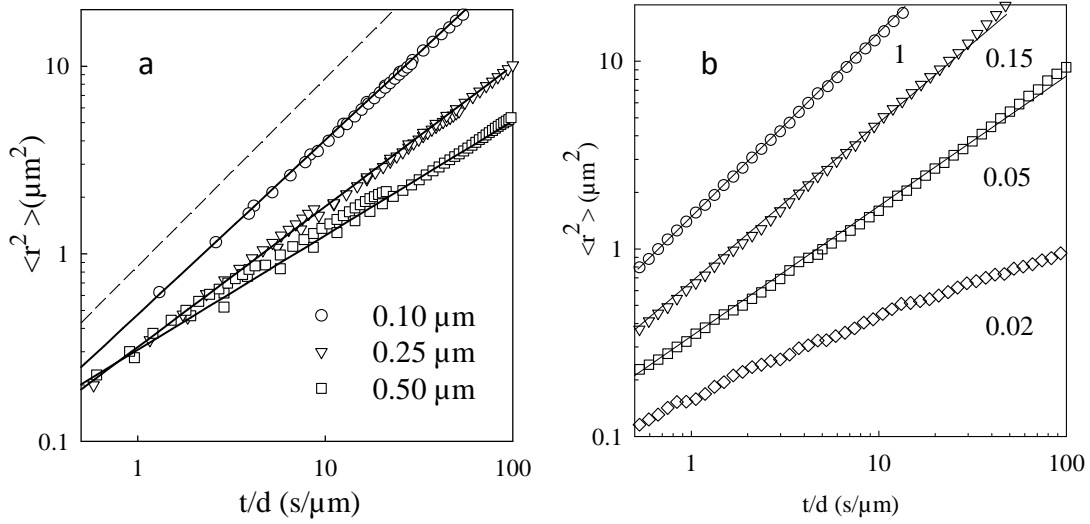


Figure 3.9. (a) MSD as a function of time normalized by the tracer diameter ‘d’ for tracers with different radii indicated in the figure in β -gels at $C = 20\text{g/L}$ and 0.18 M NaCl . The dashed line shows the MSD of freely diffusing tracers. The solid lines have slopes 0.93, 0.75 and 0.61 for $R = 0.1, 0.25$ and $0.50 \mu\text{m}$, respectively. (b) Simulated MSD as a function of time normalized by d for spherical tracers in DLCA gels at different values of the accessible volume indicated in the figure.

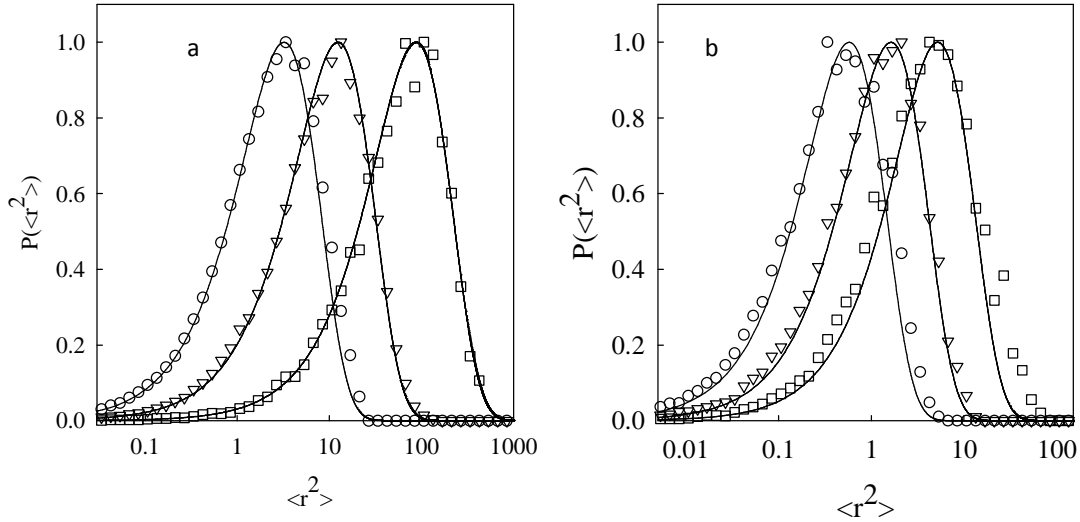


Figure 3.10. Distribution of the squared displacements in β -gels at $C=20\text{g/L}$ and 0.18 M NaCl for tracers with $R=0.1 \mu\text{m}$ (a) and $R=0.5 \mu\text{m}$ (b) at different times (1s (circles), 4s (triangles) and 40s (squares)). The solid lines are fits to a Gaussian distribution of the displacement.

diffused anomalously and $P(r^2)$ was broader, see figure 3.10 (b). In these gels, tracers with $R = 1\mu\text{m}$ were trapped and $\langle r^2 \rangle$ remained smaller than $10^{-2} \mu\text{m}^2$. Anomalous diffusion was observed in situations where the particles were close to being trapped. For instance tracers with $R = 0.5 \mu\text{m}$ showed anomalous diffusion in gels at $C = 20\text{g/L}$ and $C_s=0.2\text{M}$ while tracers with $R= 1\mu\text{m}$ were trapped and tracers with $R= 0.1 \mu\text{m}$ diffused normally.

3.1.3.3. Tracer diffusion in gels using FRAP

FITC-labeled dextran chains with different molecular weights (40, 500 and 2000 kDa) and hydrodynamic radii (R_h) (5.5, 23, and 50 nm) were used as tracers. Contrary to the latex particles used for MPT the dextran chains are polydisperse, see chapter 2. We note that at lower NaCl concentrations the range of protein concentrations where gels are formed is more limited, because the critical gelation concentration increases with decreasing NaCl concentration, see chapter 1.

At $C_s = 0.1 \text{ M}$, the intensity recovery profile of all tracers was Gaussian for all C except for d2000k at $C \geq 80 \text{ g/l}$. A Gaussian profile indicates Brownian diffusion of the tracers and the diffusion coefficient could be calculated. For $C \geq 80 \text{ g/l}$, the intensity profile of d2000k was not Gaussian and the calculation of the diffusion coefficient was not possible, for details, see chapter2.

Figure 3.11 (a) shows D/D_0 of different tracers as a function of C at $C_s = 0.1 \text{ M}$ salt. D/D_0 decreased with increasing protein concentration and tracer size. At $C_s=0.05 \text{ M}$, the intensity profile for d40k tracers was Gaussian for all protein concentrations and hence the diffusion coefficient could be determined. However, the intensity profile of both d500k and d2000k was not Gaussian for all protein concentrations except for d500k at 40 g/l and hence the diffusion coefficient of d500k could only be determined at $C=40 \text{ g/l}$. In Figure 3.11b, we have plotted D/D_0 as a function of the protein concentrations for different tracers at $C_s=0.05 \text{ M}$. It is clear that the effect of protein concentration and tracer size on D/D_0 is stronger at $C_s=0.05 \text{ M}$ than at 0.1 M salt.

In gels formed at $C_s = 0.1$ and 0.05 M , D/D_0 of all the tracers is systematically lower than η_0/η of the protein solutions for all C . This is expected because at these salt concentrations the gel structure is homogeneous and the pore size is relatively small.

Hence the friction caused by the immobile structure of the gel is much larger than that caused by the mobile native proteins in the solution. Croguennoc et al (Croguennoc et al., 2001) also observed that the diffusion of dextran molecules was faster in solution than in the corresponding gel.

The decrease of D/D_0 with increasing protein concentration can be explained by considering the fact that the pore size (correlation length) decreases with increasing protein concentration (Pouzot et al., 2004). Colsenet et al (Colsenet et al., 2006a, 2006b) also observed a decrease of the diffusion coefficient of PEO chains in whey protein gels at pH 6.88 and $C_s=0.1$ M with increasing protein concentrations.

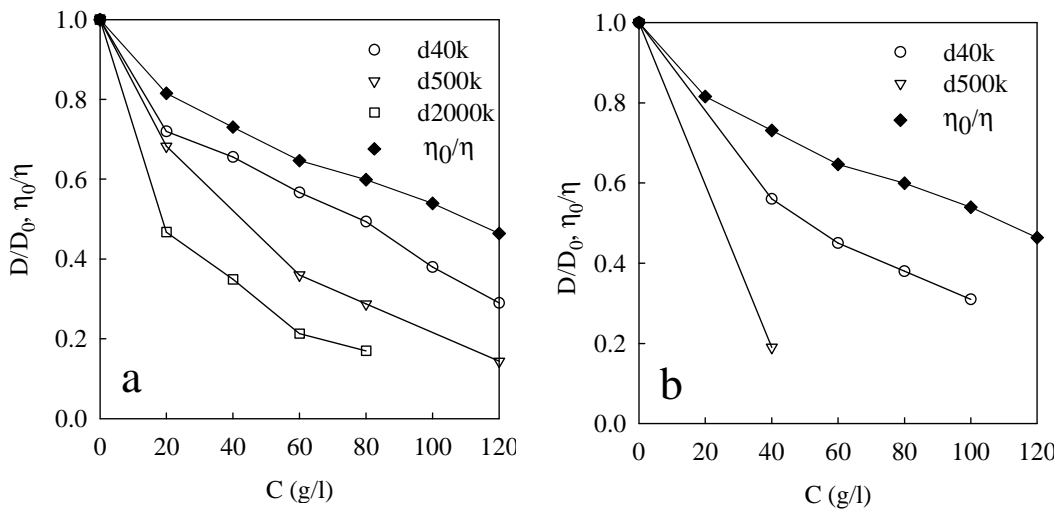


Figure 3.11. D/D_0 of different tracers in gels as a function of the protein concentrations at $C_s=0.1$ M (a) and at $C_s=0.05$ M (b).

In gels formed at $C_s=0.2$ M the tracers diffused normally for all protein concentrations tested. Figure 3.12 shows D/D_0 as a function of the protein concentration for different tracers at 0.2 M NaCl. D/D_0 decreased weakly with increasing C , but there was no systematic dependence of D/D_0 on the tracer size. This result confirms the similar observations for larger tracers by MPT at 0.2 M salt. However, D/D_0 was systematically larger for FITC-dextran molecules than for the latex particles. For comparison, D/D_0 obtained from MPT is also included in figure 3.12. From the graph it is clear that there exists some dependence of D/D_0 on tracer size even in the more heterogeneous gels.

The effect of the salt concentration between 0 to 0.2 M on the diffusion of FITC-dextran molecules was investigated more systematically at $C = 100$ g/l. D/D_0 increased with increasing salt concentration, see figure 3.13. For all salt concentrations d40k diffused normally and its diffusion coefficient could be determined. Interestingly, the intensity profile of d500k was Gaussian at $C_s = 0$ M, non Gaussian at $C_s = 0.05$ M, but again Gaussian for $C_s \geq 0.1$ M. Hence the diffusion coefficient of d500k could be determined for all salt concentrations except for $C_s=0.05$ M. In the case of d2000k the profile was only Gaussian for $C_s \geq 0.15$ M.

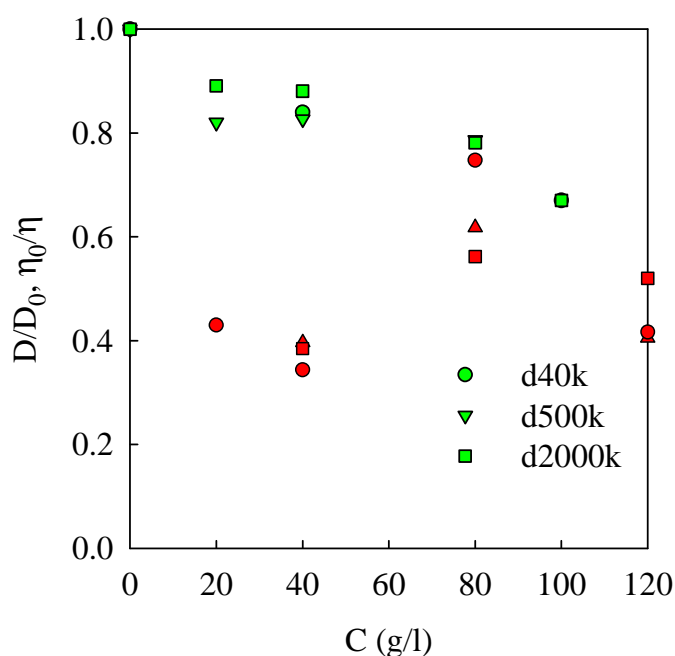


Figure 3.12. D/D_0 obtained from FRAP and MPT as a function of the protein concentration for different tracers in gels formed at 0.2 M NaCl. The green symbols represent the FRAP data whereas the red symbols shows the MPT data (particles with radii $R=0.1$, 0.25 and 0.5 μm are denoted as circles, triangles and squares, respectively.)

We observed a strong dependence of D/D_0 on the size of the tracer for salt concentrations up to $C_s=0.15$ M, but there was no dependence at $C_s=0.2$ M. It was noted that D/D_0 in gels was lower than the solution viscosity (see dotted line) at low salt concentrations ($C_s<0.15$ M) and higher at higher salt concentrations. The increase of D/D_0

with increasing salt concentration can be explained by the increase of the pore size of the gels (Ako, Durand et al., 2009) with increasing salt concentration

Almost full recovery of the fluorescence was found for those gels in which the diffusion coefficient of the tracer could be measured. However, if the intensity profile of the tracer was non Gaussian then a significant fraction of the tracers was trapped in the gel. We found that for $C_s \geq 0.1$ M, complete recovery was found for d500k at all protein concentrations, but for $C_s < 0.1$ M the fraction of mobile tracers decreased with increasing protein concentration.

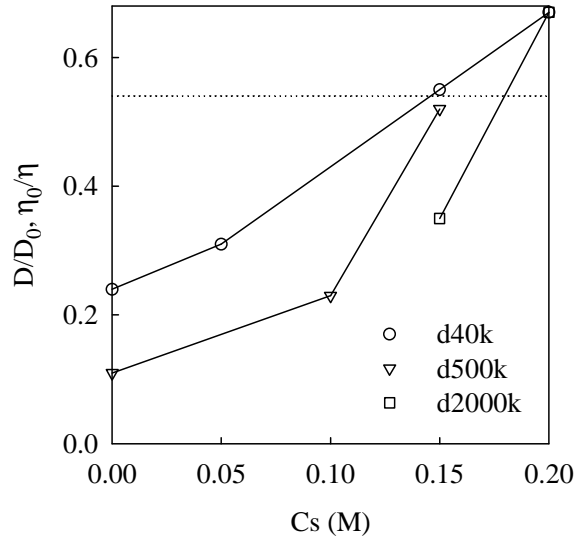


Figure 3.13. Plot of D/D_0 in gels as a function of salt concentrations (C_s) for different tracers as indicated in the graph at β -lg concentration $C=100$ g/l. The dotted line in the graph represents η_0/η for the corresponding native protein solutions at this concentration.

Figure 3.14a shows the normalized fluorescence recovery for d2000k as a function of time for different protein concentrations at $C_s=0.10$ M. For d2000k, almost complete fluorescence recovery was found for all protein concentrations for $C_s > 0.15$ M, but the mobile fraction of d2000k decreased with increasing protein concentration for $C_s \leq 0.15$ M. Figure 3.14 (b) shows the results for d500k at $C_s = 0.05$ M. For d40k complete fluorescence recovery was found for all salt and protein concentrations.

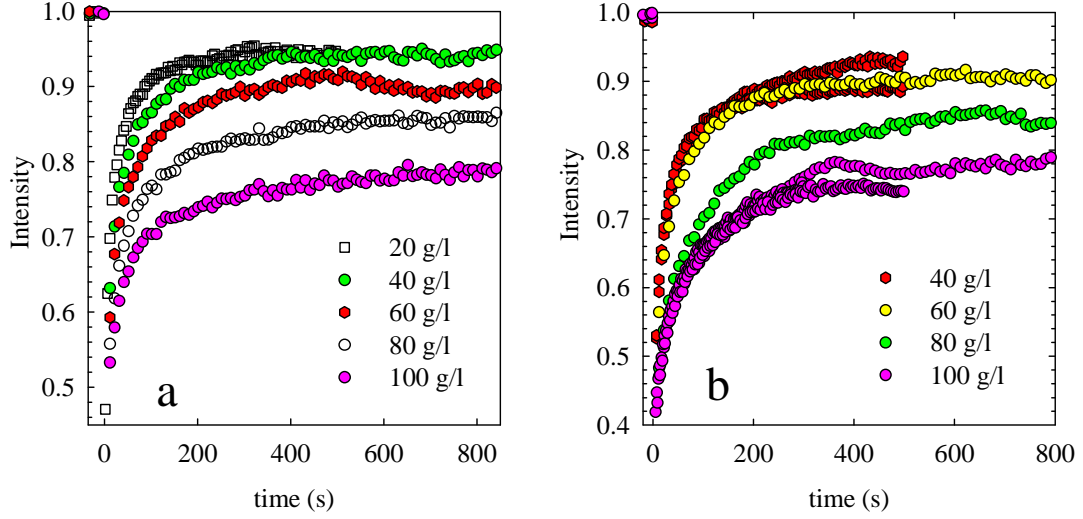


Figure 3.14. Normalized fluorescence recovery for d2000k (a) as a function of time for gels formed at $C_s=0.10M$ and different protein concentrations and (b) that of d500k at $0.05 M NaCl$.

We have determined the mobile fraction (F_m) of d500k and d2000k molecules in the gels at various salt and protein concentrations by using the relation,

$$F_m = \frac{I_f - I_{in}}{1 - I_{in}}$$

Where I_f is the normalized fluorescence intensity at infinite time after bleaching and I_{in} is the normalized fluorescence intensity immediately after bleaching. Figure 3.15 shows the mobile fraction of d500k (a) and d2000k (b) as a function of the protein concentration for different salt concentrations as indicated in the graph. From the graph it is clear that the mobile fraction decreased with increasing protein concentration for a given salt concentration. One might expect that for a given protein concentration the mobile fraction increases with increasing salt concentrations because the correlation length increases. However, we found that F_m was higher at $C_s = 0 M$ than at $C_s = 0.05 M$, see figure 3.15.

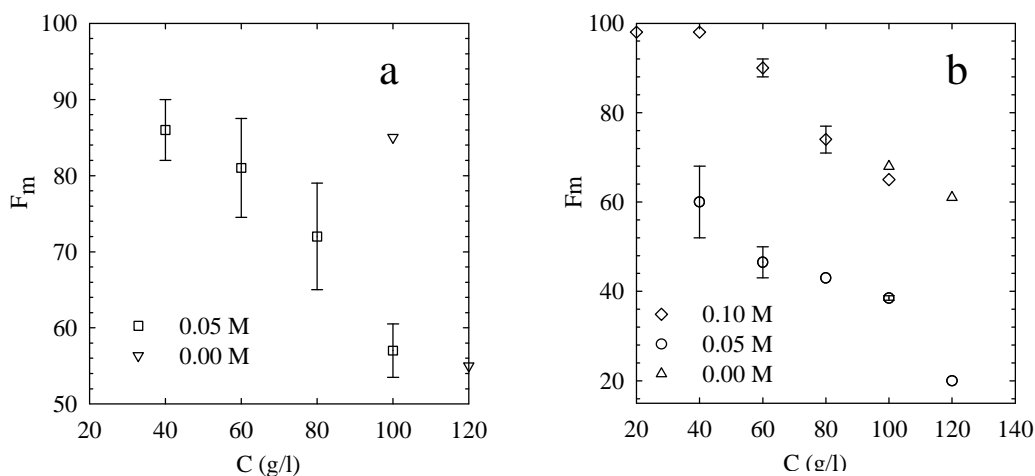


Figure 3.15. Mobile fraction of d500k (a) and d2000k (b) in gels as a function of protein concentrations for different NaCl concentrations indicated in the figure. The error bars illustrate the spread observed in repeated experiments.

We have investigated this interesting phenomenon in more detail at $C=100$ g/l, see Figure 3.16. Starting at $C_s=0$ M, F_m decreased first with increasing NaCl concentration, reached a minimum at $C_s=0.02$ M and increased again for $C_s \geq 0.05$ M.

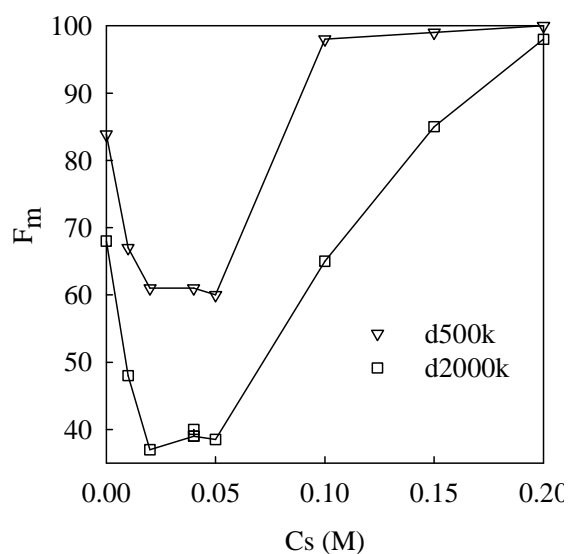


Figure 3.16. Mobile fraction of d500k and d2000k in β -lg gels as a function of the NaCl concentrations at $C=100$ g/l.

3.1.4. Discussion

Numerical simulations of tracer diffusion in colloidal gels, formed by diffusion or reaction limited aggregation of hard spheres, showed that the diffusion of the tracer was mainly controlled by the accessible volume to the spherical tracers (Babu et al., 2008), see chapter.1. It was found that the diffusion coefficient of the tracers decreased with increasing volume fraction of the gel. Here we also observed a decrease of D/D_0 of dextran molecules with increasing β -lg concentration for homogeneous gels ($C_s \leq 0.15$ M). On the other hand, for microphase separated gels, there was no systematic dependence of D/D_0 on the protein concentration. This could be explained by the fact that the increase the protein concentration was compensated by an increase in the density of the particles that formed the gels.

Computer simulations also showed that for a given gel volume fraction D/D_0 decreased with increasing tracer size, but in this study both MPT and FRAP, showed that there was no systematic dependence of D/D_0 on the tracer size for heterogeneous gels. However, the values for the smaller and flexible dextran chains were systematically higher than for the latex particles. Apparently, the effect of size on D/D_0 was smaller than the experimental error for the size range covered in the MPT and FRAP experiments. For homogeneous gels formed at lower salt concentrations ($C_s \leq 0.15$ M), D/D_0 decreases with increasing tracer size for a given protein concentration.

We found that trapping of particles depended on the tracer size both in heterogeneous and homogeneous gels. One might think that the trapping of particles is determined by the average pore size which is expected to be proportional to the correlation length. But particle tracking measurements showed that particles with $d=2 \mu\text{m}$ were diffusing normally in gels with $\xi=1.3 \mu\text{m}$ while 10 times smaller particles were trapped in gels with only two times smaller correlation length, $\xi=0.65$. This remarkable observation demonstrates that trapping of the particles cannot be related directly to the correlation length of the gel. Probably, the pore size distribution is an important factor which is not reflected by ξ .

In some cases we observed anomalous diffusion of latex particles. Simulations also showed in some situations anomalous diffusion of spherical tracers (Babu et al., 2008). The simulations covered many orders of magnitude both in time and distance scales, but for comparison with the experimental results we plotted the simulation results

corresponding to the experimental time and distance scales in figure 3.9 (b). The simulation results show a transition from normal diffusion to trapping via anomalous diffusion as a function of accessible volume. The transition is reflected by anomalous power law dependence over the limited scale covered in the experiments.

The origin of the anomalous diffusion is that the gels are heterogeneous and the tracers encounter different environments. Some tracers are situated in more constrained areas or may even be trapped, while others can diffuse more freely. Therefore, both the simulations and the experiments show a broader distribution of the displacements when the diffusion is anomalous than the Gaussian distribution that is expected for Brownian diffusion. As much longer time scales can be covered, the broadening is better observed in the simulations (Babu et al., 2008). The simulations show that close to the critical point the distribution becomes bimodal at long times. One peak represents the trapped particles and its position is stable with time, while the other peak represents the diffusing tracers and shifts to larger distances.

We also observed partial trapping of dextran molecules at lower salt concentrations. The observation that a fraction of the dextran chains diffuses freely and another is completely trapped can be explained by their broad size distribution. It was found that the mobile fraction of the tracers decreased with increasing protein concentration for a given salt concentration, see figure 3.16. This is expected since the average pore size decreases with increasing protein concentrations, so that increasingly smaller chains become trapped.

One might expect for the same reason that F_m increases with increasing NaCl concentration. However, a minimum of F_m was found as a function of the salt concentrations. This remarkable result could possibly be explained by considering the pore size distribution. The proteins strands that form the gel are relatively ordered at $C_s=0$ M resulting in a narrow pore size distribution. With increasing ionic strength the strands become less ordered and the pore size distribution broadens. This leads to an increase of the z-average correlation length, but locally domains with smaller pores could trap smaller dextran chains. The minimum reflects the combined effects of increasing the average pore size and the pore size distribution on trapping of polydisperse tracers.

3.1.5. Conclusion

The main conclusion of this work is that the diffusion of tracers in globular protein gels can be investigated successfully for a spectrum of salt concentrations ($C_s=0$ to 0.25 M) by combining CLSM with multiple particle tracking and FRAP. MPT with CLSM has proven to be a powerful tool for measuring the diffusion of tracer particles in heterogeneous gels ($C_s \geq 0.15$ M). On the other hand FRAP is a useful tool to study the diffusion of smaller molecules in homogeneous gels ($C_s \leq 0.15$ M). Unfortunately, there was a significant scattering of D/D_0 values obtained by MPT, probably due to relatively smaller amounts of particles that can be tracked.

It was found that D/D_0 for heterogeneous gels decreased only weakly with increasing protein concentration because the density of the gel phase increased with increasing protein concentration. Another remarkable observation from MPT was that the size of trapped particles cannot be correlated to the correlation length of the particles. This means that pore size distribution is probably an important factor for the mobility of the particles.

In the case of homogeneous gels D/D_0 decreased both with increasing tracer size and increasing protein concentrations. At lower salt concentrations and higher protein concentrations a fraction of the larger tracers was trapped in the gels. For a given salt concentration ($C_s < 0.1$ M for d500k and for d2000k $C_s < 0.2$ M), the mobile fraction of the tracers decreased with increasing protein concentration. However, for a given protein concentration the fraction of mobile tracers showed a minimum between $C_s=0.02$ M and $C_s=0.05$ M. The minimum can be attributed to a combination of the increase of both the average correlation length and the width of pore size distribution. This observation again leads to the conclusion that trapping of tracers cannot be understood solely on the base of the average pore size. It is necessary to consider also the pore size distribution.

3.2. Particle diffusion at the interface of water-in-water emulsion.

3.2.1. Introduction

In this section we will investigate in detail the adsorption of latex particles at the droplet interface of water in water emulsions formed by mixing aqueous solutions of PEO and dextran. CLSM allows one to visualize both the particles and the dextran phase simultaneously as described in chapter 2. The effect of particle size was studied by varying their radii between 0.1 and 1 μm . We will show that trapping of particles at the interface of water in water emulsions can be explained by the reduction of interfacial tension even though the latter is much smaller than in oil in water emulsions. The interfacial tension of the mixtures was determined from droplet deformation studies as described in chapter 2.

The organization of the particles at the interface was studied for different compositions of the mixtures and hence different interfacial tensions. At low surface coverage the particles diffused freely at the interface and the diffusion could be determined by multi-particle tracking as described in chapter 2. We will show that the diffusion coefficient of the particles depends on the contact angle with the interface and the viscosity of each phase. Finally, we show that the Pickering effect in water in water emulsion can also be produced with protein particles, which has potential application in food and cosmetics.

3.2.2. Results and discussion

It is well known that PEO and dextran are incompatible at higher concentrations (Forciniti, Hall, & Kula, 1991). The phase diagram of PEO and dextran mixtures was made by varying the concentrations of PEO and dextran as illustrated in the figure 3.17. The critical point of this phase diagram is at $C_{\text{PEO}}=1 \text{ wt\%}$ and $C_{\text{dex}}=1.7 \text{ wt\%}$. The tie-lines are parallel and are deduced from the volume fractions of PEO and dextran after phase separation.

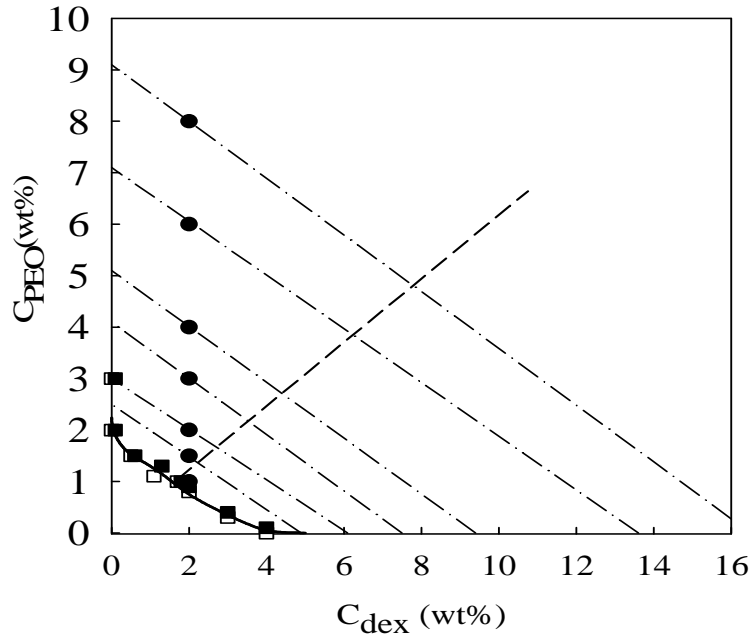


Figure 3.17. The phase diagram of PEO/dextran mixtures. Homogeneous and phase separated samples are represented by open and filled point respectively. The solid line is the binodal and the dashed dotted lines are the tie-lines for mixtures indicated by the circles. The dashed line separates systems with a larger PEO rich phase from those with a larger dextran rich phase.

The Pickering emulsion was prepared by mixing latex particles, PEO and dextran as explained in chapter 2. In most of the cases the continuous phase was PEO and the dispersed phase was dextran, but the inverse also could be prepared by varying the volume fractions of each phase. Figure 3.18 shows a CLSM image of a droplet of the dextran rich phase covered by latex particles with $r=0.25 \mu\text{m}$ in a matrix of the PEO rich phase. In most cases we found that some excess particles are dispersed in the PEO phase but none of the particles were found in the dextran phase. This could be explained by the fact the PEO is readily adsorbed on the surface of the latex particles.

Particles with radius $R=1 \mu\text{m}$ were used to measure the contact angle of the particles with the dextran droplet. The measured contact angle averaged over many particles was $140 \pm 5^\circ$. More than 90° is expected since the particles prefer the PEO phase over the dextran phase. For a solid particle at the PEO-dextran interface, the contact angle is related to three interfacial tensions: (Aveyard et al., 2003),

$$\gamma_{AB} \cos \theta = \gamma_{PA} - \gamma_{PB}$$

3.1

where γ_{AB} is the interfacial tension of the PEO-dextran interface, γ_{PA} is the interfacial tension of the PEO-particle interface and γ_{PB} is the interfacial tension of the dextran-particle interface. In this case it is clear that $\gamma_{PA} < \gamma_{PB}$. It was found that the contact angle of the particles doesn't depend strongly on the composition of the mixtures. Figure 3.19 shows an image of a latex particle at the surface of a dextran droplet in the PEO matrix.

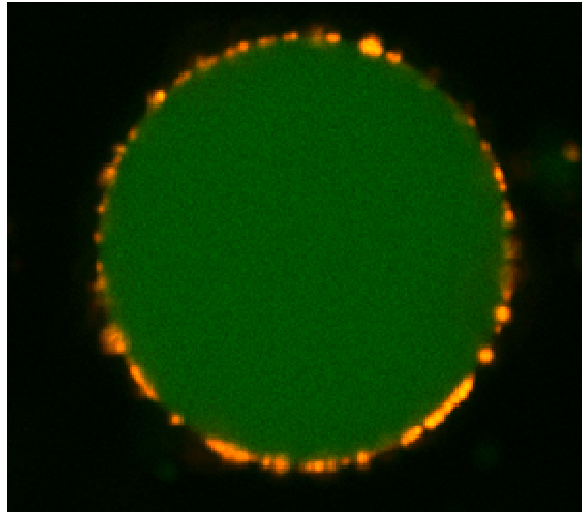


Figure 3.18. CLSM image focused at the center of a droplet of the dextran phase (green) in a matrix of the PEO phase. The latex particles (yellow) have radius of $0.25\mu\text{m}$. ($C_{\text{PEO}}=4.0 \text{ wt\%}$, $C_{\text{dex}}=2.0 \text{ wt\%}$).

A series of mixtures prepared by varying the PEO concentration up to 8.0 wt% at a fixed dextran concentration of 2.0 wt% were investigated in detail. In all the cases particle concentration was kept at 0.08%. It was found that the mixtures phase separated for $C_{\text{PEO}} \geq 0.8 \text{ wt\%}$. We observed that at 2.0 wt% dextran, particles could be trapped at the interface for PEO concentrations down to 1.7 wt%, but not for 1.5 wt%. The amount of trapped particles increased with increasing time, which could be partly due to the fusion of droplets which allows some free particles to get at the interface. Interestingly, simple Brownian diffusion of the particles was not efficient for trapping since we

observed many particles collision with the interface, but none of them resulted in trapping. The time needed to attain a reasonable covering depended on the PEO concentration. We found that for 8.0 wt% PEO it took a few minutes to obtain a good covering, while at 2.0 wt% PEO it took more than 30 minutes. The fraction of free particles increased with decreasing PEO concentration and at 1.7 wt% PEO most of the particles were free and situated in the PEO rich phase. Particles with various radii (0.1-1 μm) were used to investigate the effect of particle size on the kinetics of trapping. In all cases we observed that the particles cover the interface down to C_{PEO} 1.7 wt%, but larger particles took longer to cover the droplets.

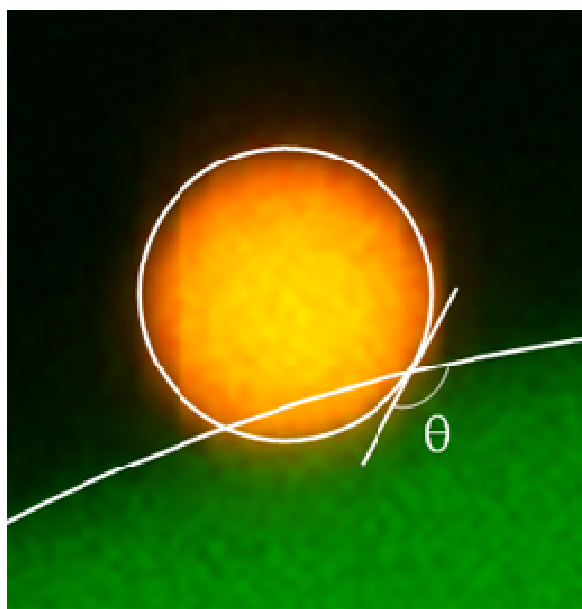


Figure 3.19. CLSM image of a latex particle (yellow) at the surface of a dextran droplet (green) in the PEO matrix. The white lines indicate the surface of the particle and the droplet. The contact angle θ with respect to the dextran phase is shown.

The amount of energy required to remove a spherical particle with radius R from the PEO-dextran interface is determined by the interfacial tension, see Eq. 1.6. In order to measure the interfacial tension of the mixtures we have used droplet deformation studies, see chapter 2. We observed that the interfacial tension increased with the tie line length

following a power law: $\gamma_{AB} \propto (\text{TLL})^{3.9}$, as was earlier reported for other PEO-dextran mixtures (Forciniti et al., 1991; Wu, Zhu, Lin, & Li, 1999), see Figure 3.20.

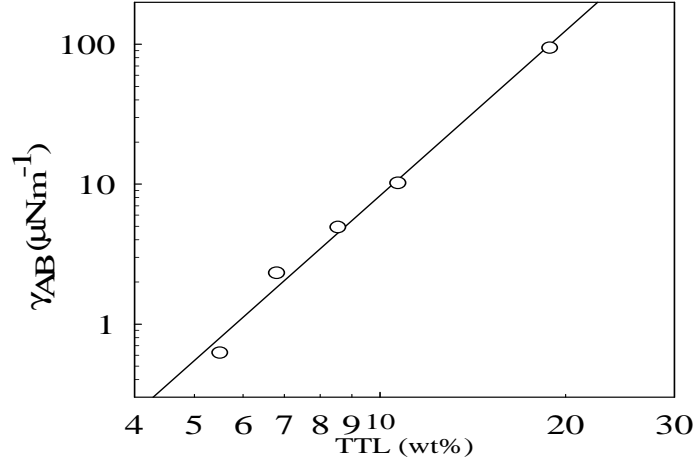


Figure 3.20. Interfacial tension as a function of tie line length for mixtures of 2 wt% dextran and varying concentrations of PEO. The solid line represents the results of a linear least squares fit and has a slope of 3.9.

We now have the three parameters needed to calculate the amount of energy required to remove a spherical particle from the interface: particle size, interfacial tension and contact angle. As mentioned above, we found that the particles were trapped at the interface down to $C_{\text{PEO}} = 1.7$ wt%. At this concentration the free energy needed to remove a spherical particle from the interface is $\Delta G = 2 \times 10^{-20}$ Nm, i.e. $\Delta G = 7kT$. This shows that trapping of particles at the interface of water in water emulsions could be explained on the basis of the reduction of the interfacial tension even if it is very low compared to oil-water emulsions. One might expect that larger particles can provide significant covering closer to the critical point since $\Delta G \propto R^2$. However, this was not observed. It may be explained by the fact that larger particles took a longer time to get trapped at the interface. Close to the critical point the system evolve quickly, so that perhaps there simply wasn't enough time for larger particles to enter the interface.

We never observed a trapped particle escape from the interface implying that trapping of the particles at the interface in PEO-dextran mixtures was irreversible.

Nevertheless, even completely covered particles could fuse and expel particles from the surface in this process. Apparently shear forces during fusion are sufficient to expel the particles. Figure 3.21 illustrates the fusion of two droplets and its subsequent relaxation to a spherical shape. The process of fusion starts by forming a whole in the particle layer (b) that grows rapidly (c) until there is no curvature between the droplets (d). Relaxation to a spherical shape is relatively slow (f) because the viscosities of the media are high and the interfacial tension is small.

If the coverage is relatively low, it is often heterogeneous with some droplets being more densely covered than others. One can also observe heterogeneous coverage of the same droplet on large length scales, which appears in first instance to be in contradiction with the observation that the particles can freely diffuse at the interface. It can, however, be explained by the fusion of droplets. When a small droplet fuses with a larger droplet all the particles at the interface of the smaller droplet are gathered at one area of the larger droplet with which it merged, see figure 3.22.

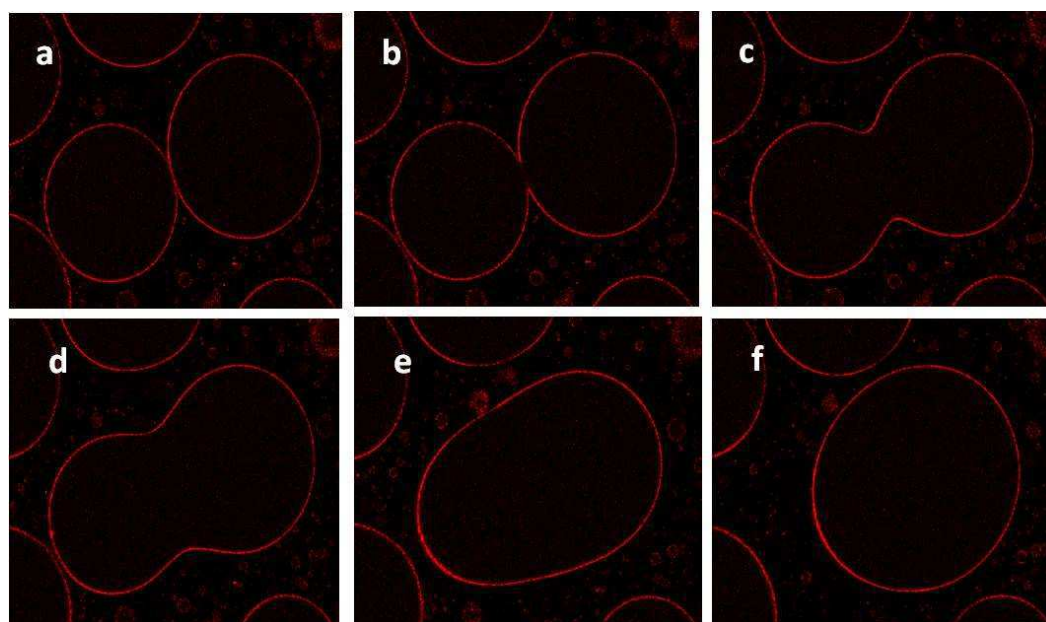


Figure 3.21. CLSM images during fusion of two droplets of the dextran phase in the PEO matrix. The droplets were covered with latex particles (red) with a radius of $0.25\mu\text{m}$. Figures a-d were taken at time intervals of 0.31s . Image e was taken after 3s and image f after 30s .

The ease of removal of particles from the interface depends on the PEO concentration. It was found that for $C_{\text{PEO}} = 8.0$ wt%, strong shear forces were required to remove particles from the interface. On the other hand, gentle stirring was sufficient to remove particles when $C_{\text{PEO}} < 2.5$ wt%. After macroscopic phase separation all particles were situated either at the interface of the two phases or in the PEO rich phase.

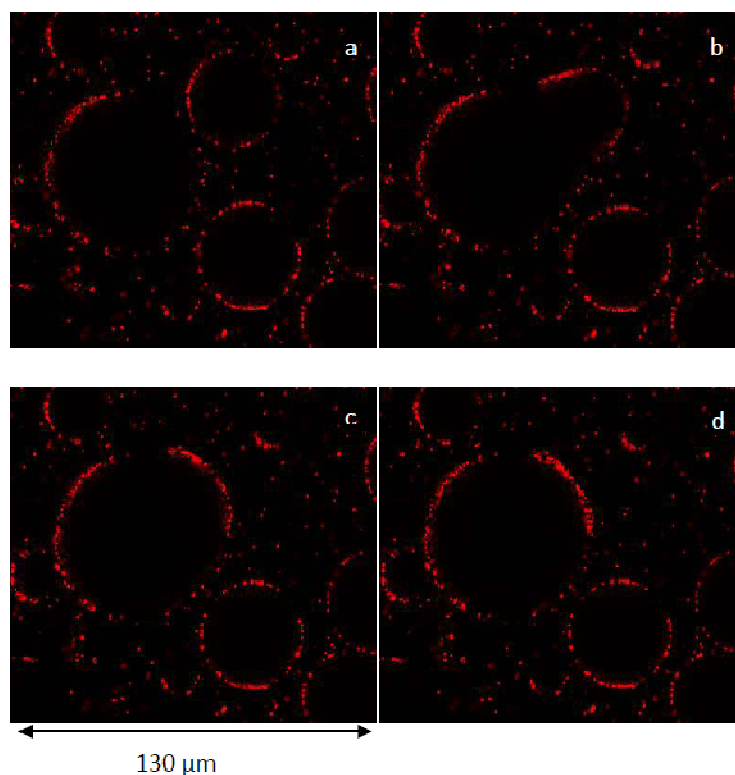


Figure 3.22. CLSM images during fusion of two droplets of the dextran phase in the PEO matrix. The droplets were partially covered with latex particles (red) with a radius of $0.25\mu\text{m}$.

3.2.3. Structure of the particles at the interface

We observed that the morphology of the particles at the interface depends on the density of the particles at the interface. It was found that the density of the particles at the interface could be increased to some extent by increasing the particle concentration, but full coverage was not obtained and the excess particles were situated in the PEO rich phase. In order to obtain dense coverage it was necessary to use high PEO and dextran concentrations and thus to have a higher interfacial tension. Figure 3.23 shows images of

droplets with different coverage density that were taken by focusing at the top surface of a droplet. The larger bright spots in the images correspond to 3 dimensional clusters of particles that were also observed in the PEO rich bulk phase. It is worth mentioning that there is no specific interaction between the particles, but the osmotic pressure from the depletion of PEO between particles produces an attractive force which increases with increasing PEO concentration and drives clustering of particles.

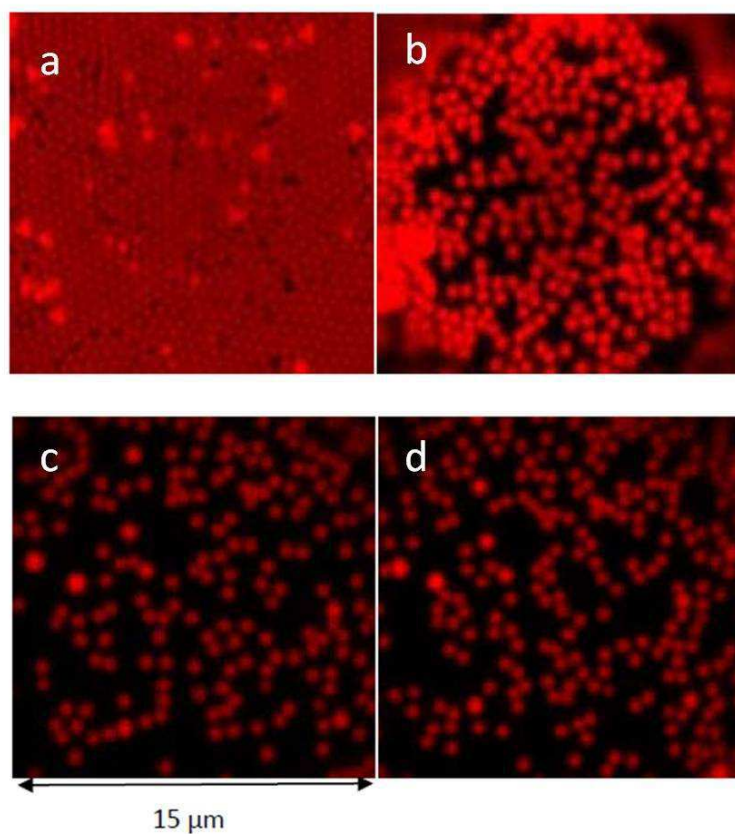


Figure 3.23. CLSM images focused at the top of droplets of the dextran phase in the PEO matrix. The droplets were covered with latex particles (red) with a radius of $0.25\mu\text{m}$. Images c and d are from the same droplet at 200 s interval. (a: $C_{\text{PEO}}=8.0\text{ wt\%}$, $C_{\text{dex}}=7.0\text{ wt\%}$; b: $C_{\text{PEO}}=6.0\text{ wt\%}$, $C_{\text{dex}}=2.0\text{ wt\%}$; c, d: $C_{\text{PEO}}=8.0\text{ wt\%}$, $C_{\text{dex}}=2.0\text{ wt\%}$).

The average density of particles at the surface increased with increasing polymer concentrations, see figure 3.23. In mixtures of 8.0 wt% PEO and 7.0 wt% dextran, the latex particles form a hexagonal crystalline structure interspersed with defects (Figure 3.23 (a)), but within the same system some other droplets were only partially covered. If

the coverage is intermediate, the particles form clusters (Figure 3.23 (b)). At low coverage, particle association is transient as is illustrated by comparing two snapshots taken with 200 s interval (c and d).

3.2.4. Mobility of the particles at the interface

The mobility of the particles at the interface was studied by monitoring their displacement with CLSM. At low coverage, each particle sees on average the same environment and the MSD of the particles at the interface increases linearly with time. Figure 3.24 shows the MSD of particles with radius 0.25 μm (a) and 0.5 μm (b) as a function of time for droplets formed in mixtures of 2.0 wt% dextran and different PEO concentrations.

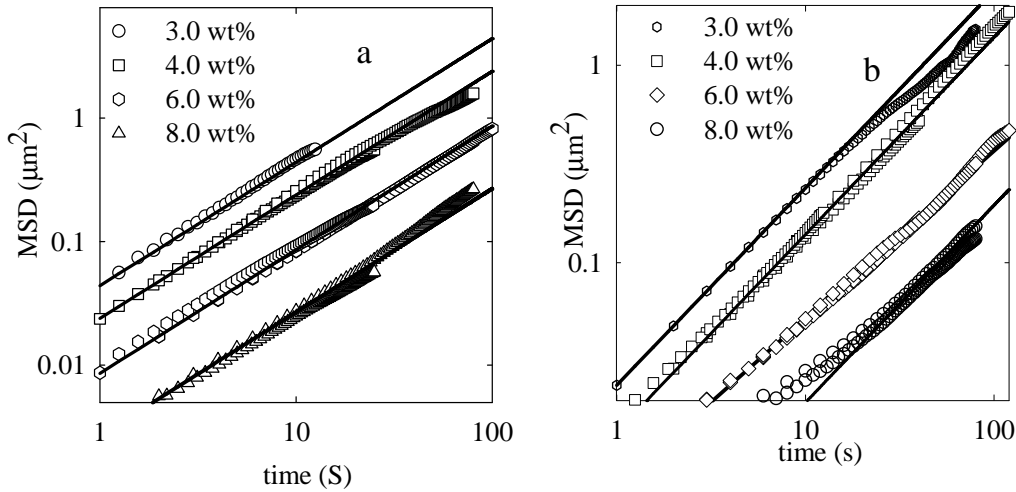


Figure 3.24. MSD of particles with radius 0.25 μm (a) and 0.5 μm (b) as a function of time for droplets formed in mixtures of 2.0 wt% dextran and different PEO concentrations indicated in the figure

For a given time the MSD of the particles is higher when the PEO concentration is lower. The diffusion coefficient of the particles was determined from the slope: $\text{MSD} = 2Dt$. D/D_0 is plotted in figure 3.25 as a function of the PEO concentrations. D/D_0 decreased with increasing PEO concentration, but there was no effect of the size of the particles on the normalized diffusion coefficient at the interface.

It was found that the diffusion coefficient of the particles at the interface was closer to that in the PEO bulk phase than in the dextran phase. This is explained by considering the total surface area of the particles that is in contact with the two phases. The surface area of the particles in each phase was calculated from the contact angle (θ) by using the relations:

$$S_A = (1 - \cos \theta)/2 \quad 3.2$$

$$S_B = (1 + \cos \theta)/2 \quad 3.3$$

where S_A and S_B are the fractions of the surface area in the PEO and the dextran phase, respectively. The equations show that the surface area of the particle in the PEO phase is much larger than in the dextran phase for $\theta=140^\circ$.

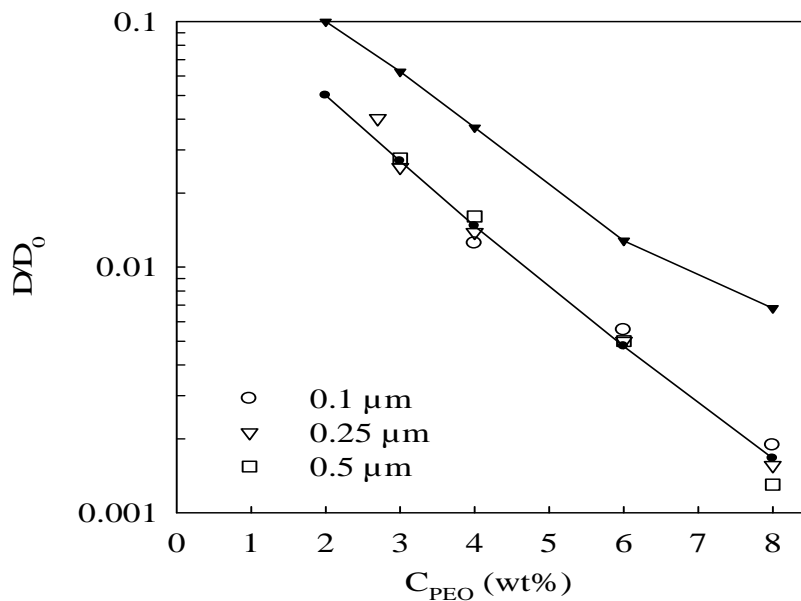


Figure 3.25. D/D_0 of latex particles with different radii at the interface between the dextran and PEO phases as a function of the PEO concentration in mixtures with 2.0 wt% dextran. The values obtained in the bulk PEO and dextran phases are indicated as filled circles and triangles, respectively.

The effective viscosity felt by the particles at the interface can be calculated as:

$$\eta_{eff} = ((1 - \cos \theta)\eta_A + (1 + \cos \theta)\eta_B)/2 \quad 3.4$$

Substituting for $\theta = 145^\circ$, we find

$$\eta_{eff} = 0.9\eta_A + 0.1\eta_B \quad 3.5$$

where η_{eff} is the effective viscosity of the particles at the interface, η_A is the viscosity of the PEO phase and η_B is that of the dextran phase. Eq. 3.5 shows that 90 % of the effective viscosity that a particle feels at the interface came from the PEO phase and this explains why the diffusion coefficient of the particles at the interface is much closer to that in the PEO bulk phase than in the dextran phase. Here we ignored the effect of interface itself since there was no size dependence of the particles on the diffusion.

3.2.5. Protein particles at the interface

Spherical protein particles with radii of 0.1 and 0.5 μm were used to test if protein particles could induce a Pickering effect in water in water emulsion. The particles were more polydisperse and less spherical than the latex particles, but are relevant to food applications. Again we investigated the trapping of particles as a function of the PEO concentration at 2 wt% dextran. It was found that particles can easily become trapped for $C_{\text{PEO}} \geq 2.0$ wt%. The main differences between latex particles and protein particles were that trapping of protein particles was faster and the excess particles went to the dextran rich phase instead of the PEO rich phase. The rate of phase separation was reduced by the presence protein particles, but macroscopic phase separation occurred eventually. Figure 3.26 shows a CLSM image of protein particles with radius $r = 0.25$ μm at the interface of droplets in a PEO-dextran mixture containing $C_{\text{PEO}}=3.5$ wt% and $C_{\text{dex}}=2.0$ wt%.

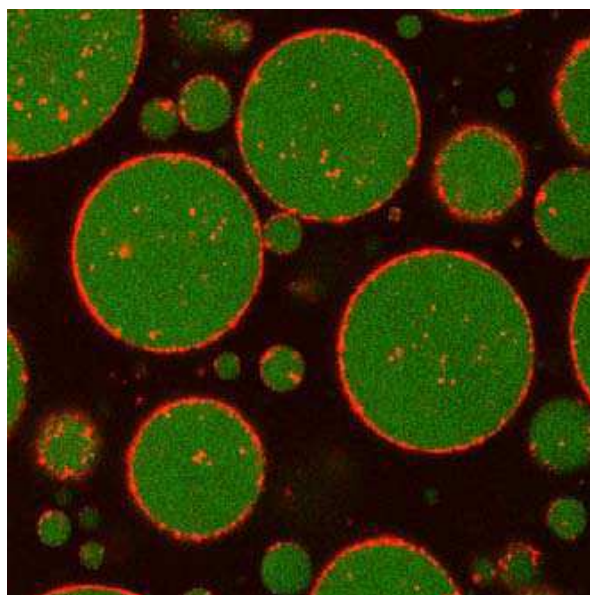


Figure 3.26. CLSM image of protein particles (orange) at the interface of emulsion droplets in a PEO-dextran (green) mixture containing $C_{PEO}=3.5$ wt% and $C_{dex}=2.0$ wt%.

3.2.6. Conclusion

Particles with radii between 0.1 and 1 μm could be trapped at the interface of droplets in water in water emulsions formed by mixing aqueous solutions of PEO and dextran. Particles were trapped at interfaces with interfacial tensions down to 1 $\mu\text{N/m}$. The trapping of particles at the interface in water in water emulsions could be explained by the reduction of the interfacial tension in spite of the fact that they are much lower than in oil-water emulsions. The structure of particles at the interface varied from a hexagonal crystalline order to a dilute random distribution with transient cluster formation at intermediate coverage. The transient association of the particles is driven by depletion of PEO between the particles. Unfortunately, particles are not efficient in stabilizing the water in water emulsions contrary to oil in water emulsions, because the shear forces induced by coalescence or external shear can easily drive the particles from the interface.

General Conclusions

General Conclusions

We have shown that CLSM can be a very useful tool to measure the displacement of tracer particles in globular protein gels and at the droplet interface of emulsions. CLSM needs to be combined with two different techniques to study the diffusion of tracers with a wide range of sizes in gels having a wide range of average pore sizes. CLSM combined with MPT could be used to investigate the diffusion of spherical particles ($R=0.1-1\mu\text{m}$) in heterogeneous gels. For homogeneous gels, CLSM with FRAP was most useful because for these gels only small tracers ($R<100\text{nm}$) were mobile. A drawback of MPT was that the experimental error is higher than alternative techniques such as DLS, pulsed-field gradient NMR, and FRAP, because the number of particles that are tracked is relatively small.

For β -lg gels formed in the presence of 0.25 M or more NaCl, Brownian diffusion of all the probes was observed. For β -lg gels formed in the presence of 0.1 M or less NaCl, all the latex particles were trapped in the gel matrix. If the diffusion of the tracer is Brownian, then its diffusion coefficient could be determined. It was found that the diffusion coefficient of the latex particles in heterogeneous gels decreases with increasing volume fraction of the gel. However, the gel volume fraction, and thus the diffusion coefficient was not very sensitive to the protein concentration, because an increase of the protein concentration resulted in an increase of the density of the gel phase. Another remarkable finding was that D/D_0 was almost independent of tracer size.

In a few cases we observed anomalous diffusion of latex particles. There was strong size dependence of the tracer size on the transition from Brownian diffusion to trapping via anomalous diffusion. For example, tracers with $R=0.5\mu\text{m}$ diffused anomalously in gels with $C=20\text{ g/l}$ and $C_s=0.2\text{ M}$, while tracers with $R=1\mu\text{m}$ were trapped and tracers with $R=0.1\mu\text{m}$ diffused normally. Anomalous diffusion is caused by the heterogeneous environment of the tracer particles.

An important finding was that the diameter at which particles become trapped cannot be correlated directly to the correlation length and hence the average pore size of the gel. We observed Brownian diffusion of particles with $R=1\mu\text{m}$ in the gels with correlation length, $\xi=1.3\mu\text{m}$, while particles with $R=0.1\mu\text{m}$ were trapped in gels with correlation, $\xi=0.6\mu\text{m}$, which means that lowering the correlation length by a factor of 2

resulted into trapping of 10 times smaller particles. This interesting result indicates that trapping of particles is also determined by the distribution of pore sizes rather than just the average pore size of the gel.

Contrary to heterogeneous gels, D/D_0 of tracers in homogeneous gels decreased strongly with increasing tracer size and protein concentration. This shows that at lower salt concentrations ($C_s \leq 0.15$), there is a strong correlation between the protein concentration and pore size of β -Ig which decreased with increasing protein concentration.

In some cases we observed partial trapping of the dextran chains. This can be explained by considering that unlike latex particles the dextran chains used in the FRAP experiments were polydisperse and hence a fraction of smaller dextran chains can diffuse normally while the bigger chains are trapped in the matrix. A larger fraction was trapped if the tracers were on average larger or if the protein concentration was higher.

Interestingly, a minimum of mobile chains was found as a function of the salt concentration between $C_s = 0.02$ and 0.05 M. The minimum reflects the combined effects of increasing the average pore size and increasing the pore size distribution on the trapping of polydisperse tracers. This result shows once more that the mobility of tracer particles in globular protein gels is strongly correlated to the gel structure both in terms of average pore size and pore size distribution.

Particles can be trapped at the droplet interface of water-in-water emulsions formed by mixing aqueous solutions of PEO and dextran. We found that particles were trapped at the interface for interfacial tensions down to $1 \mu\text{N/m}$. Even though the interfacial tension is very low, its reduction by introducing particles at the interface can still explain the particle trapping. At low coverage density, particles diffused freely at the interface with a diffusion coefficient that was determined by the viscosity of the two phases and the contact angle. At low coverage, transient association of the particles occurred which is driven by depletion of the polymers between particles in contact. On very densely covered droplets the particles show long range hexagonal crystalline order. The low interfacial tension means that the particles can easily be driven from the surface by shear forces. Therefore, fusion of particle covered droplets was possible leading to macroscopic phase separation.

Annex

Annex

Annex-1. Multiple-particle tracking Algorithm.

The tracking algorithm is written in IDL language and can be divided into four different stages: (a) correcting the imperfections in each individual image (b) accurately locating the particle positions (c) eliminating false or unwanted particles and (d) correlating the particle positions with time to create trajectories. Below, I will illustrate these processes in detail with the help of an example.

We will consider a stack of images that tracks the displacements of 0.5 micron particles in water with a dt of 0.3 s. The name of this stack is “test.tif” (where tif is a format in which the images are saved). In the first step, we use a function called `readtiffstack`, which can read in tiff stacks. The general format of this command is, `a=readtiffstack('filename.tif')`. In our case the file name is test.

- `a= readtiffstack ('test.tif')`

Now all the two hundred images are stored in ‘a’ (`a=Array [512,512,200]` each image consists of 512×512 pixels and 200 is the total number of images in the stack)

- `movie,a`

This command displays all images as a film.

Initially, we will treat one image of the stack to find the optimum parameters required to find the particles in the image. Then these parameters are applied to all two hundred images in the stack.

- `a0=a(*,*,i)`

Now `a0` corresponds to the *i*th image (*i*=0 corresponds to the first).

- `tvsc1,a0`

This command displays the image and is shown in figure.A.1.1.

The images may suffer from a range of imperfections including geometric distortion, nonuniform contrast and noise. All these imperfections can frustrate the tracking. As mentioned above, the first stage of the tracking algorithm is to correct these imperfections. These imperfections can be sensibly removed by applying a spatial band-pass filter to the image (Crocker, JC and Grier DG., 1996). In IDL: `bpass.pro` is used to filter images. `bpass` is a spatial bandpass filter which smooths the image and subtracts the

background. This programme requires two parameters which are the spatial wave length cutoffs in pixels.

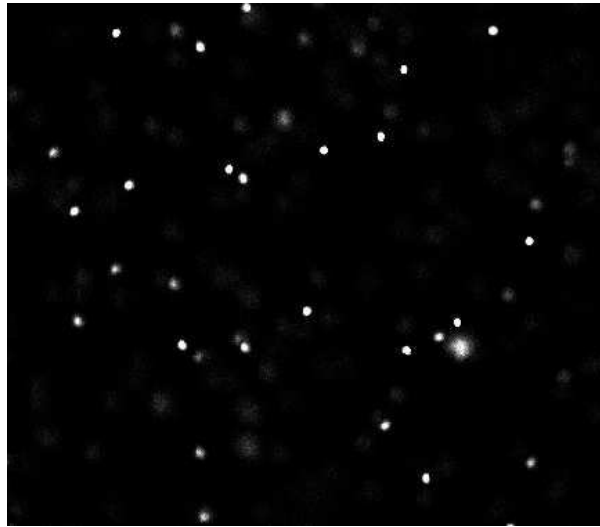


Figure.A.1.1. Shows the test image a0 and the particles in it

The first number is always one while the second number is close to the diameter of the particles that we want to find in pixels. Use the value that gives nice, sharply peaked circular blobs where the particles were. So a0, the single image to be examined is subjected to the spatial band-pass filter bpass.

- `b=bpass(a0,1,8)`

In this example the blobs diameter is 8 pixels and the filtered image is stored in b. The command 'tvscl' mentioned above can be used to inspect the filtered image b, see figureA.1.2.



Figure.A.1.2. Shows the filtered image b with an upper cutoff of 8.

The filtered image consists of bright spots on a dark background. The local brightness maxima in the image can be considered as candidate particle positions. A pixel corresponds to a particle center if no other pixel has higher intensity within a given distance; typically this distance is slightly larger than the particle radius. This reasonable assumption enables one to find the particle centroids to within half a pixel. In this algorithm `feature.pro` is used computes the brightness-weighted centroid within the circular blobs. This program requires the user to specify the size of the circular blob which is same as that of the upper cutoff of `bpass` filter. If the size of this circular blob is too large, then there is a possibility of finding multiple centers for the same particle. It is better to keep the size of the circular disc only slightly larger than the particle diameter. In our case size of the circular blob is 6 and we are going to apply the `feature.pro` on the filtered image b. This step enables us to accurately locate the particles position that is the second processing stage of the tracking algorithm.

- `f=feature(b,8)`

The variable `f` has five columns and each corresponds to different features of the particles in the image. These columns are x-centroid (0th), y-centroid (1st), total brightness (2nd), radius of gyration (3rd) and eccentricity (4th) which is 0 for circles and 1 for lines. The limitation of `feature.pro` is that it identifies the particle centers in terms of intensity and hence undesired intensity modulation can cause errors in the particle location which has to be eliminated in the third stage of the tracking algorithm. The elimination of

spurious or unwanted particles are carried out with the help of the above variable “f” since it has the information of total brightness (2nd column), radius of gyration (3rd column) and eccentricity (4th column) of the particles. Thus false particles can be eliminated by either restricting the acceptable values of total brightness, radius of gyration or the eccentricity of the particles.

- `f2=eclip(f,[2,3000,10000])`

Here 2 represents the 2nd column of f which is the total brightness of the particles, 3000 is the lower cutoff of the brightness and 10000 corresponds to the maximum accepted brightness of the particles. Thus the above command selects only those particles that have brightness between 3000 and 10000 and removes the others.

- `f2=eclip(f,[3,1,5])`

Selects only those particles that have radius of gyration between 1 and 5.

- `f2=eclip(f,[4,0,0.3])`

Selects only those particles with eccentricity between 0 and 0.3.

- `fo2=fover2d(a0,f2,radius=15,/circle)`

This command visualizes the selected particles in the image, see figure.A.1.3.

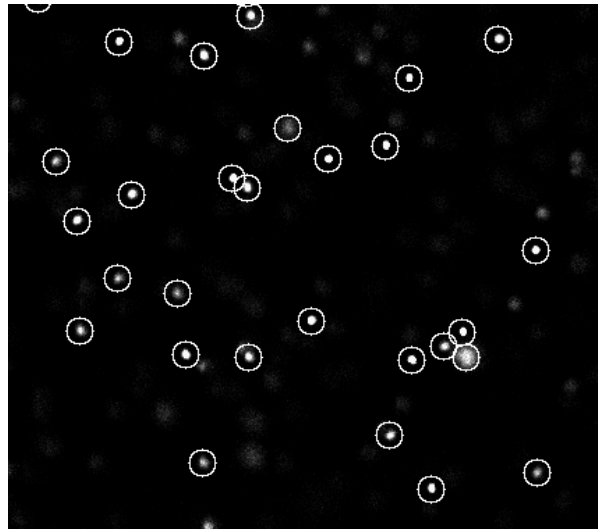


Figure.A.1.3. Shows the selected particles in the test image after treating with feature.pro.

Up to now, we have discussed the first 3 stages of the tracking algorithm and also we know various parameters to track the particles in our test image. In order to link the

locations into trajectories, we have to apply this process to all images. For convenience, the feature.pro and bpass.pro have been combined into one program, epretrack.pro, that can run on large, multiple image data sets once the correct bpass.pro and feature.pro parameters have been determined interactively on single images. The calling sequence of epretrack.pro is given below.

epretrack,'filename.tif',bpass.pro,feature.pro,/tiff,/multiepretrack.

In this case file name is “test”, so

- epretrack,'test.tif',bplo=1,bphi=6,dia=6,mass=2700,/tiff,/multi.

Where bplo and bphi correspond to lower and upper cutoff of bpass.pro, dia (which is typically same as bphi) is the diameter of the circular blob on which the centroid operation is done and mass is the third column of feature.pro which is the total brightness of the particles. Here only particles with total brightness<2700 are selected.

The epretrack.pro routine generates a file of coordinates ‘pt.test.tif’ (pt.filename.tif) for each image in the stack. The next step is to read the pt files that contain the data (x-centroid, y-centroid, total brightness, radius of gyration, eccentricity) for all selected particles in all frames.

- pt=read_gdf('pt.test.tif')

We then check for pixel biasing which gives us an opportunity to make sure that the parameters were well chosen. This is done by plotting a histogram of the fractional part of the x-positions of the particles. If there is no favored sub-pixel value the histogram of the x-position of all particle positions modulo 1 should be completely flat.

- plot_hist,pt(0,*) mod 1,binsize=0.1

On the other hand if the histogram is not flat then the parameters need to be refined until we achieve a flat histogram. Figure.A.1.4 corresponds to the histograms of pixel biasing for two different dia values: (a) d=6 and (b) d=3.

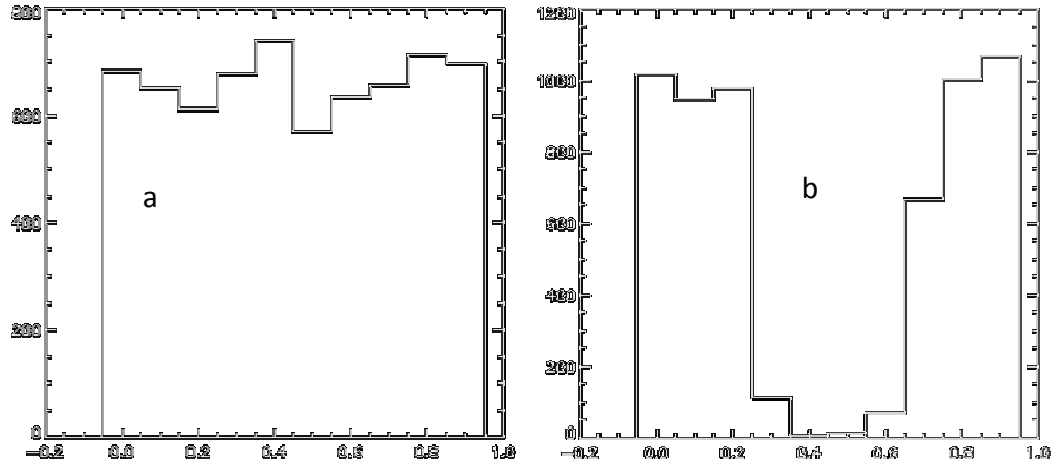


Figure.A.1.4. Corresponds to the histograms of pixel biasing for two different d values:
(a) $d=6$ and (b) $d=3$.

- `plot,ft(2,*),ft(3,*),psym=3;`

The above command shows a plot of the brightness versus the radius and allows us to verify that the correct cut-off was chosen, see figure.A.1.5.

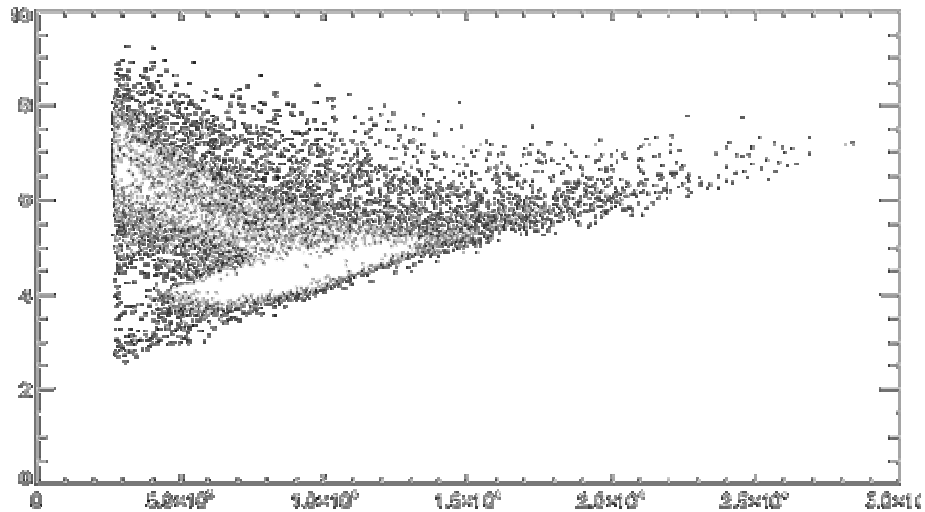


Figure.A.1.5. Corresponds to the histograms of pixel biasing for two different d values:
(a) $d=6$ and (b) $d=3$.

We can use the following commands to visualize a movie of particle displacements in all images.

- `a = readtiffstack('test.tif')`
- `fo=fover2d(a,pt,/circle,rad=10)`
- `movie,fo`

Sometimes the movie shows that there are still unwanted or false particles (eg. particle aggregates). These unwanted particles can be eliminated by choosing stricter cut-offs as explained above. Eg.:

- `ft=eclip(pt,[3,1,9])`
- `ft=eclip(pt,[2,10000,40000])`
- `ft=eclip(pt,[4,0,0.3])`

After determining the particle positions with sub-pixel accuracy, we need to connect the particle positions in different images to create the trajectories. The particle positions in the successive images can be identified only on the basis of proximity because the size and intensity of the particles are the same. The optimum identification of particle positions should minimize the total squared distance of travel (Crocker, JC and Grier DG., 1996). To make such identification computationally feasible, a maximum possible particle displacement between images must be specified. This parameter should be sufficiently large, to ensure that true displacements are not rejected and small enough so that different particles in subsequent frames are rarely considered the same displaced particle. The `track.pro` routine is used to perform this operation. For this routine the user has to set two parameters: one is the maximum possible distance that a particle is allowed to displace between two successive images and the other is the number of continuous frames in which the particles is visible. The latter provides an additional level of filtering because an artefact unlikely to occur in several consecutive frames. The calling sequence of `tracking.pro` is shown below,

- `tr = track(pt,8,goodenough=5,memory=0,dim=2)`

8 is the maximum displacement in pixels of particles between two consecutive images, `goodenough=5` means that only those particles are considered that occur at least in 5 continuous frames. "memory" allows us to track particles which temporarily

disappear -- it acts as a memory. Thus particles may be missing for a chosen number of frames in a row, but if they reappear in the same location, they are still considered the same particle. This can be useful if the particles are occasionally coming in and out of focus. `dim =2` means that the tracking is in two dimensions. It is possible to track in 3 dimensions, but only for very slow diffusion as many more images need to be taken at each time slice. `tr` consists of 7 columns: the first five are from `feature(x, y, brightness, radius and eccentricity)`; the sixth column is the time stamp from `epretrack` and the seventh column is a unique particle ID #.

- `p=mkpdf(tr,i,dim=2);`

This command returns the trajectories of the particle at a given time slice `i`. In order to verify that the displacement setting is correct, a histogram of the particle displacements between consecutive frames can be generated. The histogram should completely decay and not be truncated by the maximum displacement setting. Any of the following commands can be used to generate the histogram.

- `plot_hist,p(0,*),data,coff,center,/fit,/log`
- `plot_hist,p(0,*),data,coff,center,/fit;`
- `plot_hist,p(1,*),data,coff,center,/fit,/log`
- `plot_hist,p(1,*),data,coff,center,/fit`

The first two commands will generate a histogram of particle displacement along the x-direction; one will be in log scale and the other one in linear scale. Figure.A.1.6 obtained by plotting the histogram for two different maximum displacement settings: (a)=10 and b=(3).

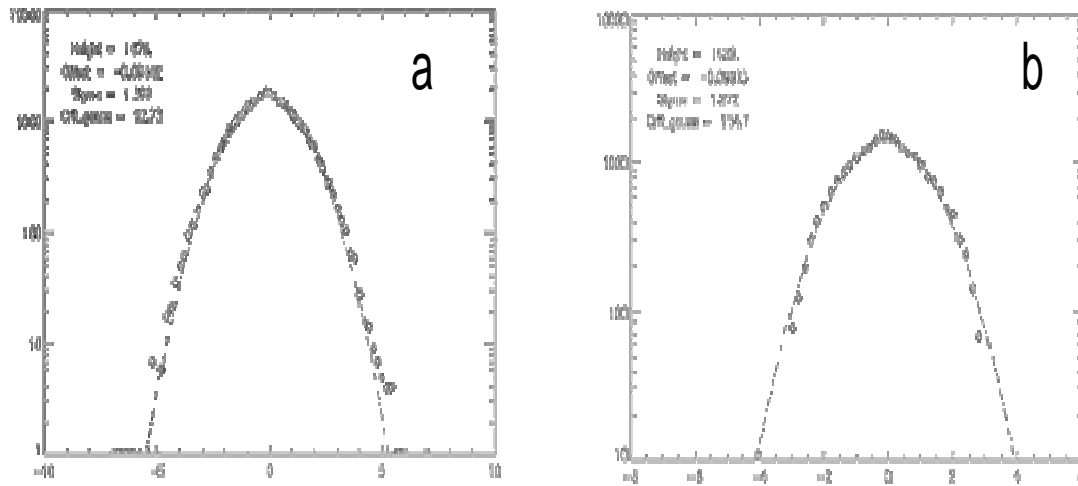


Figure.A.1.6. Obtained by plotting the histogram for two different maximum displacement setting: (a)=8 and (b)=3. The maximum displacement setting at (a) is correct since the histogram completely decays at the maximum displacement while in (b) it is truncated.

If the maximum displacement setting is fine, then we can proceed to the next step where we visualize the trajectories of a single particle. The commands for generating particle trajectories are:

- `w=where(tr(6,*) eq 1)`
- `plot,tr(0,w),tr(1,w),/isotropic,/ynozero`

This trajectory corresponds to the particle with identification number#1 (eq 1) is shown in figure.A.1.7.

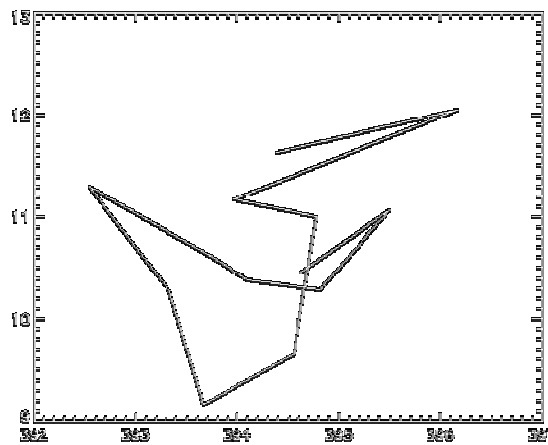


Figure.A.1.7. Trajectories of particles with $R=0.25 \mu\text{m}$ in $\beta\text{-Ig}$ solution with $C=80 \text{ g/l}$ and the time interval between the image was 0.31s .

The coordinates of all the particles are stored in tr and need to be averaged using the following command:

- `k=msdres(tr, maxtime=40)`

k consists of 15 columns:(0)the time stamp of images t (1)number of tracks (2) number of significant tracks (3) average displacement in the x direction, $\langle x \rangle$ (4)average displacement in the y direction, $\langle y \rangle$ (5) MSD in x direction, $\langle x^2 \rangle$ (6)MSD in y direction, $\langle y^2 \rangle$ (7) $\langle x^2 \rangle - \langle x \rangle^2$ (8) $\langle y^2 \rangle - \langle y \rangle^2$ (9) $\langle r^2 \rangle - \langle r \rangle^2$ (10) centerx, (11)sigx², (12) centery, (13) sigy², (14) sigr².

- `plot, k(0,*), k(5,*), psym=6`
- `oplot, k(0,*), k(9,*), psym=6`

The 0th column of k corresponds to the time scale and 5th column corresponds to average displacement in y-direction. So this command generates a graph in which the average displacement of the particles in the y direction is plotted as a function of time. On the other hand, column 9 corresponds to the average MSD of the particles in the x and y direction. So the second command will plot MSD of the particles as a function of time.

- `his=plothistsqr(tr, dimax=20, binsize=0.3, min=-1, max=3.) ;`
- `write_text, his, 'histsqr.txt'`

The above commands visualize and write in a file the distribution of MSD of particles which is Gaussian for normal diffusion and broader for anomalous diffusion. Figure.A.1.8 shows the distribution of MSD of particles with $R=0.25 \mu\text{m}$ in $\beta\text{-lg}$ solution with $C=80 \text{ g/l}$.

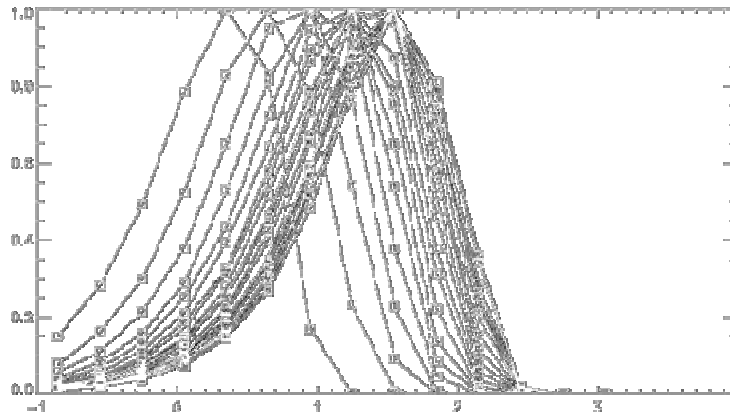


Figure.A.1.8. Distribution of MSD of particles with $R=0.25 \mu\text{m}$ in $\beta\text{-lg}$ solution with $C=80 \text{ g/l}$.

Annex-2. Most likelihood estimation method for FRAP

Frap data were analyzed with a recently developed a pixel based statistical methodology utilizing the most likelihood estimation (MLE) (Jonasson et al., 1986). The method takes in to account all the pixels including those pixels outside the bleached region. It is assumed that the noise in the image is independent between pixels and in time and is distributed with mean zero and constant variance σ^2 . The essential requirement of this method is that the intensity profile of the data must be Gaussian at all times during the recovery. Advantages of this method are that it can provide the error estimates of the parameters it calculates and also the effect of the point spread function is negligible. It maximizes the likelihood function of a series of images and estimates the diffusion coefficient of the fluorescent tracers with an error bar.

For a Gaussian concentration profile, the initial tracer concentration after bleaching can be written in the form:

$$C_0(r) = a_0 - \frac{a_1}{r^2} \exp\left(-\frac{r^2}{r_0^2}\right) \quad \text{A2.1}$$

If the recovery is caused by Brownian diffusion of the tracers, then the concentration at a distance r from the center of the bleached region at time t is given by:

$$C(r, t) = a_0 - \frac{a_1}{4Dt + r_0^2} \exp\left(-\frac{r^2}{4Dt + r_0^2}\right) \quad \text{A2.2}$$

If the concentration of fluorochrome is low enough then the pixel intensity $p(i, t)$ at pixel i at a distance r_i from the center of the bleached region at time t is proportional to the unbleached tracer concentration $C(r, t)$.

Annex-2.1. Input setting for FRAP data analysis

The data analysis was carried out in Mat-lab. First we have to open the “mainalltimes_datasave.m” which is the programme file needed to analyze the images. As in the case of the particle tracking algorithm, here also we have to insert some input parameters. There are two sets of input parameters: the first set of parameters are correct or only approximate while the second set of parameters specify folders and file names. All these parameters will be explained with the help of an example. For illustration, here we consider the FRPA data analysis of d500k in water and the file name is “test_data”.

The first input parameter is the number of postbleach images that are used for the analysis. In all the cases we have used 30 images and the command is given below,

- `no_images = 30;`

Next we have to insert the pixel size in meters, which is denoted as `side` in the programme. We used a 20×water immersion objective with a zoom factor of 8, which gives a pixel size of 122 nm.

- `side = 0.122070e-6;`

The time interval between the images, which is denoted as `delta_t`, is also required.

- `delta_t = 0.5;`

Next we have to specify the type of the image. If the images are 12 bit then we set `twelve=1` otherwise `twelve=0`. Here the images are saved as 8 bit-tif format. Hence we set `twelve` as zero.

- `twelve=0;`

Another input parameter is the size of the ROI or the diameter of the bleached region which is here 30 μm .

- `ROI=30e-6;`

As mentioned in section 2.2.13.2, the programme determines the intensity of the unbleached fluorescein molecules as a function of distance from the center of the bleached region. Hence we have to set the central pixel of the bleached region. In the programme `centx` and `centy` correspond to the x coordinate and y coordinate of the central pixel, respectively. The image format is 512×512 and hence `centx` and `centy` are about 256.

- `centx=256;`
- `centy=256;`

If the center coordinates are exactly known then we set `known_cent=1` and we set `known_cent=0` if the coordinates are only approximations. We have always set,

- `known_cent=0;`

As mentioned above, the programme maximizes the likelihood functions of a series of images to calculate the parameters of diffusion. So the next step is to find out the likelihood functions of each image. In order to calculate the likelihood function an initial guess is needed which is given by,

- $\text{guess}=(2*\text{side}/\text{ROI})^2;$

Here the programme calculates the guess from the side (the pixel size in meters) and ROI (the diameter of the bleached region). Unfortunately, the ROI (here it 30 μm) also depends on the point spread function of the laser and hence the exact measurement of ROI is difficult. Hence the programme allows one to set guess manually and it is done by setting guessp equal 0 or 1.

- $\text{guessp}=0$ or 1;

If we set $\text{guessp}=1$, then the programme will generate a graph where guess should be given as the approximate value where the curve cuts the x-axis, see figure.A.2.1,

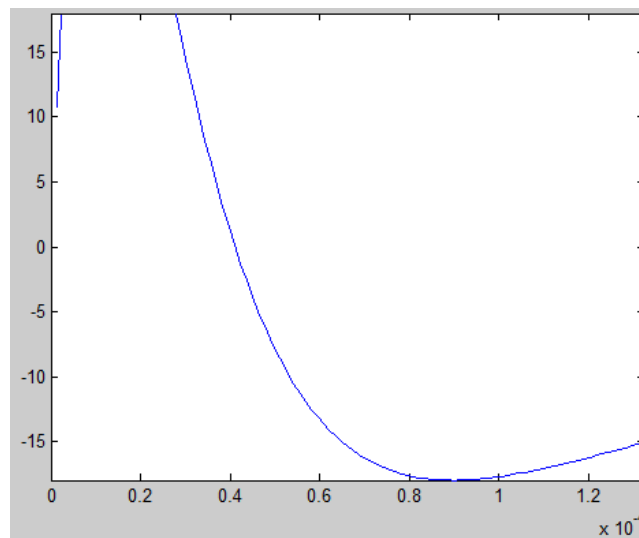


Figure.A.2.1.Shows the guess value and is the point where the curve cut x-axis which is approximately 0.8×10^{-4} .

However we found that the manually obtained guess and the one obtained from the equation are almost the same and hence we set $\text{guessp}=0$.

The next groups of input parameters specify folders and file names. The filenames of the images have the following structure,

- `folder\namerepnr_tjjj_endname`

where repnr is a vector of replicate numbers for the files with the same file name and it can be between 00 and 99.The file with name "test_data" consists of different FRAP measurements and each one has different repnr. This number is generated by the confocal software and for example repnr 06 has the following sequences of images:

- test_data_FRAP Pre Series06 (10 images with different time stamps)
- test_data_FRAP Bleach Series06 (10 images with different time stamps)
- test_data_FRAP Pb1 Series06 (100 images with different time stamps)

tjjj corresponds to the different time stamps of the images and it can be between 000 and 999.

Thus for the first post-bleach image with repnr 06 has the following structure of the file name:

- C:\FRAP\test_data\test_data_FRAP Pb1 Series06_t000_ch00.tif

If we consider above image as an example, then the folder is given by,

- folder='C:\FRAP\test_data\';(on a windows system)

Next we have to set the folder where the results are saved.

- savefolder='C:\FRAP\test_data\';
- starttime=0;

If the image sequences start from t000 and starttime=1 if the image sequences start from t001 and so on. In some cases the intensity profile of the first post-bleach images are not Gaussian for high molecular weight probes and in this situation we can set starttime=1 or 2 so that the first post-bleach images are not considered for the analysis.

Enter the name of the post-bleach images,

- name=strcat('test_data_FRAP Pb1 Series');
- repnr=[06];
- endname='_ch00.tif';

Thus the post bleach images test_data_FRAP Pb1 Series06_t000 to t029_ch00.tif (since the total number of images was set as 30) will be analyzed to measure the parameters of diffusion.

Next we have to enter the detail of the pre-bleach images. It is not necessary to use pre-bleach images since the average intensity outside the bleached region can be considered as the initial intensity or the intensity of the pre-bleach images.

- preim=1;

Pre-bleach images should be used otherwise preim=0.

- prename=strcat('L 0s048cd2000k0c_FRAP Pre Series');

Name of the prebleach images.

- prenr=00;
- prenr1=09;

The first and last number of pre-bleach images.

The mat-lab programme generates two text files in which the results are stored and these files are stored as savename and savename2, see below:

- `savename=strcat(savefolder,'resparnormalmodel.txt');`
- `savename2=strcat(savefolder,'resparnormalmodel.txt');`

The results saved in “savename” are 1) a 0-1 variable indicating if the background procedure was used (1) or not (0), 2) a 0-1 variable indicating if the pre-bleach images were used (1) or not (0), 3) the replicate number, 4) the number of images used in the estimation, 5) the estimated diffusion coefficient in unit of $\mu m^2/s$, 6) a lower bound of a 95% confidence interval for the diffusion coefficient in units of $\mu m^2/s$, 7) an upper bound of a 95% confidence interval for the diffusion coefficient in unit $\mu m^2/s$, 8) the standard deviation for the diffusion coefficient in units of $(\mu m)^2/s$ and 9) the value of the likelihood function at the optimal value of the parameters.

savename2, the filename for saving more results namely the parameters of Eq. A2.1 and A2.2 with standard deviations. That is 1) a_0 , 2) a_1 unit pix^2 , 3) D unit pix^2/s , 4) r_0 unit pix^2 , 5) σ^2 , 6) standard deviation of a_0 , 7) standard deviation of a_1 , 8) standard deviation of D , 9) standard deviation of r_0 , 10) standard deviation of σ^2 .

The programme allows one to visualize the plot of the intensity of the CLSM images as a function of distance from the center of the bleached region and the fit obtained from the MLE method. These plots are called diagnostic plots and the interval (dstep) between the diagnostic plots can be adjusted.

- `dstep=1;`

The above command generates diagnostic plots for every image in a sequence

- `saveplots=1;`

If the diagnostic plots should be saved otherwise 0.

- `imform='jpg';`

Diagnostic plot could be saved in jpeg format. It is also possible to save images as other format like eps.

Image preprocessing like background adjustments and crop is also possible. However, we used images without any preprocessing and hence we set:

- `back=0;`

- crop=0;

Annex-3. Input setting for the pair correlation analysis

In the case of β -lg gels, we found that combining two zoom factors 1 and 4 with a 63 \times water immersion objective was sufficient to cover the whole range of r . For the pair correlation analysis, six images were taken for each zoom. These images are combined together to make a stack of images and then saved as raw format.

The pair correlation analysis of the CLSM images was carried out with the help of a home build programme. The input parameters that are required for this programme are: number pixels of in the images, total number of images in the stack , the maximum distance that has to be correlated with a reference pixel, total number of pixels that are should for the analysis, the probability of choosing a pixel as the reference image.

The general format of the input setting in our programme is given by:

- correl_confocal01 name of the stack 512 512 6 100 100 0 -1

First two columns after the name of the stack correspond to the total number of pixels of the CLSM images along the X and Y direction. Number 6 is the total number of images in the stack. The next two columns correspond to the whole range of r from the reference pixel along the x and y direction. 0 indicates that the programme chooses all the pixels in the image for analysis at a distance which is larger than the maximum value of r from the edge of the image. -1 in the last column shows that there is no preferred probability of choosing a reference pixel in the image or the selection of the reference pixel is purely random.

References

- Ako, K. (2010). Etude de la structure des gels protéiques par Microscopie confocale. Polymères, Colloïdes, Interfaces, vol. Ph.D. Le Mans: Univ. du Maine.
- Ako, K., Durand, D., Nicolai, T., & Becu, L. (2009). Quantitative analysis of confocal laser scanning microscopy images of heat-set globular protein gels. *Food Hydrocolloids*, 23, 1111-1119.
- Ako, K., Nicolai, T., Durand, D., & Brottons, G. (2009). Micro-phase separation explains the abrupt structural change of denatured globular protein gels on varying the ionic strength or the pH. *Soft Matter*, 5, 4033-4041.
- Atkins, P. (Ed.). (1994). *Spectroscopy 2: Electronic Transmissions in Physical Chemistry* (5 ed.). New York: W. H. Freeman & Company.
- Aveyard, R., Binks, B. P., & Clint, J. H. (2003). Emulsions stabilised solely by colloidal particles. *Advances in Colloid and Interface Science*, 100, 503-546.
- Axelrod, D., Koppel, D. E., Schlessinger, J., Elson, E., & Webb, W. W. (1976). Mobility measurement by analysis of fluorescence photobleaching recovery kinetics. *Biophysical Journal*, 16(9), 1055-1069.
- Babu, S., Gimel, J. C., & Nicolai, T. (2008). Tracer Diffusion in Colloidal Gels. *J. Phys. Chem. B*, 112, 743-748.
- Bamberger, S., Seaman, G. V. F., Sharp, K. A., & Brooks, D. E. (1984). The effects of salts on the interfacial tension of aqueous dextran poly(ethylene glycol) phase systems. *Journal of Colloid and Interface Science*, 99(1), 194-200.
- Bauer, R., Hansen, S., & ogendal, L. (1998). Detection of Intermediate Oligomers, Important for the Formation of Heat Aggregates of beta-lactoglobulin. *International Dairy Journal*, 8(2), 105-112.
- Baussay, K., Bon, C. L., Nicolai, T., Durand, D., & Busnel, J. P. (2004). Influence of the ionic strength on the heat-induced aggregation of the globular protein beta-lactoglobulin at pH 7. *Int J Biol Macromol*, 34(1-2), 21-28.
- Berne, B., & Pecora, R. (1976). *Dynamic light scattering*. New York: Wiley;.
- Binks, B. P., & Horozov, T. S. (2006). *Colloidal particles at liquid interfaces*. Cambridge University Press.
- Brownlow, S., Morais Cabral, J. H., Cooper, R., Flower, D. R., Yewdall, S. J., Polikarpov, I., et al. (1997). Bovine beta-lactoglobulin at 1.8 Å resolution--still an enigmatic lipocalin. *Structure*, 5(4), 481-495.
- Colsenet, R., Soderman, O., & Mariette, F. (2006a). Effects of Ionic Strength and Denaturation Time on Polyethyleneglycol Self-Diffusion in Whey Protein Solutions and Gels Visualized by Nuclear Magnetic Resonance. *J. Agric. Food Chem.*, 54, 5105-5112.
- Colsenet, R., Soderman, O., & Mariette, F. (2006b). Pulsed Field Gradient NMR Study of Poly(ethylene glycol) Diffusion in Whey Protein Solutions and Gels. *Macromolecules*, 39, 1053-1059.
- Crocker, J. C., & Grier, D. G. (1996). Methods of Digital Video Microscopy for Colloidal Studies. *Journal of Colloid and Interface Science*, 179(1), 298-310.
- Croguennoc, P., Nicolai, T., Kuil, M. E., & Hollander, J. G. (2001). Self-diffusion of Native Proteins and Dextran in Heat-set Globular Protein Gels. *J. Phys. Chem. B*, 105, 5782-5788.
- Cucheval, A. S. B., Vincent, R. R., Hemar, Y., Otter, D., & Williams, M. A. K. (2009). Multiple Particle Tracking Investigations of Acid Milk Gels Using Tracer Particles with Designed Surface Chemistries and Comparison with Diffusing Wave Spectroscopy Studies. *Langmuir*, 25, 11827-11834.
- Cussler, E. L. (2000). *Diffusion mass transfer in fluid systems*. 2nd edition. Cambridge University Press.

- Ding, P., Wolf, B., Frith, W. J., Clark, A. H., Norton, I. T., & Pacek, A. W. (2002). Interfacial tension in phase-separated gelatin/dextran aqueous mixtures. *Journal of Colloid and Interface Science*, 253(2), 367-376.
- Durand, D., Gimel, J. C., & Nicolai, T. (2002). Aggregation, gelation and phase separation of heat denatured globular proteins. *Phys. A*, 304, 253-265.
- Fick, A. (1855). Concerns diffusion and concentration gradient. *Ann Phys*, 170, 59.
- Firoozmand, H., Murray, B. S., & Dickinson, E. (2009). Interfacial Structuring in a Phase-Separating Mixed Biopolymer Solution Containing Colloidal Particles. *Langmuir*, 25(3), 1300-1305.
- Forciniti, D., Hall, C. K., & Kula, M. R. (1990). Interfacial-tension of polyethyleneglycol-dextran-water systems - Influence of temperature and polymer molecular-weight *Journal of Biotechnology*, 16(3-4), 279-296.
- Forciniti, D., Hall, C. K., & Kula, M. R. (1991). Influence of polymer molecular weight and temperature on phase composition in aqueous two-phase systems. *Fluid Phase Equilibria*, 61(3), 243-262.
- Fredrick, E., Walstra, P., & Dewettinck, K. (2010). Factors governing partial coalescence in oil-in-water emulsions. *Advances in Colloid and Interface Science*, 153(1-2), 30-42.
- Fricke, H. (1924). A Mathematical Treatment of the Electric Conductivity and Capacity of Disperse Systems I. The Electric Conductivity of a Suspension of Homogeneous Spheroids. *Physical Review*, 24(5), 575-587.
- Frith, W. J. (2010). Mixed biopolymer aqueous solutions - phase behaviour and rheology. *Advances in Colloid and Interface Science*, 161(1-2), 48-60.
- Guido, S., Simeone, M., & Alfani, A. (2002). Interfacial tension of aqueous mixtures of Na-caseinate and Na-alginate by drop deformation in shear flow. *Carbohydrate Polymers*, 48(2), 143-152.
- Hagman, J., Lorén, N., & Hermansson, A.-M. (2010). Effect of Gelatin Gelation Kinetics on Probe Diffusion Determined by FRAP and Rheology. *Biomacromolecules*, 11(12), 3359-3366.
- Hambling, S. G., McAlpine, A. S., & Sawyer, L. (1992). Beta-lactoglobulin. In: Fox PF, ed. *Advanced dairy chemistry*. Amsterdam: Elsevier. pp 141-190.
- Jonasson, J., Lorén, N., Olofsson, P., Nydén, M., & Rudemo, M. (2008). A pixel-based likelihood framework for analysis of fluorescence recovery after photobleaching data. *J. Microsc.*, 232, 260-269.
- Jung, J.-M., Savin, G., Pouzot, M., Schmitt, C., & Mezzenga, R. (2008). Structure of Heat-Induced beta-Lactoglobulin Aggregates and their Complexes with Sodium-Dodecyl Sulfate. *Biomacromolecules*, 9(9), 2477-2486.
- Kabalnov, A. (1998). Thermodynamic and theoretical aspects of emulsions and their stability. *Current Opinion in Colloid & Interface Science*, 3(3), 270-275.
- Le Bon, C., Nicolai, T., & Durand, D. (1999). Kinetics of Aggregation and Gelation of Globular Proteins after Heat-Induced Denaturation. *Macromolecules*, 32, 6120-6127.
- Levine, S., & Sanford, E. (1985). Stabilization of emulsion droplets by fine powders. *Canadian Journal of Chemical Engineering*, 63(2), 258-268.
- Lorén, N., Nydén, M., & Hermansson, A.-M. (2009). Determination of local diffusion properties in heterogeneous biomaterials. *Advances in Colloid and Interface Science*, 150(1), 5-15.
- Mackie, J. S., & Meares, P. (1955). The Sorption of Electrolytes by a Cation-Exchange Resin Membrane. *Proc R Soc London A*, 232, 485-498.

- Masaro, L., & Zhu, X. X. (1999). Physical models of diffusion for polymer solutions, gels and solids. *Progress in Polymer Science*, 24(5), 731-775.
- McClements, D. J. (2005). *Food Emulsions: Principles, Practice and Techniques*, 2nd Edition. CRC Press. Boca Raton, Florida.
- Mehalebi, S., Nicolai, T., & Durand, D. (2008). The influence of electrostatic interaction on the structure and the shear modulus of heat-set globular protein gels. *Soft Matter*, 4, 893-900.
- Moschakis, T., Murray, B. S., & Dickinson, E. (2006). Particle Tracking Using Confocal Microscopy to Probe the Microrheology in a Phase-Separating Emulsion Containing Nonadsorbing Polysaccharide. *Langmuir*, 22(10), 4710-4719.
- Nicolai, T., Britten, M., & Schmitt, C. (2011). Beta-Lactoglobulin and WPI aggregates: Formation, structure and applications. *Food Hydrocolloids*, 25(8), 1945-1962.
- Nicolai, T., Pouzot, M., Durand, D., Weijers, M., & Visschers, R. W. (2006). Iso-scattering points during heat-induced aggregation and gelation of globular proteins indicating micro-phase separation. *EPL (Europhysics Letters)*, 73(2), 299-305.
- Norton, I. T., & Frith, W. J. (2001). Microstructure design in mixed biopolymer composites. *Food Hydrocolloids*, 15(4-6), 543-553.
- Ogston, A. G., Preston, B. N., & Wells, J. D. (1973). On the Transport of Compact Particles Through Solutions of Chain-Polymers. *Proceedings of the Royal Society of London. A. Mathematical and Physical Sciences*, 333(1594), 297-316.
- Oliveira, K. M., Valente-Mesquita, V. L., Botelho, M. M., Sawyer, L., Ferreira, S. T., & Polikarpov, I. (2001). Crystal structures of bovine beta-lactoglobulin in the orthorhombic space group C222(1). Structural differences between genetic variants A and B and features of the Tanford transition. *Eur J Biochem*, 268(2), 477-483.
- Peters, R., Peters, J., Tews, K. H., & Bahr, W. (1974). Microfluorimetric study of translational diffusion in erythrocyte-membranes. *Biochimica Et Biophysica Acta*, 367(3), 282-294.
- Phillies, G. D. J. (1986). Universal scaling equation for self-diffusion by macromolecules in solution. *Macromolecules*, 19(9), 2367-2376.
- Phillies, G. D. J. (1987). Dynamics of polymers in concentrated-solutions - the universal scaling equation derived. *Macromolecules*, 20(3), 558-564.
- Phillies, G. D. J. (1989). The hydrodynamic scaling model for polymer self-diffusion. *Journal of Physical Chemistry*, 93(13), 5029-5039.
- Phillies, G. D. J. (1992). Range of validity of the hydrodynamic scaling model. *Journal of Physical Chemistry*, 96(24), 10061-10066.
- Pickering, S. U. (1907). *Emulsions*. *Journal of the Chemical Society*, 91, 2001-2021.
- Picullell, L., & Lindman, B. (1992). Association and segregation in aqueous polymer/polymer, polymer surfactant, and surfactant surfactant mixtures - similarities and differences. *Advances in Colloid and Interface Science*, 41, 149-178.
- Pouzot, M., Durand, D., & Nicolai, T. (2004). Influence of the Ionic Strength on the Structure of Heat-Set Globular Protein Gels at pH 7. Beta-lactoglobulin. *Macromolecules*, 37(23), 8703-8708.
- Stepanek, P. (1993). In: Brown W, editor. *Dynamic light scattering*. Oxford: Oxford University Press.
- Tarimala, S., Ranabothu, S. R., Verneti, J. P., & Dai, L. L. (2004). Mobility and In Situ Aggregation of Charged Microparticles at Oil-Water Interfaces. *Langmuir*, 20(13), 5171-5173.

- Townend, R., Winterbottom, R. J., & Timasheff, S. N. (1960). Molecular Interactions in beta-Lactoglobulin. II. Ultracentrifugal and Electrophoretic Studies of the Association of beta-Lactoglobulin below its Isoelectric Point². *Journal of the American Chemical Society*, 82(12), 3161-3168.
- Tsien, R. Y., & Waggoner, A. (1995). Fluorophores for confocal microscopy. In *Handbook of Biological Confocal Microscopy*, 2nd Ed.; Pawley, J.B., Ed.; Plenum Press: New York, 267-280.
- Wu, Y.-T., Zhu, Z.-Q., Lin, D.-Q., & Li, M. (1999). Modeling of liquid-liquid equilibrium of polyethylene glycol-salt aqueous two-phase systems—the effect of partial dissociation of the salt. *Fluid Phase Equilibria*, 154(1), 109-122.